8-14-2015

# A Study of Adobe Wall Moisture Profiles and the Resulting Effects on Matched Illumination Waveforms in Through-The-Wall Radar Applications

Steven Ryan Price

# A study of adobe wall moisture profiles and the resulting effects on matched illumination waveforms in through-the-wall radar applications

By

Steven Ryan Price

A Dissertation
Submitted to the Faculty of
Mississippi State University
in Partial Fulfillment of the Requirements
for the Degree of Doctor of Philosophy
in Electrical and Computer Engineering
in the Department of Electrical and Computer Engineering

Mississippi State, Mississippi

August 2015

A study of adobe wall moisture profiles and the resulting effects on matched illumination waveforms in through-the-wall radar applications

By

Steven Ryan Price

Approved:

_____

J. Patrick Donohoe
(Major Professor)

_____

Derek T. Anderson
(Committee Member)

_____

Erdem Topsakal
(Committee Member)

_____

Nicolas H. Younan
(Committee Member)

_____

James E. Fowler
(Graduate Coordinator)

_____

Jason M. Keith
Dean
Bagley College of Engineering

Name: Steven Ryan Price

Date of Degree: August 14, 2015

Institution: Mississippi State University

Major Field: Electrical and Computer Engineering

Major Professor: J. Patrick Donohoe

Title of Study: A study of adobe wall moisture profiles and the resulting effects on matched illumination waveforms in through-the-wall radar applications

Pages in Study: 138

Candidate for Degree of Doctor of Philosophy

In this dissertation, methods utilizing matched illumination theory to optimally design waveforms for enhanced target detection and identification in the context of through-the-wall radar (TWR) are explored. The accuracy of assumptions made in the waveform design process is evaluated through simulation. Additionally, the moisture profile of an adobe wall is investigated, and it is shown that the moisture profile of the wall will introduce significant variations in the matched illumination waveforms and subsequently, affect the resulting ability of the radar system to correctly identify and detect a target behind the wall. Experimental measurements of adobe wall moisture and corresponding dielectric properties confirms the need for accurate moisture profile information when designing radar waveforms which enhance signal-to-interference-plus-noise ratio (SINR) through use of matched illumination waveforms on the wall/target scenario. Furthermore, an evaluation of the ability to produce an optimal, matched illumination waveform for transmission using simple, common radar systems is undertaken and radar performance is evaluated.

DEDICATION

*To my wife Rachel, and to my family Shelby, Stephanie, Shannon, and Stanton along with Tony and Bettye Jenkins for their enduring support and inspiration.*

ACKNOWLEDGEMENTS

This work is a reflection of the time and effort afforded me by my parents and all of the teachers and professors that I have had the benefit of learning from throughout my life. The expression often credited to Isaac Newton, "If I have seen further, it is by standing upon the shoulder of giants," fits well to my circumstance.

I am especially grateful to my advisor, Dr. J. Patrick Donohoe, for guiding me patiently through this trek. Additionally, I would like to express my gratitude to Dr. Derek Anderson for our many fruitful discussions, as well as the valuable assistance from my dissertation committee members, Dr. Erdem Topsakal and Dr. Nicolas Younan. Furthermore, I would like to thank Dr. John Ball for participating in my dissertation defense. I have received much support from many friends and colleagues, and I wish to thank them as well.

Finally, I would like to thank the U.S. Army Corps. Of Engineers, Engineer Research and Development Center of Vicksburg, MS for all the support I have received and allowing me the ability to conduct such challenging, interesting, and worthwhile work.

TABLE OF CONTENTS

LIST OF TABLES

LIST OF FIGURES

# CHAPTER I

# INTRODUCTION

The ability to sense information in an enclosed structure is of great importance to numerous police, emergency, and military applications. Through-the-wall radar (TWR) is a particularly emerging area of remote sensing research related to sensing information within an enclosed structure. TWR aims to develop technologies that provide high quality imaging or identification and detection of objects within a building structure (and thus are located behind a wall). Examples of TWR applications include the determination of building layouts, the possibility of occupants and their locations, and the identification and classification of objects or materials within the building [1-3]. For example, with accurate sensing and imaging of a TWR scenario, police can better handle a hostage situation by obtaining knowledge of the building layout, the likelihood of hazardous materials being present, and the probable locations of hostages and captors. Thus, the ultimate goal of TWR is having the capability to provide information (vision) into areas that are otherwise unobservable through standard means.

The development of remote sensing techniques and algorithms depend entirely on the physical propagation characteristics of materials present in the considered environment as well as sensor capabilities. Typically, all remote sensing applications begin with physics-based wave equations that process the information returned to sensors. Data collected at different sensor positions and times are accumulated and

processed to form an image of the target space using the appropriate wave equations. Because the wave equations describe the nature of interactions between the wave (e.g. radio, light, sound) and media present in the remote environment, the sensor provided complex returns form an image through comparison of the measured complex returns and the returns predicted by free space assumptions of the wave equations. However, when considering more complex problems such as transmission through scattering media, free-space propagation assumptions are no longer valid and cannot be applied. For these applications, the signal no longer simply propagates through free-space but may be reflected, refracted and or diffracted. Examples of non-free-space applications include geophysical sensing (GPR), medical imaging, and through-the-wall sensing. Furthermore, each example contains its own respective set of challenges and techniques. For instance, in geophysical and medical applications, the considered sensing medium composes the entire volume but is discontinuous. Similarly, TWR encounters many air-medium interfaces that significantly change the propagating wavefront. For geophysical and medical applications, sensors are typically placed near or in direct contact with the medium to better propagate through the medium. Conversely, sensors for TWR are often located away from the building structure so that the attenuation is a result of the wall/target rather than the large volumes of air that compose the building structure [4-9].

Research in TWR developed from its close relation to ground-penetrating radar and is predominantly guided by the specific through-wall application desired. Two main areas of recent research emphasis include whether the application seeks information on movement within the building structure, or whether the application desires imaging the interior layout of the structure and/or detecting its contents. To this end, it is noted that

the work in this document concerns itself with a static environment and imaging or identifying and detecting contents situated behind a structure.

Propagation effects degrade imaging and detection results and must be accounted for in order to have proper TWR operation. Because propagating waveforms in through-wall radar may experience numerous air-wall interfaces, propagation effects such as attenuation, dispersion, diffraction, reflections/refractions, and multipath may be encountered multiple times and can significantly affect the radar signal. Without properly accounting for these effects, the ability to image and detect contents within enclosed structures will be severely degraded. Typical techniques used to combat some of these effects include image-focusing algorithms that attempt to perform wavefront corrections and tomographic algorithms that improve shadowing and attenuation by adjusting for projection through material volumes but these algorithms usually do not account for multipath and Bragg scattering [25-27]. Hence, utilizing techniques such as clutter rejection, multipath identification, image formation, image sharpening, array processing techniques, and synthetic aperture radar (SAR) coherently is the topic of much current research in TWR concerning imaging contents within buildings [10-24].

Relying solely on the projection information will not be sufficient to overcome the effects of multipath, dispersion, and reflection. Understanding and properly accounting for the wave interaction and propagation between the physical components of the enclosed structure being examined is vital to overcoming these ill effects. A common occurrence that hinders the performance of TWR may include incorrect localization derived when an object outside of the building interacts with the reflection of the initial front wall reflection which results in an ambiguous image inside the structure.

Furthermore, the strong front wall reflection may cause weak targets near the wall to go undetected. Another occurrence derives from multipath propagation that introduces ghosts or false targets in the image. Moreover, offsets and blurring of targets can result from uncompensated refraction through walls. Bragg scattering resulting from structural elements within a wall such as rebar can also cause ambiguous images and subsequent waveform modulation [28-30]. TWR is a challenging problem due to the numerous propagation effects as previously described, but recent research utilizing model-based reasoning presents a prospective way that propagation effects can be accounted for while also overcoming the limitations of using only projection information in TWR applications.

The model-based reasoning approach can encompass all aspects of TWR. Whether it be a distinct, direct approach of target identification and detection using typical radar signal processing techniques and pattern recognition based on *a priori* information or a general, highly complex system which iteratively forms 3-D images of a building's structure as described by Baranoski [2]. Structural details of a building can be formed by constructing each component layer of the building using inference made from differences between the predicted model and the sensed information. However, this is intuitively challenging with regards to a noisy and cluttered environment and is severely impacted when improper assumptions and estimations occur caused by wall ambiguities and inaccurate training data; thus, libraries of accurate wall structure elements is an essential part of TWR model based reasoning.

The more direct model-based approach is formed for a particular target situated in a given environment. From the *a priori* information of the desired target and wall, an

effective radar system can then be used to detect, identify, locate, and monitor a target, rather than the building's structure. Both approaches are extremely beneficial independently, but a radar system that encompasses both structural imaging and fine discrimination of internal objects (targets) has not yet been accomplished. The key challenges lie primarily in developing processing techniques and algorithms that allow suitable wavelength resolution while avoiding unacceptable ambiguities such as the previously mentioned effects over extended spatial areas.

Fundamental to TWR applications are the propagation characteristics of electromagnetic radiation through walls and at the boundaries between the air and wall, and how these characteristics depend on waveform selection which can be determined directly by the electrical properties of the wall. The choice of operating frequency is vitally important as it must consider balancing the attenuation through the wall (favoring lower frequencies) and the resolution of the imaging (favoring higher frequencies). According to Farwell of the US Army CERDEC, frequency selection of TWR is the most important design consideration as the tradeoffs are especially noticed for very dense wall materials such as adobe and concrete [1]. Furthermore, for target recognition applications, the potential target's frequency response is of substantial importance. Because a target's unique signature is frequency dependent, model-based reasoning can be utilized to incorporate both the frequency information of both the wall and target in the radar design.

The parameters used in modeling materials and wave propagation inside materials are defined by the materials' dielectric properties. The material properties of the wall, defined by permittivity, which can be expressed as $\varepsilon = \varepsilon' + j\varepsilon'' = \varepsilon_r\varepsilon_0 + j\frac{\sigma}{\omega\varepsilon_0}$, is of

great importance to TWR because it describes the effects experienced by an electromagnetic wave when interacting with or through another material such as the wall. The relative permittivity $\varepsilon_r$ and the electric conductivity $\sigma$ are the two main components that dictate wave propagation through a material and are of great importance to TWR that utilizes model-based reasoning. The angular frequency $\omega$ is adjusted according to the frequencies of interest and $\varepsilon_0$ is the vacuum permittivity; thus, material permittivity is defined by its relative permittivity $\varepsilon_r$ and conductivity $\sigma$.

Recently, matched illumination theory has been used to enhance TWR by optimally designing the transmission waveform of the radar system [31-34]. Matched illumination theory as used in TWR is a model-based reasoning technique that takes advantage of *a priori* knowledge to design optimal transmission waveforms which improve the SINR of a matched filter transmitter-receiver pair. Spurred particularly by advances in adaptive, pulse-shaping radar transmitters, a revival of research involving waveform design and diversity has been occurring with specific problem solutions [31-46]. The designed optimum waveform seeks to improve the information of the target response while also suppressing noise and clutter.

Typically, research utilizing matched illumination theory for TWR has focused on homogeneous wall structures [31-34]. The electrical properties of the wall structure are a significant TWR design consideration as the target return signature is highly dependent on the physical composition of the wall structure. The moisture level within a solid wall is of significant interest because it can change quickly due to precipitation and other environmental conditions. The typically used homogeneous wall model is insufficient to

accurately design optimal waveforms for a solid wall with non-uniform moisture profiles. A heterogeneous wall model is required.

Electromagnetic wave propagation through various wall materials has been the topic of many publications over the past couple of decades [1, 47-58]. However, with regards to moisture content and profile of a wall, the amount of openly published literature is limited [59-62, 75-82]. Perhaps, the primary reason why this type of research is limited is that methods used to measure the moisture profile of a wall is a very challenging and time consuming problem in itself and is for the most part, structurally destructive and very problem specific. Meanwhile, a method of accurate moisture profile measurement and knowledge of existing wall moisture profiles is extremely beneficial to TWR because as illustrated below in Figure 1.1, attenuation differences of more than 50 dB for two-way through-wall wave propagation are not unlikely. Thus, having more realistic wall models will lead to more accurate model-based reasoning as well as enhanced radar performance when utilizing waveform design [1, 2].

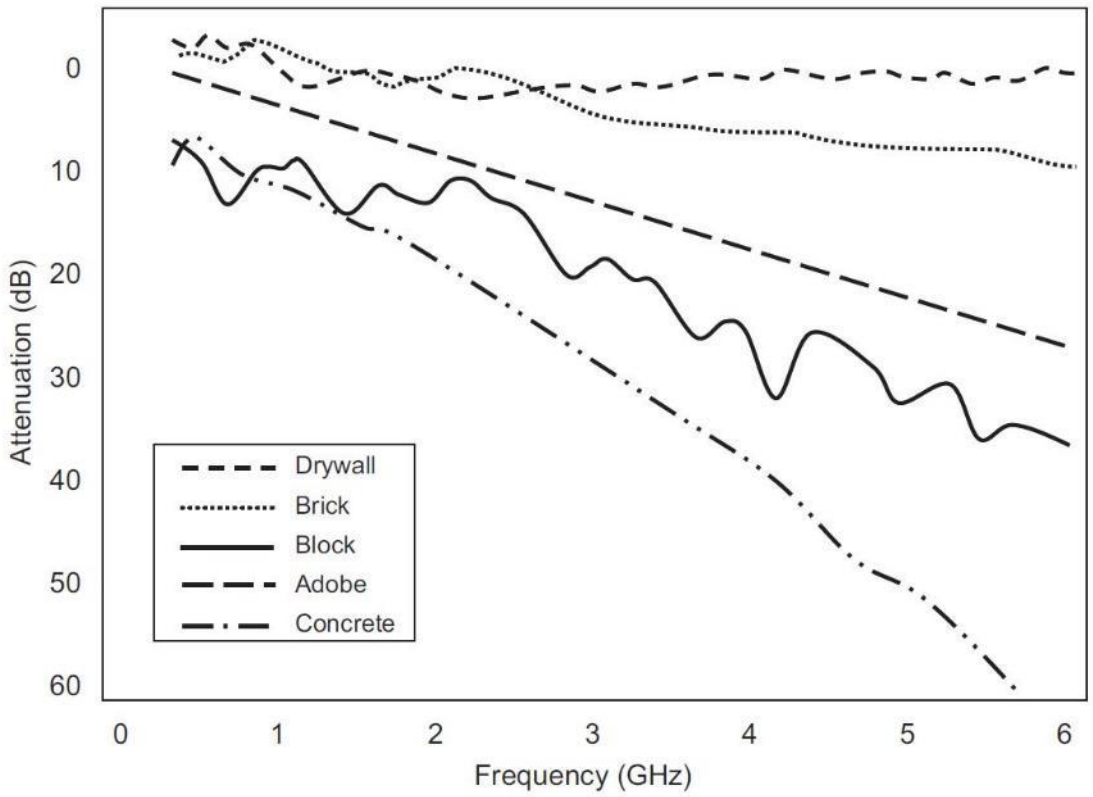


Figure 1.1 Measurements via Akela, Inc. of wall attenuation vs. frequency [1]

To combat the severe attenuation caused by the wall material, properly accounting for the wall's interaction must be accomplished for acceptable radar performance. Design of transmission waveforms is fundamental to radar system performance and influences the amount of information obtained from a target. From its inception around the 1950's, waveform design and diversity is an area of radar research that focuses on novel transmission strategies as a way to improve radar performance in a variety of civil and military applications. At the core of waveform design is the principle that any and all knowledge of the radar problem should be exploited in the design and operation of the radar system. This naturally lends itself to model-based reasoning approaches as well as

adaptive systems that can respond to dynamic conditions and resultantly increase robustness of the radar system. Waveforms such as wideband chirps, pulse trains, and phase codes are commonly designed for Doppler resolution, range resolution, and ambiguity considerations [63]. However, with a more focused design approach on transmitter-centric systems with model-based reasoning, the knowledge learned, estimated, or assumed from the environment leads to optimal transmit radar waveforms designed for specific target or target ensembles and conditions [37, 44-46, 64].

## 1.1 Matched Illumination Waveform Design

The design of transmission waveforms matched to specific targets has been the subject of numerous research efforts over the past decade and investigated from both signal-to-noise ratio (SNR) maximization and information-theoretic approaches [31-46, 64]. Target matched illumination approaches rely on target signature exploitation and require sufficient *a priori* information about the characteristics and properties of the target such as composition and shape. More explicitly, matched illumination techniques consider the design of an optimal detection system featuring a designed transmission waveform and corresponding matched filter receiver for a specific target under consideration. Furthermore, it maximizes the SINR at the output of the matched filter receiver for a designed transmitter-receiver pair and resultantly optimizes target detection by maximizing the Mahalanobis distance between target echoes [31].

To derive the matched illumination waveform, an extended target model is considered and can reasonably describe the radar problem as a linear system [31, 35]. The corresponding system model is shown below in Figure 1.2. Let $z(t)$ be the

transmission waveform illuminating the target and $s(t)$ be the target scattered field at some arbitrary point in the far field. Then,

$$s(t) = z(t) * q(t) \tag{1.1}$$

where $q(t)$ is the target impulse response and $(*)$ is the convolution operation. The same waveform convolved with the clutter response, $c'(t)$ yields the signal-dependent clutter return such that $c(t) = z(t) * c'(t)$. The signal received at the receiver is then

$$r(t) = s(t) + x(t) \tag{1.2}$$

where $x(t) = c(t) + n(t)$ represents the total undesired contribution of clutter and noise. After matched filtering the received signal, the output is

$$y(t) = b_{match}(t) * r(t) \tag{1.3}$$

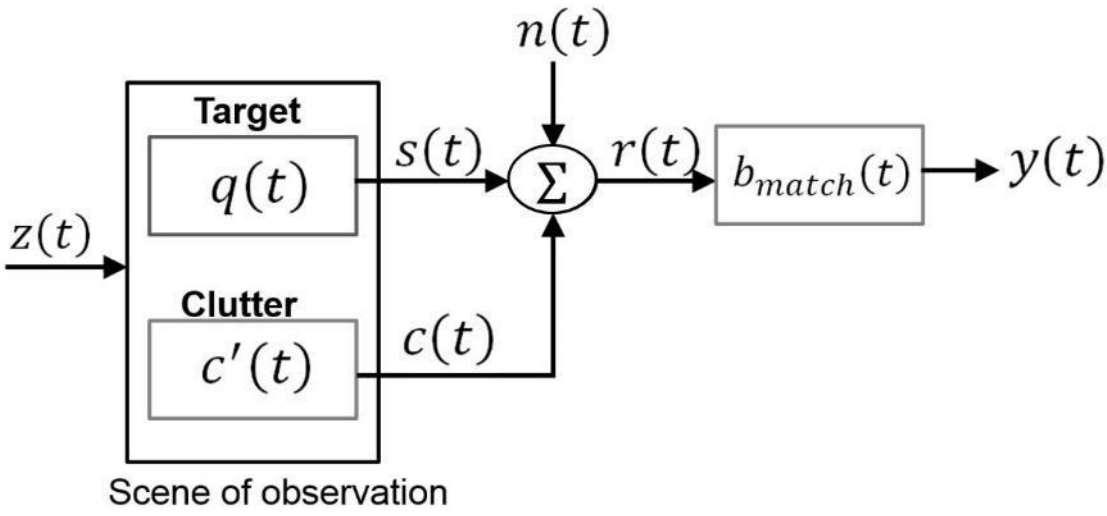


Figure 1.2 Block diagram of target model used in waveform design

The received signal comprises the reflection of the transmitted waveform from the target, the signal-dependent clutter, and additive thermal noise. If the target is absent, the receiver has only components from the clutter and noise and consequently represents less energy compared to the case when the target is present. Thus, in a stationary, white noise and clutter scenario, enhancing the receiver SINR leads to improved target detection.

To facilitate discrete-time implementation and for convenience of mathematical manipulation, the finite-duration functions of time representing the aforementioned target model (shown in Figure 1.2) are represented by their sampled, real-valued vectors. The transmission waveform $z(t)$ is given by $N$ equally spaced time samples separated by the time interval $\Delta t$ for some finite time duration $N\Delta t$, i.e., $\boldsymbol{z} \equiv [z_1, z_2, \dots, z_N]^T$. Likewise, the received target echo $s(t)$ is represented by the vector $\boldsymbol{s} = [s_1, s_2, \dots, s_M]^T$ where $M \geq N$ since the scattered energy is collected at the receiver for some duration greater than the active time of the transmitter. In principle, multiple reflections from the target can result in an infinite length impulse response. However, the energy due to these multiple reflections become negligible at some time length related to the transit time of the waveform across the target [35]. Accordingly, the target impulse response $\boldsymbol{Q}$ is an approximation and normally satisfactory for numerical implementation when having a finite size of $M \times N$.

Following the target model, an $M \times N$ target impulse response convolution matrix $\boldsymbol{Q}$ is defined with the samples (real-valued) of the target impulse response, i.e.,

$$\boldsymbol{Q} \equiv \begin{bmatrix} q_1 & 0 & \cdots & 0 \\ q_2 & q_1 & \cdots & 0 \\ \vdots & \vdots & \ddots & \vdots \\ q_N & q_{N-1} & \cdots & q_1 \\ q_{N+1} & q_N & \cdots & q_2 \\ \vdots & \vdots & \ddots & \vdots \\ q_M & q_{M-1} & \cdots & q_N \end{bmatrix} \tag{1.4}$$

The received target echo signal vector $\boldsymbol{s}$ of length $M$ can be expressed as the multiplication of the target convolution matrix $\boldsymbol{Q}$ with the $N$ length transmission waveform vector $\boldsymbol{z}$, i.e.,

$$\boldsymbol{s} = \boldsymbol{Q}\boldsymbol{z} \tag{1.5}$$

It is noted that obtaining an accurate target impulse response is vital to matched illumination techniques and typically unknown. Thus, (1.5) can be reformulated as a deconvolution problem to find the target impulse response vector of length $N$ if the input and output of the system are known, i.e.,

$$\boldsymbol{q} = [q_1, q_2, \ldots, q_N]^T = \boldsymbol{Z}^{-1}\boldsymbol{s} \tag{1.6}$$

where $\boldsymbol{Z}$ is the $M \times N$ convolution matrix containing the incident waveform that is identical in structure to $\boldsymbol{Q}$. The solution to this problem is not trivial and has been found to be ill-conditioned; hence, an approximation which minimizes the error must be found [65-68]. Further explanation of the deconvolution problem can be found in Appendix A.

Meanwhile, once the target impulse response is determined, the system output after matched filtering has the form

$$\boldsymbol{y} = \boldsymbol{b}_{\text{match}}^H \boldsymbol{r} = \boldsymbol{b}_{\text{match}}^H \boldsymbol{s} + \boldsymbol{b}_{\text{match}}^H \boldsymbol{x} \tag{1.7}$$

where $\boldsymbol{b}_{\text{match}}$ is the matched filter vector of length $M-1$ and $[\cdot]^H$ represent the Hermitian operator. The system outputs are now defined by the signal, $\boldsymbol{y}_s = \boldsymbol{b}_{\text{match}}^H \boldsymbol{s}$, and noise pulse clutter, $\boldsymbol{y}_x = \boldsymbol{b}_{\text{match}}^H (\boldsymbol{c}+\boldsymbol{n})$. The independence and zero mean assumptions of the target, clutter and noise signals imply that the received signal autocorrelation matrix is $\boldsymbol{R}_r \equiv E[\boldsymbol{r}\boldsymbol{r}^H] = \boldsymbol{R}_s + \boldsymbol{R}_x$, where $E[\cdot]$ is the expected value operator and $\boldsymbol{R}_s \equiv E[\boldsymbol{s}\boldsymbol{s}^H]$ and $\boldsymbol{R}_x = E[\boldsymbol{x}\boldsymbol{x}^H]$ are the autocorrelation matrices of the signal and the noise plus clutter, respectively. The $M \times N$ Hermitian-Toeplitz matrix $\boldsymbol{R}_x$ is the temporal autocorrelation of the noise plus clutter of the form

$$\boldsymbol{R}_x = \begin{bmatrix} r_1 & r_2 & \cdots & r_M \\ r_2^* & r_1 & \cdots & r_{M-1} \\ \vdots & \vdots & \ddots & \vdots \\ r_M^* & r_{M-1}^* & \cdots & r_1 \end{bmatrix} \tag{1.8}$$

in terms of the matrix elements

$$r_p \equiv \frac{1}{2\pi}\int_{-\pi}^{\pi}\{G_n(\omega) + G_c(\omega)|Z(\omega)|^2\}e^{j(p-1)\omega}d\omega \tag{1.9}$$

where $G_n(\omega)$, $G_c(\omega)$, and $|Z(\omega)|^2$ are the power spectral density functions for the noise, clutter, and the transmission waveform, respectively. In the case when noise is stationary and white ($G_n(\omega) = N_0$) and in the absence of clutter ($G_c(\omega) = 0$), the autocorrelation matrix $\boldsymbol{R}_r$ becomes diagonal with elements equal to the noise power $N_0$ and the matrix elements of (1.8) are independent of the transmission waveform frequency response $Z(\omega)$.

Here, the filter output SINR can be written in the form

$$\gamma = \frac{E[|\boldsymbol{y}_s|^2]}{E[|\boldsymbol{y}_x|^2]} = \frac{\boldsymbol{b}_{\text{match}}^H \boldsymbol{R}_s \boldsymbol{b}_{\text{match}}}{\boldsymbol{b}_{\text{match}}^H \boldsymbol{R}_x \boldsymbol{b}_{\text{match}}} \tag{1.10}$$

The optimum matched receiver filter $\boldsymbol{b}_{\text{match}}$ can be calculated by use of partial differentiation and written as the Weiner-Hopf equation [35]

$$\boldsymbol{b}_{\text{match}} = \boldsymbol{R}_x^{-1}\boldsymbol{s} = \boldsymbol{R}_x^{-1}\boldsymbol{Q}\boldsymbol{z}. \tag{1.11}$$

Substitution of (1.11) into (1.10) gives the SINR of the matched filter

$$\gamma_{\text{match}} \equiv \max_{\boldsymbol{b}_{\text{match}}} \gamma = \boldsymbol{s}^H\boldsymbol{R}_x^{-1}\boldsymbol{s}\ . \tag{1.12}$$

Further substitution of (1.5) into (1.12) permits the optimization of matched filter SINR to be with respect to the transmission waveform $\boldsymbol{z}$ via

$$\gamma_{\text{opt}} \equiv \max_{\boldsymbol{z}} \gamma_{\text{match}} \equiv \max_{\boldsymbol{z}} \boldsymbol{z}^H\boldsymbol{\Omega}\boldsymbol{z} \tag{1.13}$$

in terms of the target autocorrelation matrix $\boldsymbol{\Omega}$ defined by

$$\boldsymbol{\Omega} = \boldsymbol{Q}^H\boldsymbol{R}_x^{-1}\boldsymbol{Q}\ . \tag{1.14}$$

Obtaining the optimum transmission waveform is defined for two cases:

### 1.1.1 Case 1: Zero Clutter ($\boldsymbol{G_c(\omega) = 0}$ )

For the zero clutter case, $G_c(\omega) = 0$, the autocorrelation matrix of the noise plus clutter is independent of the transmission waveform; thus, the optimization problem reduces to the maximization defined in (1.13) with constraints that the optimum transmission waveform $\boldsymbol{z}$ is of finite duration and finite energy as well as being independent of the matrix $\boldsymbol{\Omega}$ of (1.14). As shown in [35, 40], the SINR $\gamma_{\text{opt}}$ is maximized if the transmission waveform $\boldsymbol{z}$ is proportional to the dominant eigenvector of the target autocorrelation matrix $\boldsymbol{\Omega}$ defined in (1.14). That is, $\boldsymbol{z} \propto \boldsymbol{v}$ given $\boldsymbol{\Omega v} = \Lambda\boldsymbol{v}$ where $\Lambda$ is the eigenvalue associated with the eigenvector $\boldsymbol{v}$.

### 1.1.2 Case 2: Non-zero Clutter ($G_c(\omega) \neq 0$ )

When the clutter is present, $G_c(\omega) \neq 0$, the noise plus clutter autocorrelation matrix $\boldsymbol{R}_x$ depends upon the power spectral density of the transmission waveform as shown in (1.9); hence, the optimum waveform which maximizes the SINR $\gamma_{\text{opt}}$ is found using either the eigen-waveform solution of [35,40] or the information-theoretic solution via a frequency domain waterfilling solution [69,70]. The waterfilling solution models the target impulse response as a Gaussian random process and the optimal waveform is derived through a maximization of the mutual information between a Gaussian distributed target ensemble and the received signal in clutter and noise. Meanwhile, the eigen-waveform solution is found by an iterative procedure described below [35]:

1. For initialization, $k = 0$, begin with an arbitrary, real causal temporal transmission waveform vector $\boldsymbol{z}_0$ of duration $t_0$ and energy $E_0 = \boldsymbol{z}_0^H \boldsymbol{z}_0$.
2. Let the Fourier transform $\boldsymbol{z}_k \leftrightarrow Z_k(\omega)$ and find the corresponding temporal autocorrelation matrix $\boldsymbol{R}_k$ using (1.8) and (1.9)
3. Compute the target autocorrelation target matrix $\boldsymbol{\Omega}_k$ using (1.14) in terms of $\boldsymbol{R}_k$ calculated in step 2 and the target impulse response convolution matrix $\boldsymbol{Q}$.
4. Find the dominant, normalized eigenvector $\boldsymbol{v}_1^k$ of the $\boldsymbol{\Omega}_k$ matrix.
5. Update the transmission waveform via the update rule, i.e.,

$$\boldsymbol{z}_{k+1} = \frac{\boldsymbol{z}_k + \epsilon_k \boldsymbol{v}_1^k}{\sqrt{\left(1+\frac{\epsilon_k}{\sqrt{E_0}}\right)^2 - \left(\frac{\epsilon_k}{\sqrt{E_0}}\right)^3}} \tag{1.15}$$

where $\epsilon_k$ is a meaningful measure of error at stage $k$ defined as

$$\epsilon_k = \sqrt{2\sqrt{E_0}\left(\sqrt{E_0} - \boldsymbol{z}_k^H \boldsymbol{v}_1^k\right)}\,. \tag{1.16}$$

6. Iterate until done. That is, let $\boldsymbol{z}_{k+1} \leftrightarrow Z_{k+1}(\omega)$ and go back to step 2 with $k$ replaced by $k+1$. Repeat until $\epsilon_k$ is sufficiently small. Hence, $\boldsymbol{z}_{\text{opt}} = \lim_{k\to\infty} \boldsymbol{z}_k$.

Both approaches (waterfilling and eigen-solution) give optimum waveforms which enhance the matched filter receiver SINR, but they should be favored for different circumstances. Assume that only one transmission waveform is available for a particular target detection problem. The waterfilling solution tends to spread the waveform energy out as it tries to encompass the spectral variance of the Gaussian target ensemble. Intuitively, this could yield good results if the target's impulse response doesn't match as well as expected because its composition, orientation, or shape is effectively different than the assumed target. On the other hand, the eigen-solution places a significant portion of its energy into one or two narrow bands and will perform better than the waterfilling solution as long as the target's impulse response closely resembles the expected impulse response.

## 1.2 Application of Matched Illumination for Target Classification

The matched illumination waveform is designed to maximize the probability of target identification and classification as well as optimize target detection (increase SNR) [35, 40]. To maximize the probability of correct target classification, the Mahalanobis distance between two target echoes can be maximized, i.e.,

$$maximize\ \eta^2 = \left(\boldsymbol{s}_\alpha - \boldsymbol{s}_\beta\right)^H \boldsymbol{R}_x^{-1}\left(\boldsymbol{s}_\alpha - \boldsymbol{s}_\beta\right) \tag{1.17}$$

where $\boldsymbol{s}_\alpha$ and $\boldsymbol{s}_\beta$ are the vectors corresponding to the echoes from targets $\alpha$ and $\beta$, respectively, $\eta^2$ is the Mahalanobis distance, and $\boldsymbol{R}_x$ is the Hermitian-Toeplitz autocorrelation matrix of the noise and clutter. For optimal detection, the SINR is optimized in (1.10) - (1.13) and similarly, the Mahalanobis distance is optimized (maximized) following the same method and presenting (1.10) in terms of the targets' impulse response

$$\eta^2 = \boldsymbol{z}^H \boldsymbol{\Omega} \boldsymbol{z} \tag{1.18}$$

where the targets' impulse response autocorrelation matrix is

$$\boldsymbol{\Omega} = \left(\boldsymbol{Q}_\alpha - \boldsymbol{Q}_\beta\right)^H \boldsymbol{R}_x^{-1} \left(\boldsymbol{Q}_\alpha - \boldsymbol{Q}_\beta\right). \tag{1.19}$$

Thus, the Mahalanobis distance is maximized through the use of the optimum discriminating waveform obtained following the previously discussed zero/non-zero clutter case solutions.

## 1.3 Chapter Summary

It is clear that TWR imaging is a challenging problem. As previously discussed, current research is investigating model-based reasoning approaches to combat the adverse effects of the wall. Meanwhile, the transmission waveform is critical to the performance of radar systems, and using model-based reasoning to design transmit waveforms for TWR applications can be accomplished with matched illumination waveform design. The matched illumination waveform optimizes the target return in the given environment based on the target signature by optimally placing the spectral energy of the waveform. Often in target identification and detection, the target and environment are known *a*

*priori* and can be characterized accurately. With advanced knowledge of the radar target and environment, exploiting both the known target impulse response and wall transmission properties can enhance target detection. The resulting matched illumination waveform then emphasizes the target information through the wall while suppressing clutter and noise of the environment.

Specifically, radar performance enhancements that can be created through model-based, waveform design techniques in TWR utilizing matched illumination theory is investigated in this work. Applying matched illumination waveform design to TWR systems is detailed in Chapter 2. Also, the impacts of wall-target interaction on matched illumination waveforms are presented in Chapter 2. To ensure accuracy of designed transmit waveforms using model-based reasoning techniques, the wall's composition is investigated and the impacts that a wall's moisture profile has on resulting matched illumination waveforms is presented in Chapter 3.

Because this work shows that moisture profiles within walls impact the waveform design process, it is clear that accurate wall models must be used when using model-based approaches. The success of TWR utilizing matched illumination theory depends on the *a priori* knowledge of the target and environment; thus, careful consideration must be given to not only the target but also the wall. Unfortunately, literature detailing accurate properties of wall materials is lacking, and is severely limited in terms of moisture content within wall structures. Chapter 4 aims to contribute information concerning the moisture profile present within walls by presenting moisture measurements taken for an adobe wall and correlating the moisture content to accurate dielectric property values. Finally, in Chapter 5, the moisture profile measurement and

corresponding dielectric properties are validated through radar measurements taken on a through-wall radar problem consisting of an adobe wall and aluminum plate target. By taking radar measurements of the through-wall problem with the adobe wall, the results can be compared to simulation and the measurements can be verified as well as validation of the transmitted matched illumination waveform's radar performance increase. Also noted in the study is the ability to transmit the optimal waveforms using a simple radar system, rather than needing to rely on expensive, arbitrary waveform generators.

# CHAPTER II

## ACCURARCY OF MATCHED ILLUMINATION WAVEFORM DESIGN

In this chapter, the impacts of wall-target interaction on matched illumination waveforms for TWR are examined via finite-difference time-domain (FDTD) simulations. Returns from various wall-target scenarios are considered as a function of the target-to-wall separation in order to examine the effectiveness of the so-called *primary-wave* target response in the matched illumination implementation. The primary-wave target response is shown to effectively maximize the SINR in through-wall radar applications where the wall-target interaction is minor and the primary-wave response closely resembles the full-wave target response which contains all wall-target interactions. The ability of the primary-wave target response to maximize the SINR can be degraded by relatively minor errors in the wall-target transfer function caused by the incomplete wall-target physics inherent to the scheme. In such cases, the resulting matched illumination waveform spectrum is generally characterized by narrowband energy concentrated at suboptimal frequencies.

Because the success of TWR utilizing matched illumination theory depends on the *a priori* knowledge of the target and environment, careful consideration must be given to wall and target interaction. In [31-36, 75, 87-88], the matched illumination waveform is derived using only the individual impulse response of the target and the transmission impulse response of the wall. This method is very attractive for its

simplicity as well as its flexibility. That is, once a target's impulse response and wall transmission impulse response is found, an optimal waveform can be derived quickly for a variety of wall-target scenarios and positions rather than having to complete a full simulation for every scenario of a wall-target combination in order to derive the impulse responses of the wall and target. However, an assumption that the target-wall interaction is minimal is inherent to the matched illumination waveform design scheme, so the target return from this matched illumination waveform is designated as the primary-wave target response. The target return from a matched illumination waveform determined by including all wave physics is designated as the full-wave target response.

This section investigates the relative performance of primary-wave and full-wave matched illumination waveforms using conducting cylinder targets behind lossless and lossy homogeneous walls. The ability of the primary-wave and full-wave matched illumination waveforms to maximize the SINR of the return is examined as the separation distance between the target and the wall is varied.

## 2.1 Application of Matched Illumination Waveform Design to TWR

Matched illumination waveforms were originally developed to improve the detection of low observable aircraft and ground-based vehicles [35,46]. More recently, the matched illumination technique has been extended for target detection and identification in TWR applications [31-36, 75, 87-88]. In TWR applications, typical indoor targets and walls can be defined and modeled *a priori*. This is a safe assumption given that often in surveillance missions, there is a known target of interest and generally wall composition is consistent in a given region and therefore can be easily obtained or assumed. If the wall thickness is completely unknown and the radar system cannot infer

the proper thickness, recent research has shown agreement in the use of microwave measurement techniques relying only on time delay measurements from different receiver positions to accurately determine wall thickness [71-74]. Subsequently, the target optimum waveform(s) for TWR may be designed off-line and be ready for emission with system deployment.

The matched illumination waveform technique serves TWR applications well through easy adaptation to different environments and/or targets, as opposed to inverse filtering. For example, consider a scene that includes a particular wall and target. If the transfer function of the complete scene (Fourier transform of the complete scene impulse response) is known, the SINR may be increased by radiating a waveform which equalizes the frequency response. However, the transfer function of the complete scene would need to be recalculated each time the relative position between the wall and target is changed, which would be computationally expensive and inefficient. Conversely, the matched illumination waveform is derived using only the impulse responses of the wall and the target, resulting in a robust and efficient process to determine the optimal waveform. Given a library of wall transmission impulse responses and target impulse responses, an optimal waveform can be derived quickly and efficiently for a particular wall-target combination at any relative spacing. That is, a complete simulation for every scenario of a wall-target combination is not required.

Derivation of the matched illumination waveform for use in TWR utilizes a linear, time-invariant target model as previously discussed; however, the wall response is now incorporated into the target model. To account for the walls, the target model in Figure 1.2 can be extended as described in Figure 2.1 where $q(t)$ and $w(t)$ are the

impulse responses of the target and wall, respectively. The wall impulse response includes only transmission characteristics [31-35, 75, 87-88] so that reflections from the wall are not utilized in the waveform optimization.

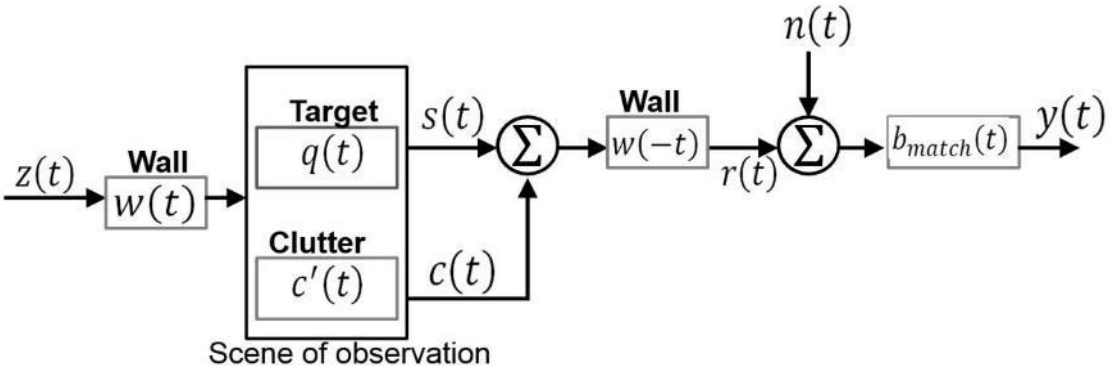


Figure 2.1 Block diagram of target model for TWR

With the addition of the wall, the received target echo $s(t)$ is expressed as

$$s(t) = z(t) * w(t) * q(t) * w(-t) \tag{2.1}$$

where $w(-t)$ is the transmission impulse response of the wall in the reverse direction. The forward and reverse transmission properties of the wall may be symmetric ( $w(t) \equiv w(-t)$ ) such as in the case of uniform, homogeneous wall composition or asymmetric ( $w(t) \not\equiv w(-t)$ ) such as in the case of more realistic wall models featuring non-symmetric dielectric properties along the path of wave propagation. In this case, special attention should be made to obtain both the forward and reverse wall transmission impulse response.

Following the target model of Figure 2.1, the combined wall/target impulse response $u(t)$ replaces the target only impulse response $q(t)$ and is represented by

$$u(t) = w(t) * q(t) * w(-t) \tag{2.2}$$

and arranged to form the wall/target convolution matrix $\boldsymbol{U}$ which has the same structural form as (1.4). The combined wall/target autocorrelation matrix becomes $\boldsymbol{\Omega}_w = \boldsymbol{U}^H \boldsymbol{R}_x^{-1} \boldsymbol{U}$ and the optimum waveform is obtained in the same manner previously discussed in the zero/non-zero clutter cases. Again, the Mahalanobis distance is maximized through the use of the matched illumination waveform, which in the presence of the wall, $\boldsymbol{Q}_\alpha$ and $\boldsymbol{Q}_\beta$ from (1.19) are replaced by the combined wall/target convolution matrix $\boldsymbol{U}_\alpha$ and $\boldsymbol{U}_\beta$ composed of elements $u_\alpha(t) = w(t) * q_\alpha(t) * w(-t)$ and $u_\beta(t) = w(t) * q_\beta(t) * w(-t)$ for targets $\alpha$ and $\beta$.

## 2.2 Simulation

The wall transmission impulse response $w(t)$ in (2.1) only models the forward propagation of waves through the wall, which includes the initial forward traveling wave along with all multiple bounces within the wall that exit the wall in the forward direction. Accordingly, the wall transmission impulse response in the reverse direction $w(-t)$ only models the propagation of scattered waves through the wall in the reverse direction. Thus, the received target echo determined using (2.1) ignores the following wave components: (a.) all wall-only reflections involving reverse propagation on the radar side of the wall and (b.) all target reflections resulting in forward propagation on the target side of the wall (target reflections that are reflected by the wall back to the target). To illustrate the components of the received through-wall target echo and what components are neglected, Figure 2.2 details the components of the applied responses which consist of the wall transmission impulse response (green solid lines) and the through-wall target

echo (black solid lines). The neglected components, (a.) and (b.), are shown as dashed lines and are the wall only reflection (black dashed lines) and the wall-target interactions (red dashed lines), respectively. The through-wall target echo determined using (2.1) defines the primary-wave target impulse response. The complete full-wave solution for the wall-target radar echo minus the wall-only echo components defines the full-wave target response.

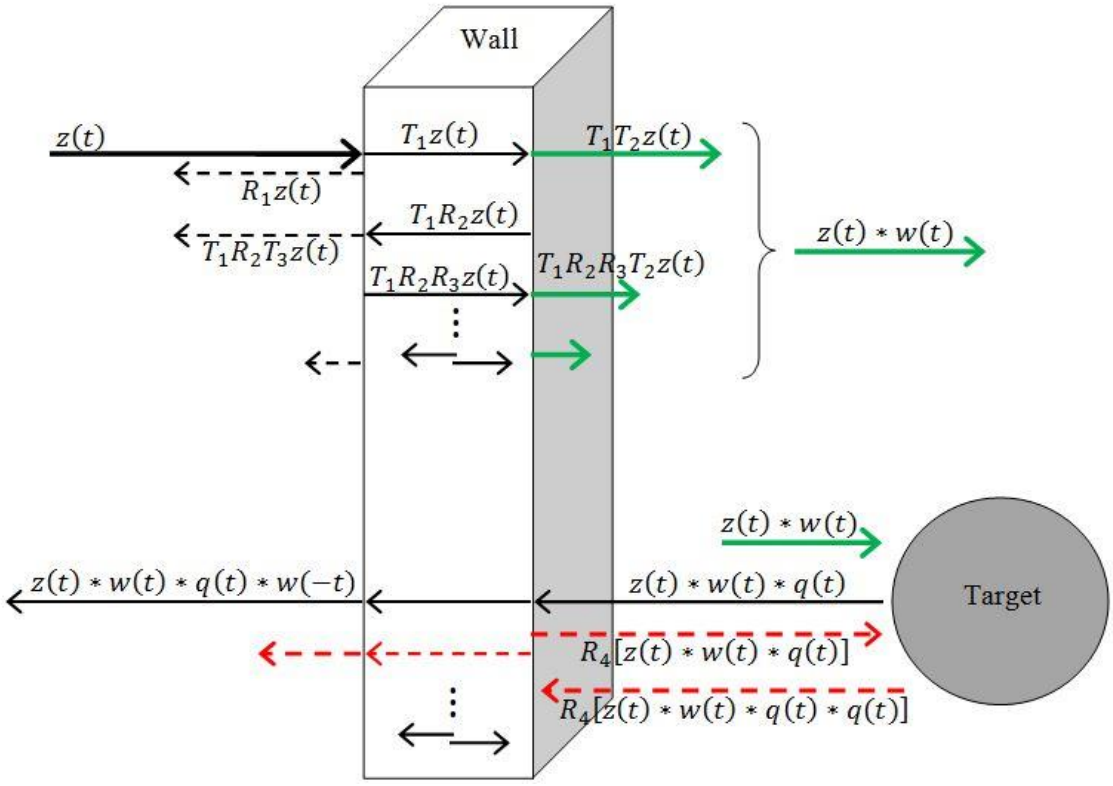


Figure 2.2 Components of wall-target radar problem where $T$ represents the transmission at an interface and $R$ represents the reflection at an interface

The differences in the primary-wave and full-wave target responses are demonstrated using a monostatic radar system that illuminates a conducting cylindrical

target located behind either a lossless or lossy homogeneous wall as shown in Figure 2.3. The impulse response required for the primary-wave target response and the complete radar environment model required for the full-wave target response are modeled with the *Angora* FDTD simulation package [86]. The targets are illuminated with a differentiated Gaussian pulse containing energy over the 0.1 to 6.5 GHz band. The incident waveform and resultant scattered fields were both bandpass filtered with a passband from 0.9 to 4 GHz in order to consider only the commonly used frequency range which has been shown to provide desirable tradeoffs between signal attenuation, scene resolution, and antenna size for TWR [1]. The wall-to-target separation distance $D$, the cylinder sizes, and the wall transmission properties (lossless/lossy) are all varied in the comparison of the primary-wave and full-wave target responses. Three hollow conducting cylinders of lengths $L_1 = 52$ mm, $L_2 = 114$ mm, and $L_3 = 230$ mm are considered each with an outer diameter of 16 mm and an inner diameter of 9 mm and displayed in Figure 2.3. Each target is located behind a lossless or lossy homogeneous wall of infinite extent (wall thickness = 0.2 m, $\varepsilon_r = 6$, $\sigma_1 = 0$ S/m $\sigma_2 = 0.1$ S/m). The axes of the cylinder targets are aligned with the electric field of the incident waves, and the target and wall are in the far-field of the antenna.

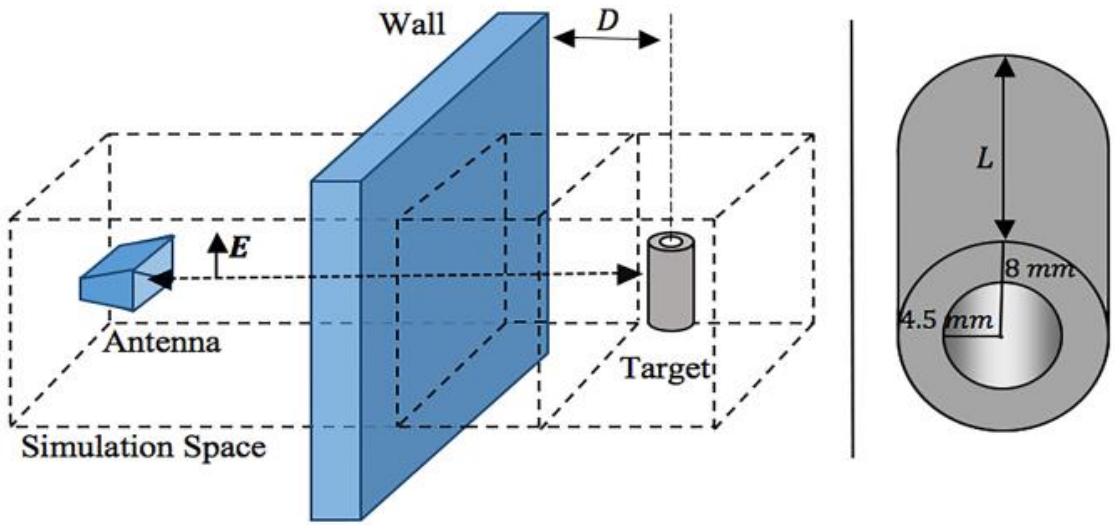


Figure 2.3 Geometry of wall and cylinder simulations with expanded view of cylinder

Matched illumination waveforms are then derived using full-wave and primary-wave target responses as described in Section 2.1 and utilized in [31-36, 75, 87-88]. Differences in the matched illumination waveforms resulting from the full-wave and primary-wave target responses can be found by direct examination of the waveforms themselves, or by comparing the SINR at the receiver matched filter output due to the matched illumination waveforms. To compare the performance of different matched illumination waveforms, the input SNR is fixed to the matched filter in all cases. The noise variance is $\sigma^2 = P_{\max}/10^{\frac{SNR_{\text{in}}}{10}}$ where $P_{\max}$ is the highest power of the received signal, and $SNR_{\text{in}}$ is assumed to be 10 dB. All waveforms are assumed to be of equal duration and contain equivalent total energy.

It should be noted that only normal incidence is considered in this study in order to simplify the comparison of primary-wave and full-wave target responses. The uncertainty of the target aspect would be a major factor in the actual performance of a

given matched illumination waveform. The orientation of the target with respect to the radar needs to be known or obtained *a priori* in order to achieve maximum waveform performance for a specific target, which is not always possible. However, given the stationary nature of many targets over a long observation time, the radar can cycle through a bank of matched illumination waveforms for a given target at different aspect angles, resulting in the highest SINR at the output of the matched filter corresponding to the actual target orientation.

## 2.3 Results and Performance Analysis

The matched illumination waveform of a given wall/target combination, when subjected to white noise and zero clutter, is characterized by energy concentrated at frequencies where the individual responses of the wall and target tend to align. It is therefore useful to examine the spectral characteristics of the wall/target impulse response (i.e., the wall/target transfer function) when comparing the primary-wave and full-wave results. The transfer functions of the primary-wave and full-wave impulse responses are shown in Figure 2.4 for a cylinder of length $L_3 = 230$ mm behind a lossy wall for different values of wall-to-target separation distance. Differences are noted in the primary-wave and full-wave transfer function spectra relative to both amplitude and frequency content. The primary-wave transfer functions exhibit a common spectral shape at all target-to-wall spacings, as opposed to the full-wave transfer functions which show more variation in spectral shape with spacing. Note that the primary-wave transfer functions have a common peak value at approximately 1.75 GHz for all target-to-wall spacings, while the peak values of the full-wave transfer functions peak at approximately 1.75 or 3.0 GHz, depending on the target-to-wall spacing. The differences in the spectral

characteristics of the primary-wave and full-wave transfer functions lead to different matched illumination waveforms, which typically take the form of one or more narrowband components.

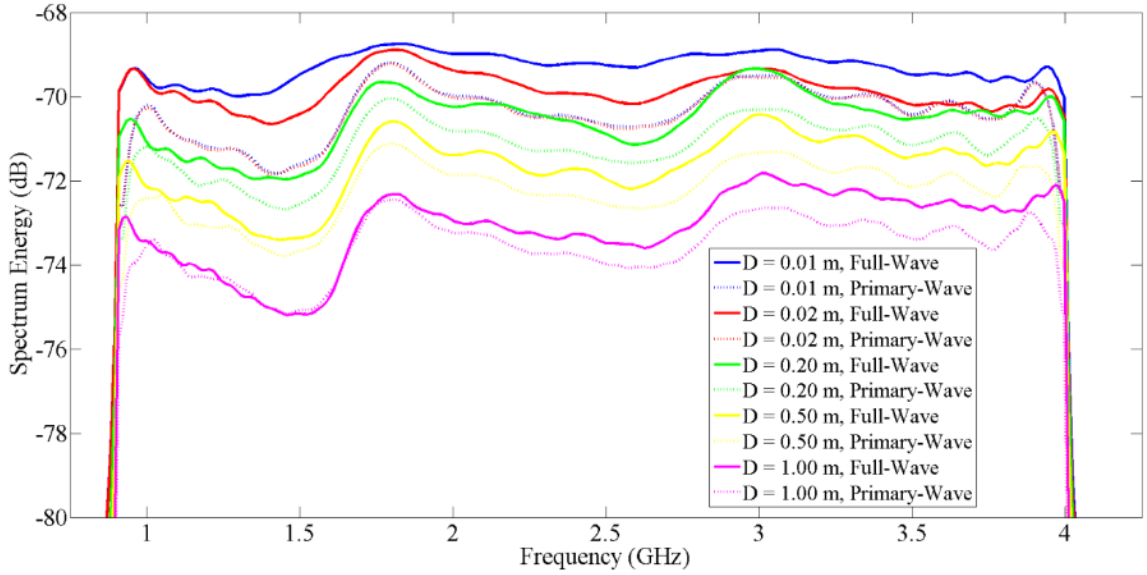


Figure 2.4 Transfer functions of full-wave and primary-wave wall-target impulse responses for the 230 mm cylinder located at a distance $D$ behind a lossy, homogeneous wall

The spectra of the matched illumination waveforms generated from primary-wave and full-wave wall-target impulse responses for a cylinder at a distance of $D = 1$ m behind a homogeneous wall are shown in Figure 2.5 for all three cylinder lengths (52, 114, and 230 mm) and both wall types (lossless and lossy). In general, the full-wave optimum waveforms for a given cylinder are quite similar for both lossless and lossy walls, with minor frequency shifts in the narrowband components, while the primary-wave optimum waveforms can be located at significantly different frequencies for a lossless and lossy wall as seen for the 114 mm cylinder. When the primary-wave and

full-wave optimum waveforms are compared, significant differences in the frequencies of the optimum waveforms are seen. The primary-wave and full-wave optimum waveforms for the 114 mm cylinder are separated by approximately 300 MHz, while those of the 230 mm cylinder are separated by approximately 1.2 GHz.

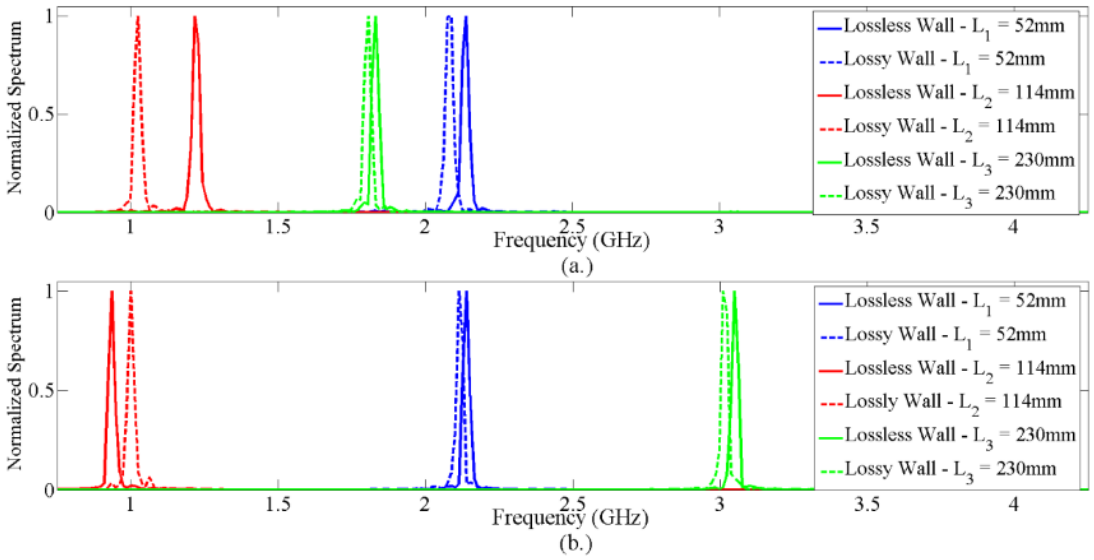


Figure 2.5 Matched illumination waveforms for cylinder targets located at $D$ =1.0 m behind lossless and lossy walls

(a.) Optimal waveforms derived from primary-wave transfer functions
(b.) Optimal waveforms derived from full-wave transfer functions

The effectiveness of a matched illumination waveform is measured by the resulting SINR for a given wall/target combination. The SINR levels for the matched illumination waveforms derived from the primary-wave and full-wave target responses of the three cylinder lengths at varying wall-target separation distances are determined and compared for both lossless and lossy walls. The difference in the SINR levels obtained for the primary-wave and full-wave matched illumination waveforms, designated as $\Delta SINR$, is defined in units of dB as

$$\Delta SINR_{\mathrm{dB}} = 10\log_{10}\left(\frac{SINR_{fw}}{SINR_{pw}}\right) = \left(SINR_{fw}\right)_{\mathrm{dB}} - \left(SINR_{pw}\right)_{\mathrm{dB}} \tag{2.3}$$

where $SINR_{fw}$ and $SINR_{pw}$ are the SINR levels determined from the full-wave and primary-wave responses, respectively. The value of $\Delta SINR$ is shown in Figure 2.6 for the three cylinder targets located behind lossless and lossy walls as the target-to-wall separation is varied. In general, larger values of $\Delta SINR$ are seen for larger cylinder sizes at larger target-to-wall separations. It should be noted that the maximum values of $\Delta SINR$ (worst performing matched illumination waveforms obtained from primary-wave transfer functions) are seen in cases where the spectral energy of the waveform is focused at suboptimal frequencies, when compared to the frequencies present in matched illumination waveforms obtained from the full-wave transfer functions.

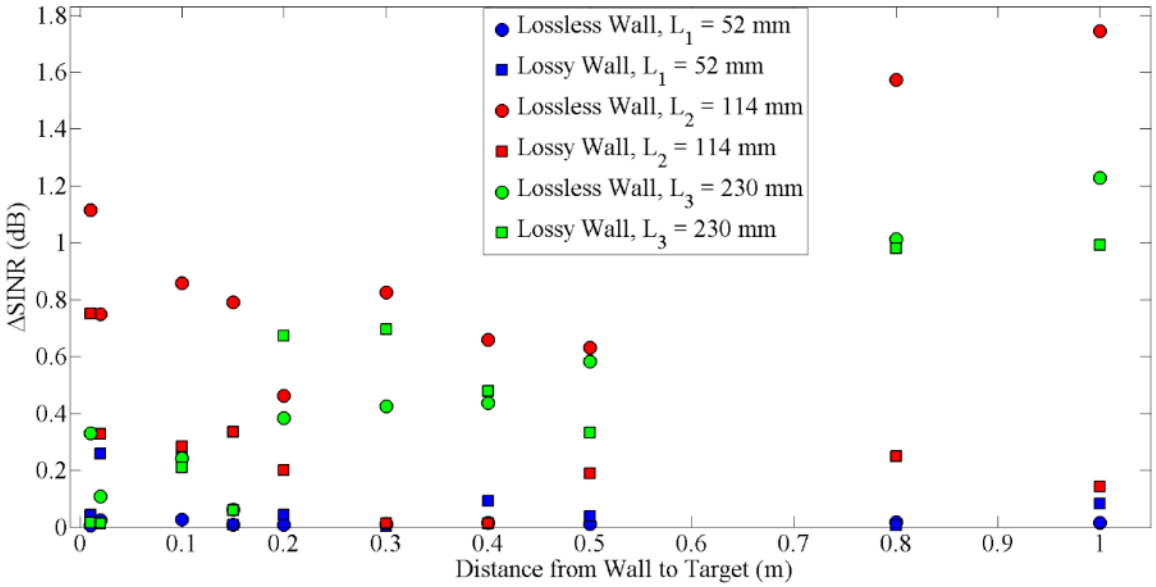


Figure 2.6 $\Delta SINR$ vs. target-to-wall separation distance for the three cylinder targets behind lossless and lossy walls

## 2.4 Chapter Summary

The impacts of wall-target interaction on matched illumination waveforms for TWR have been examined in this chapter. The returns from wall-target scenarios with varying target sizes, wall-to-target distances, and wall types were used to demonstrate the effectiveness and limitations of the so-called primary-wave wall-target response in the matched illumination implementation. The primary-wave wall-target response has been shown to effectively maximize the SINR in through-wall radar applications where wall-target interaction is minor and the primary-wave wall-target transfer function is an accurate representation of the full-wave wall-target transfer function. However, the SINR performance of matched illumination waveforms based on the primary-wave wall-target response can be degraded by relatively minor errors in the wall-target transfer function caused by the incomplete wall-target physics inherent to the scheme. In such cases, the resulting matched illumination waveform spectrum is generally characterized by narrowband energy concentrated at suboptimal frequencies.

As seen through this study, accurate impulse response information is critical to the performance of the optimal waveform. Thus, the impacts that the wall moisture profile has on resulting matched illumination waveforms are investigated next in Chapter 3. The optimal waveforms derived from matched illumination theory tend to be narrowband signals; thus, it is necessary that highly accurate impulse response information be calculated or derived through accurate measurement and modeling. The effects of improper wall modeling are illustrated through the study of wall moisture profiles effect on matched illumination waveforms radar performance.

# CHAPTER III

# IMPACTS OF WALL MOISTURE PROFILE ON WAVEFORMS

The forward and reverse transmission properties of the wall play a key role in TWR and must be characterized accurately to effectively implement the matched illumination technique. Typically, homogeneous walls are utilized in TWR studies, but this assumption may be inadequate for walls with significant variation in electrical properties in the direction of wave transmission. Failure to accurately model the attenuation and dispersion effects as a function of depth into the wall could result in matched illumination waveforms that are significantly suboptimal for the actual radar environment. This chapter focuses on the characteristics of matched illumination waveforms for particular wall moisture profiles.

Due to construction differences and environmental changes, the wall's composition can vary greatly. Electrical permittivity of walls can (for the most part) be properly estimated and measured for materials through techniques utilizing SAR and time of arrival processing; however, these measurements assume a homogeneous material and consequently, the material must maintain a fairly constant level of permittivity in order for the estimations to remain accurate [51, 89-92]. Unfortunately, typical wall materials such as wood, concrete, and adobe contain distributions of moisture content within their structure which resultantly causes variations to permittivity levels [53-54, 59-60, 62]. Thus, the assumption of constant levels of permittivity throughout the material is not

valid in general. Accordingly, the models representing the wall should address such changes in moisture because water within the material will result in changes of dielectric properties. With models updated to include the moisture profile and corresponding dielectric properties, an understanding of the effects of moisture profiles on matched illumination waveforms is needed and presented in this chapter.

## 3.1 Numerical Simulations

Measurement of actual moisture content and correlating dielectric properties for real walls under specific environmental conditions has yet to be fully explored, and no extensive information has been found in the open literature regarding this topic. Thus, in this chapter, we consider representative wall moisture profiles that exhibit general shapes characteristic of particular environmental conditions as shown in the conductivity profiles of Figure 3.1.

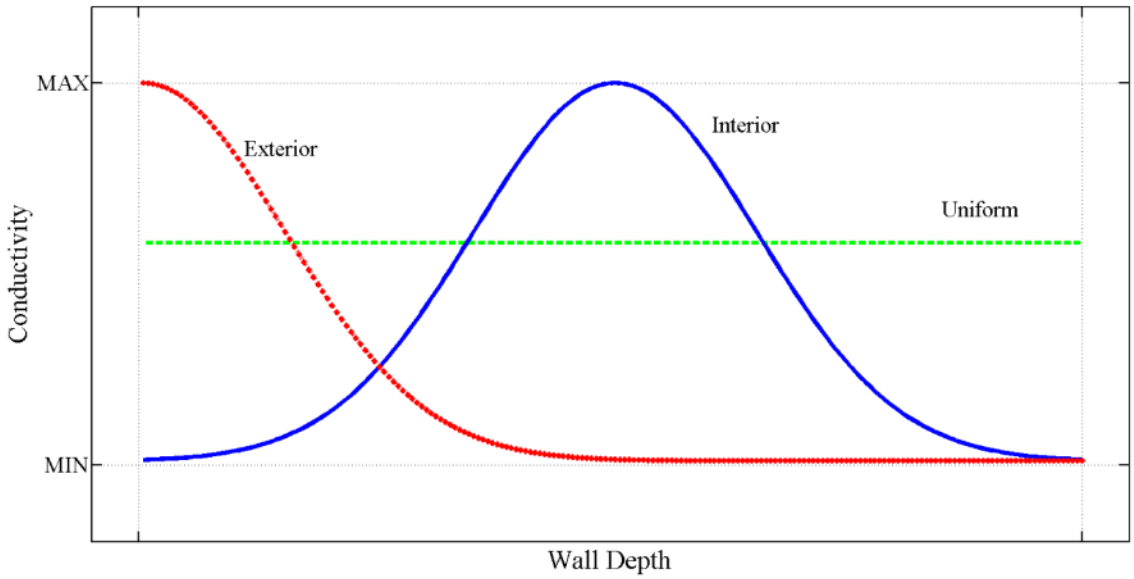


Figure 3.1 Wall conductivity/moisture content profiles

The *uniform* conductivity profile represents a wall that has been exposed to a constant environment over a long period of time, such that the moisture content is basically uniform throughout. The *interior* conductivity profile is representative of a wall that has dried over time at both its interior and exterior surfaces. The *exterior* conductivity profile represents a wall exposed to high humidity levels or precipitation on the exterior surface. Certainly, more complex profiles are probable, such as that seen in the case of a wall that experiences different rates of interior and exterior drying. However, with the lack of extensive information available to direct the correct profile shape, the profiles considered here are investigated to illustrate the need of more accurate wall models in the circumstance of non-uniform moisture profile.

The target and wall impulse responses required to determine the matched illumination waveform are computed using the Angora FDTD simulation package [86]. The heterogeneous wall conductivity profiles are modeled by creating a system of $M$ homogeneous layers. The number of layers required to ensure accurate results is found by iteratively computing the change in transmission signatures as the number of layers is increased until a sufficiently small change is found for a given FDTD cell dimension. The Angora simulation software is particularly effective at handling this type of wall model since it allows for multiple layers of infinite extent. The representative wall models are shown in Figure 3.2 as modeled by Angora. Each layer is modeled such that the material extends through not only the absorbing boundaries but also the total-field/scattered-field (TFSF) boundary. This is beneficial for the FDTD problems encountered here because the simulation space can be reduced to efficiently solve for the

scattered fields introduced by an incident plane wave without further processing required to neglect the edge effects of the wall.

A monostatic radar system consisting of a target (wooden table) behind a wall model (heterogeneous or homogeneous) was modeled with Angora to demonstrate the effects of wall moisture profiles on the resulting matched illumination waveforms. The conductivity profiles shown in Figure 3.1 were implemented in the wall model according to the wall/target geometry shown in Figure 3.3. The frequency-dependent characteristics of the complex permittivity for the individual layers that compose the wall model are defined using an extended Debye model for a given moisture level [49-50, 60]. The dielectric property (permittivity) ranges investigated in this work follow measured and estimated results in [49] for concrete and sand at different levels of moisture saturation and contain the following values: $6 \leq \varepsilon_r \leq 28$ , $0.0 \leq \sigma \leq 1.0\ S/m$.

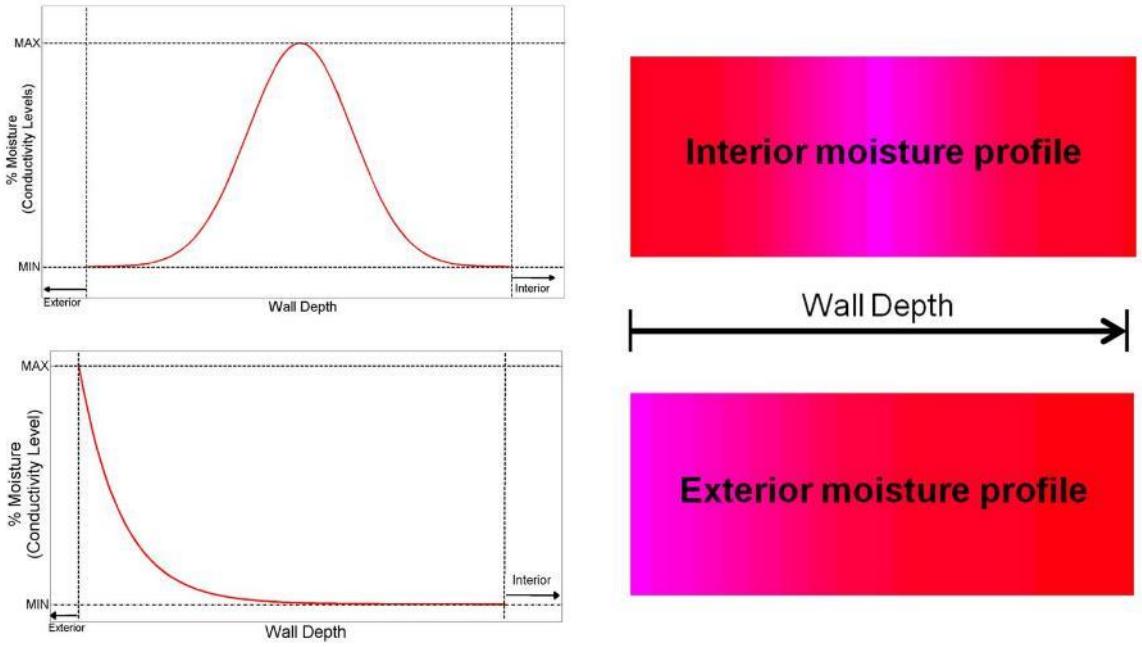


Figure 3.2 Representative heterogeneous walls as modeled in Angora

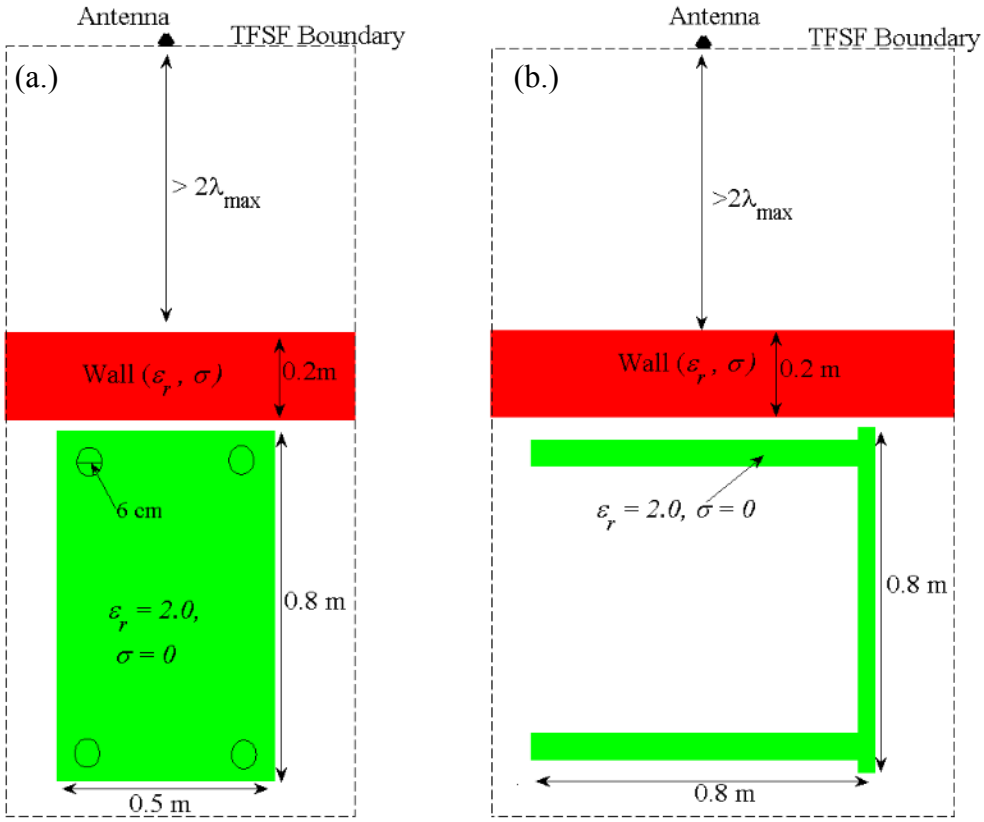


Figure 3.3 Geometry of wall and table simulation

(a.) $xz$ dimensions
(b.) $yz$ dimensions

It is assumed that the transmitter/receiver pair is located in the far zones of the targets for the frequencies considered. For each wall model and target, the scattering field was computed for a linearly polarized ($E_x$) incident waveform at incident angles from 0° to 60° with 5° increments in the $xz$ plane. That is, using the spherical coordinate system, the incident waveform was transmitted at polar (zenith) and azimuth angles of $120° \leq \theta \leq 180°$ and $\phi = 0°$, respectively. For all incident waveforms, the incident vector $\boldsymbol{k}$ is set at $\phi = 0°$ so that the waveform travels in the $+z$ direction. The coordinate

system with an incident waveform directed at $\theta$ =180° and having an aspect angle of 0° is shown in Figure 3.4 where $\psi$ is the polarization angle of the electric-field unit vector and measured from $\xi$ to $\eta$ so that $\psi = 90°$ which yields $E_x$ polarization. Maxwell's equations dictate that the electric field is perpendicular to the incidence vector $\widehat{\boldsymbol{k}}$. In order to define the orientation of the electric vector unambiguously, a local coordinate system is defined such that $\hat{\xi} = \widehat{\boldsymbol{k}} \times \hat{z}$ and $\hat{\eta} = \hat{\xi} \times \widehat{\boldsymbol{k}}$ . The unit vectors $(\hat{\xi}, \hat{\eta})$ are perpendicular to each other and lie in the plane perpendicular to the incident vector $\widehat{\boldsymbol{k}}$.

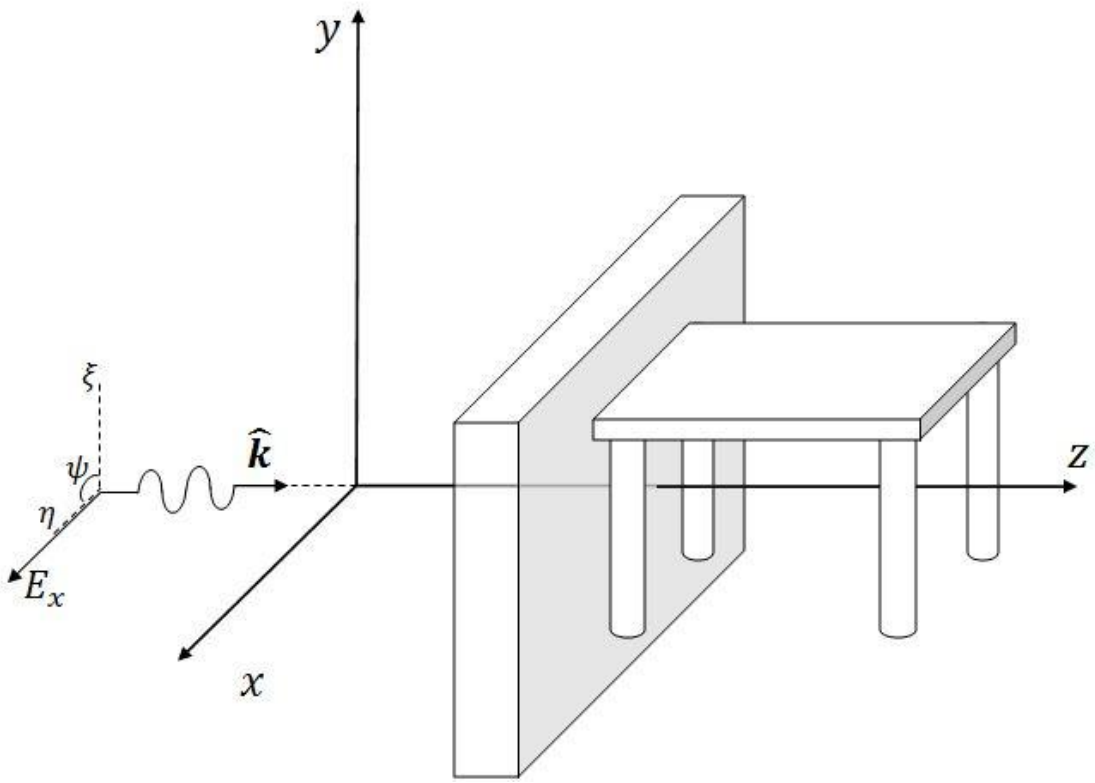


Figure 3.4 Geometry of simulations illustrating incident waveform

The transmission impulse response of the wall as well as the scattering impulse response of the table were found by illuminating each in free space with a differentiated Gaussian pulse containing energy over the 0.1 to 6.5 GHz band and deconvolving the incident waveform from the scattered field [65-68]. Deconvolution of the impulse response is not trivial and complicated by the presence of an ill conditioned matrix in the deconvolution process. A brief discussion of techniques used for deconvolution can be found in Appendix A. The incident waveform and resultant scattered fields were both lowpass filtered with a cutoff frequency equal to 6.5 GHz in order to keep the frequency range within the range of interest as well as neglect energies at the near-zero, high frequency content of the incident waveform which could lead to error in the impulse response derivation.

## 3.2 Simulation Results

The results below illustrate the impacts of the wall moisture profile on matched illumination waveforms. First, the transfer functions of the walls and targets illustrate the spectral location of the signal energy and provide a clear illustration of how the matched illumination process optimally designs a transmission waveform. Then, the SINR is computed for the various wall models and conclusions are made about the performance of the optimal matched illumination waveforms.

### 3.2.1 Comparison of Transfer Functions

To begin discussion of the simulation results, it is first noted that the matched illumination waveforms are highly aspect angle dependent due to radar targets yielding significantly different impulse responses for different orientations. Yet, this aspect angle

dependency is for the most part target based. The wall's impulse response was shown to remain relatively similar in terms of its impulse response when subjected to different incident angles. The transfer functions (Fourier transforms of impulse responses) for the wall models and the table target are shown in Figures 3.5-3.12 on a normalized scale for the homogeneous (uniform) and heterogeneous (interior and exterior) wall models, respectively. An inspection of the wall and target transfer functions is beneficial to illustrate where peaks in the transfer functions align, which determines the frequency band(s) yielding the strongest response for the given wall/target scene. Intuitively, the transmitted waveform should contain significant amounts of signal energy at these frequencies to improve the SINR.

As seen in Figures 3.5-3.6, the aspect angle mainly affects the target response rather than the wall response. For the uniform wall in Figure 3.5, the transfer function ultimately retains its shape and does not alter dramatically except for the magnitude of the transfer function. There are slight changes in the location of the peaks and nulls at the higher frequencies, but they are minor in comparison to the target's peak and null movement arising from the transmission incidence angle. The slight change of the wall transfer function with respect to aspect angle as seen with this wall model is consistent with all wall models considered in this study. As expected, the significant alteration of transfer function with respect to aspect angle is seen for the target response. In Figure 3.6, the target's transfer function for varying aspect angles are shown with a square point located at the peak of the given function. Here, the peaks move significantly across the frequency spectrum and the transfer functions are not closely related to one another in terms of overall shape; consequently, the target's orientation should be very accurate

when considering the design of transmitting matched illumination waveforms to achieve optimal detection performance. However, as previously stated, the uncertainty of target orientation can be overcome by cycling through all possible waveforms for a given target of interest.

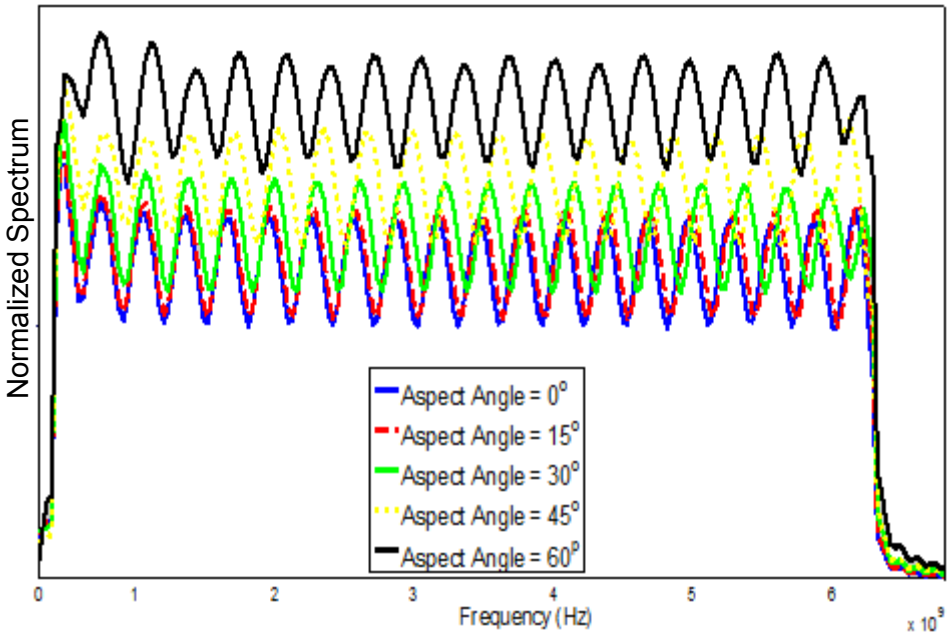


Figure 3.5 Uniform wall model transfer function for different aspect angles

Note: Wall shown in the figure has dielectric properties of $\varepsilon_r = 6,\ \sigma = 0.5\ S/m$

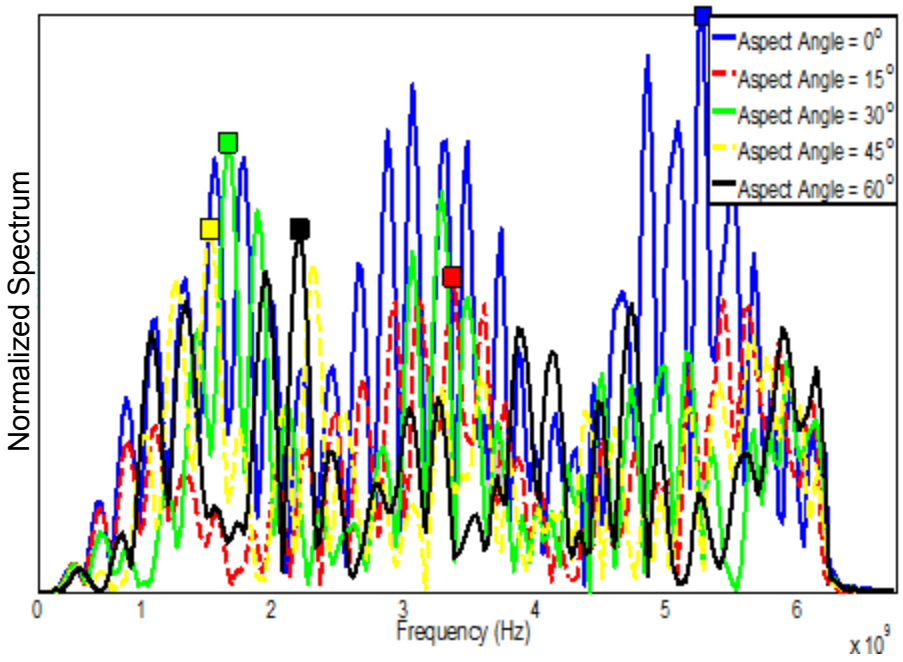


Figure 3.6 Table (target) transfer function for different aspect angles

The matched illumination scheme places signal energy that will have the best transmission response through the wall and scatter most effectively with the target under consideration. Figure 3.7 demonstrates how the matched illumination waveform places its energy in the optimal position given this impulse response (or equivalently transfer function) information used in the design process. It is clear that the optimal waveform contains energy at peaks in the wall transmission response and the target scattering response and varies greatly for wall's containing spectral differences due to their dielectric properties. Again, it should be remembered that the cases shown here assume white noise and no clutter. In the case of colored noise and clutter, the optimal waveform's spectral energy would be in the most optimal position with respect to wall transmission, target backscatter, noise spectral power, and clutter spectral power.

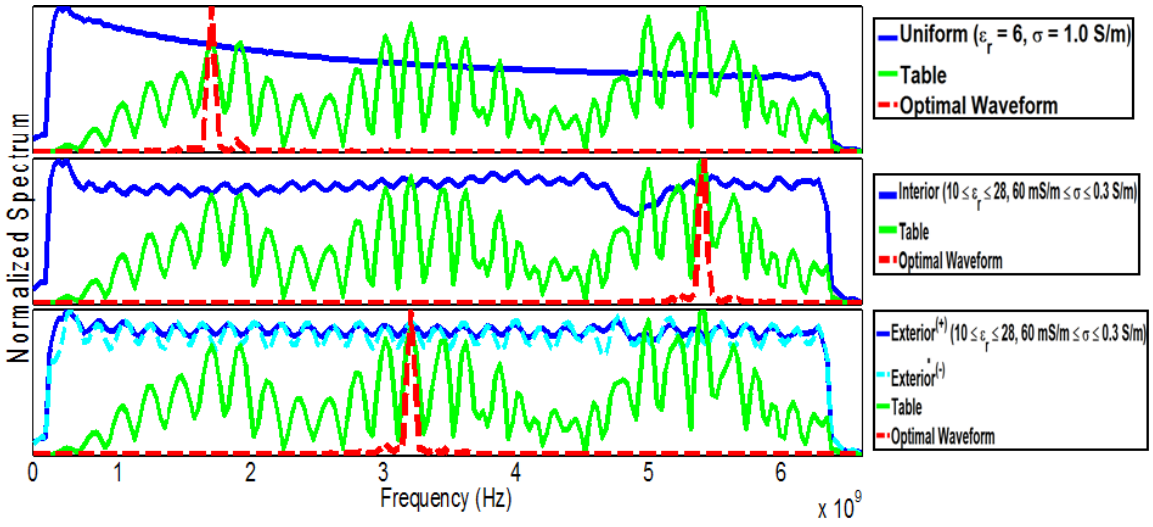


Figure 3.7 Transfer functions of particular wall model and table target and the resulting optimal waveform

With regards to only considering the conductivity changes (moisture will most significantly affect the conductivity of the material), Figures 3.8- 3.10 reveal that lower wall conductivities yield radome-like wall responses for all three profiles. In general, higher values of wall conductivities tend to smooth the wall responses over the considered frequency band for all three profiles, but still tend to favor lower frequencies for the interior and exterior profiles. For sufficiently high conductivities, surface reflections are enhanced at both wall/air interfaces for the uniform profile, but only at the outer wall/air interface for the exterior profile. The surface reflections are not affected at either wall/air interface for the interior profile.

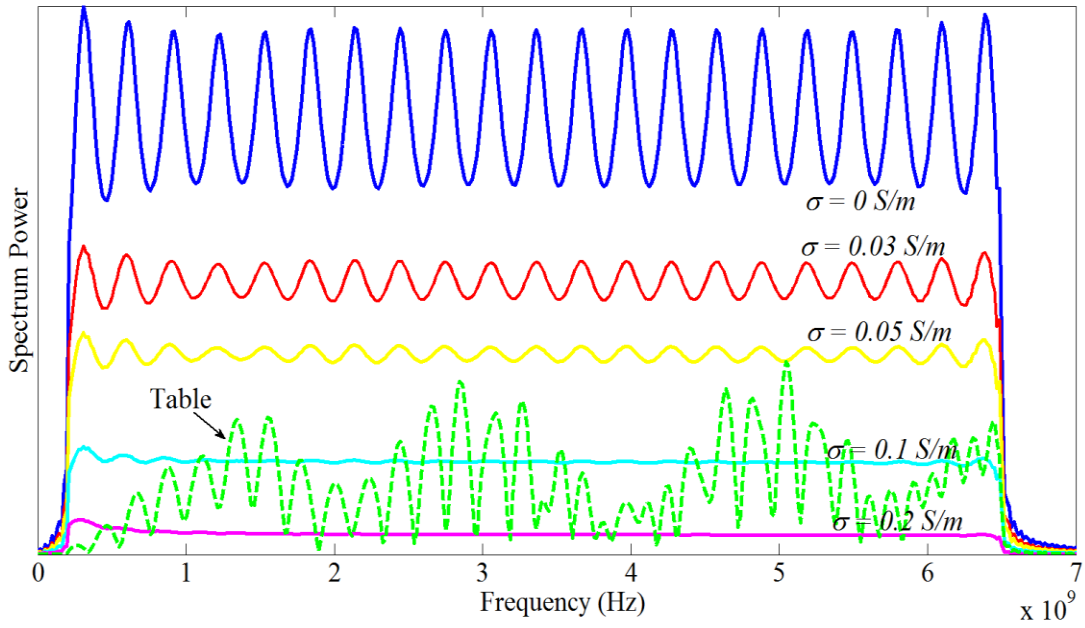


Figure 3.8 Wall and table transfer functions - uniform conductivity profile

Note: All wall models have relative permittivity value of $\varepsilon_r = 6$

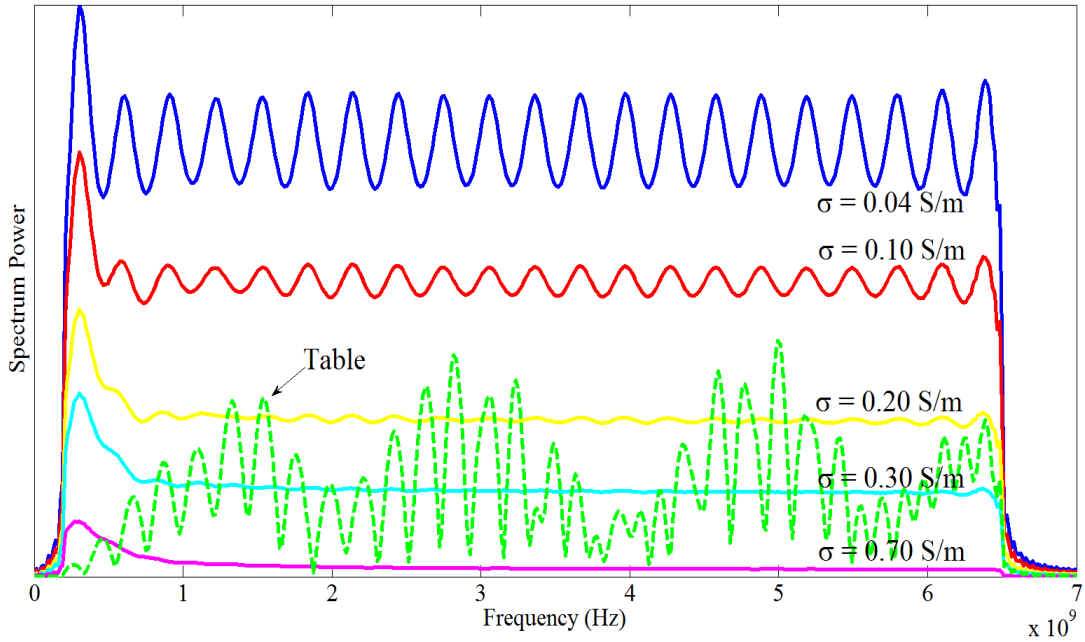


Figure 3.9 Wall and table transfer functions - interior conductivity profile

Note: All wall models have relative permittivity vale of $\varepsilon_r = 6$

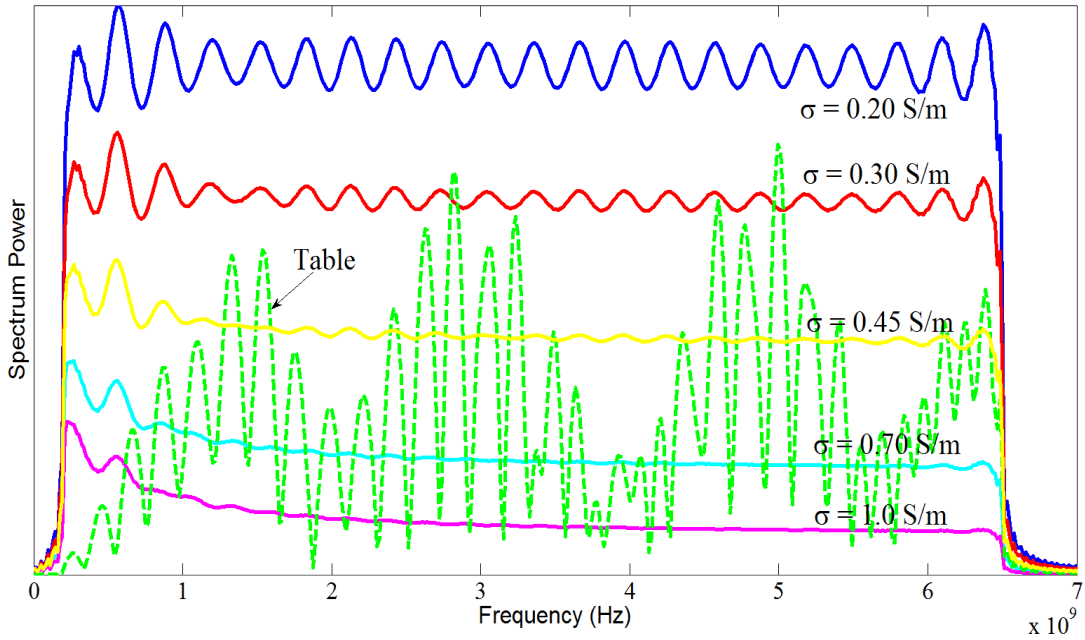


Figure 3.10 Wall and table transfer functions - exterior conductivity profile

Note: All wall models have relative permittivity value of $\varepsilon_r = 6$

The spectra of three representative matched illumination waveforms given uniform, interior, and exterior conductivity profiles of equal max conductivity and equal mean conductivity are shown in Figures 3.11 - 3.12, respectively. In general, the matched illumination optimization method places most of the signal energy where the combined wall transmission and target scattering responses are maximum. Clearly, the shape of the moisture profile (conductivity profile) significantly impacts the spectral location of the transmission waveform's energy as illustrated in Figures 3.11 – 3.12. Note that the matched illumination waveforms in Figure 3.12 are focused at a single lower frequency for the interior profile, a single upper frequency for the uniform profile, and distributed among three frequencies for the exterior profile. The three frequencies of interest represent the three highest peaks in the target response.

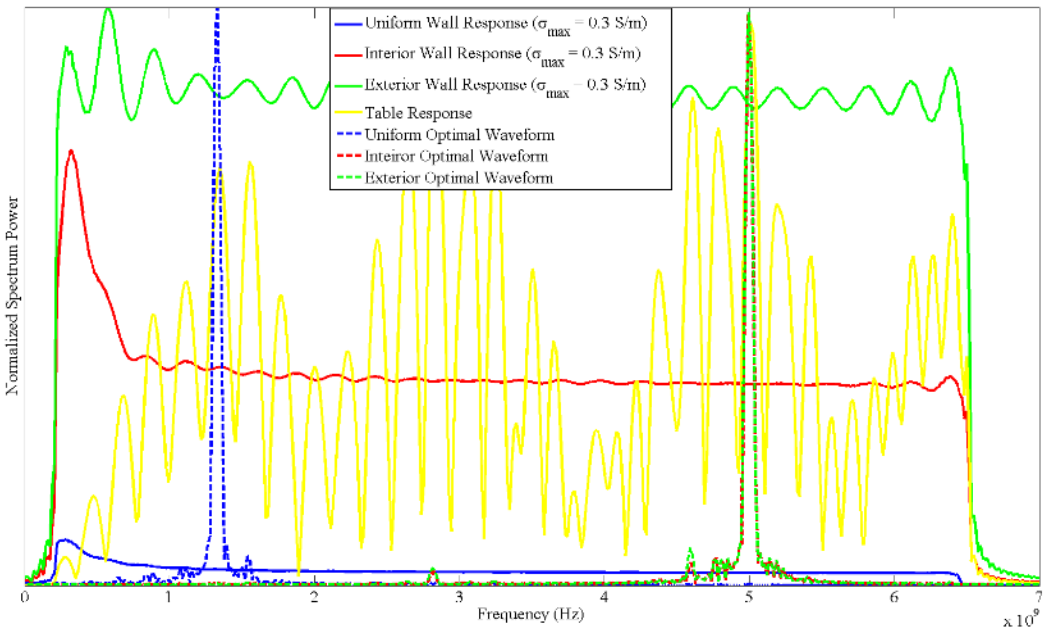


Figure 3.11 Matched illumination waveform spectra for different wall conductivity profiles of equal max conductivity

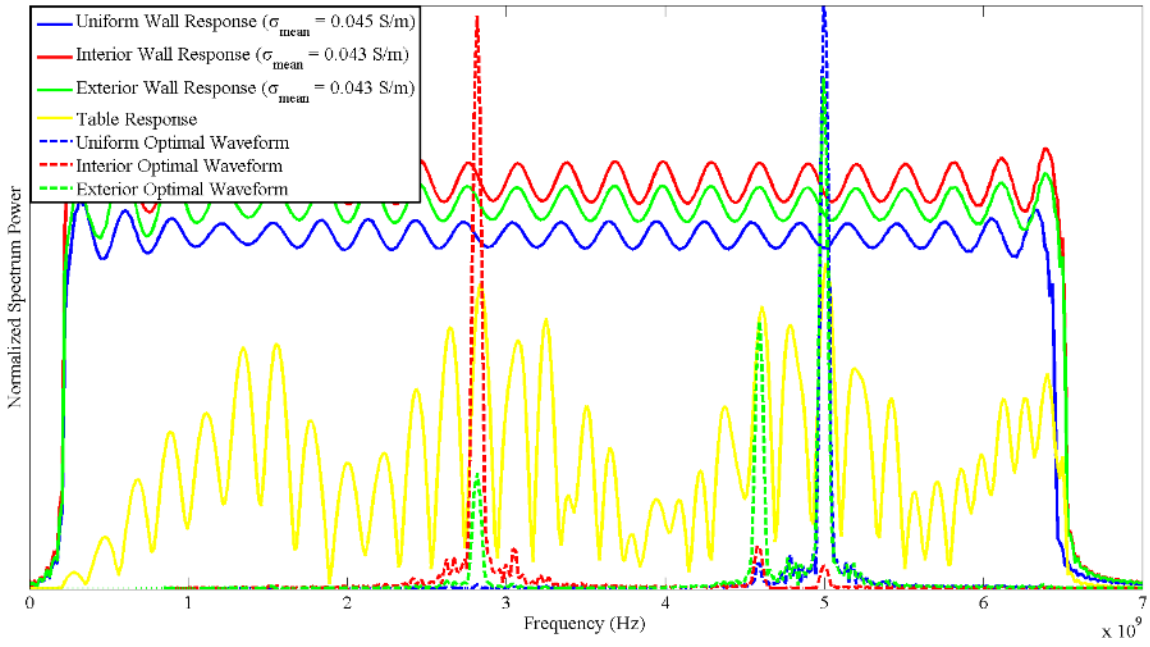


Figure 3.12 Matched illumination waveform spectra for different wall conductivity profiles of equal mean conductivity

### 3.2.2 SINR Comparison

Similar to Chapter 2, to compare the performance of different matched illumination waveforms, the input SNR is fixed to the matched filter in all cases. The noise variance is $\sigma^2 = P_{\max}/10^{\frac{SNR_{\text{in}}}{10}}$ where $P_{\max}$ is the highest power of the received signal, and $SNR_{\text{in}}$ is assumed to be 10 dB. The SINR corresponding to the transmitted optimal waveforms derived for a particular wall model and the table target at all aspect angles are computed and compared to the SINR of a transmitted chirp waveform of equal duration, equivalent energy, and covering frequencies from 0.9 GHz to 6.5 GHz. The chirp waveform serves as a good comparison because it is conventionally used in scenarios containing poor *a priori* information about the target scene as well as likely transmitting energy which will respond well to the environment due to its broadband characteristics.

The optimal waveform performed significantly better than the chirp signal, averaging greater than 15 dB SINR improvement for all wall models and aspect angles. The SINR computed for every aspect angle using the optimal waveform and chirp waveform for an interior wall moisture profile correlating to dielectric properties of $\varepsilon_r = 6, \sigma_{\max} = 0.3$ S/m and a table target is shown in Figure 3.13. It is evident from Figure 3.13 and Table 3.1 that the matched illumination waveform can provide significant enhancement to the radar system's SINR when modeled accurately. In Table 3.1, a subset of all simulation results is provided to illustrate the radar performance increase of optimal waveforms over chirp waveforms of equal duration and energy.

Also included in Table 3.1 is the SINR improvement over a chirp waveform attained for the three cylinder targets simulated and previously discussed in Chapter 2.

The chirp waveform is of equal duration and equivalent energy to the optimal waveforms and has cutoff frequencies of 1GHz and 4 GHz. Like the table target simulations, significant SINR improvement is attained for the cylinder targets when using the derived optimal waveforms. It is noted that the maximum SINR improvement corresponds to the optimal waveform derived from the full-wave response while the minimum SINR corresponds to the primary-wave response rather than differing aspect angle differences (for the cylinder simulations, aspect angle variation was not considered). Also, the SINR improvements seen for some of the cylinder targets is much lower than the improvements seen for the table target; however, a portion of this difference may be attributed to the chirp waveform used in the cylinder target simulations being more narrowband (1 - 4 GHz) than the chirp waveform (0.9 - 6.5 GHz) used for comparison of the table target simulations. From the SINR results of the cylinder targets, it can be inferred that the smaller, less efficient scatterers (smaller cylinders), benefit most from optimal waveform design rather than transmitting over a wide range of frequencies due to their narrow scattering response. As the scattering response of the target narrows, the transmission waveform's placement of spectral energy becomes ever more important to radar performance. Consequently, matched illumination waveform design can significantly benefit the radar performance of poor target scatterers.

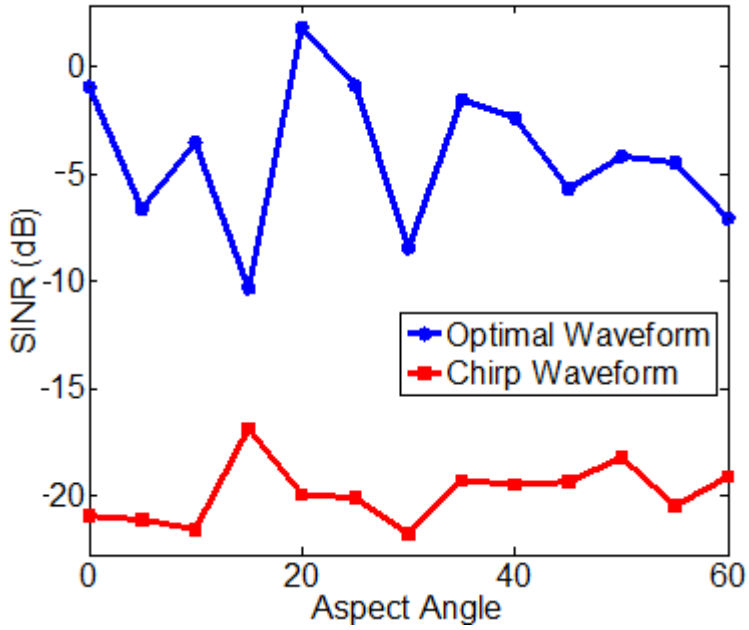


Figure 3.13 SINR comparison of transmitted optimal and chirp waveforms for an interior wall moisture profile corresponding to $\varepsilon_r = 6, \sigma_{\max} = 0.3$ S/m

Table 3.1 Representative subset of SINR improvement gained from transmitting matched illumination waveforms rather than chirp waveforms

| Profile | Target | $\varepsilon_r$ | $\sigma\ (S/m)$ | SINR Improvement ( dB ) | | |
|---|---|---|---|---|---|---|
| | | | | MAX | MIN | AVG |
| Uniform | Table | 6.0 | 0.0 | 20.26 | 12.46 | 15.22 |
| Uniform | Table | 6.0 | 1.0 | 23.19 | 9.82 | 16.73 |
| Interior | Table | 4.00 - 12.86 | 0.05 - 1.00 | 22.98 | 12.36 | 16.74 |
| Interior | Table | 10.0 - 28.00 | 0.06 - 0.30 | 22.87 | 11.27 | 15.74 |
| Exterior | Table | 4.00 - 12.86 | 0.05 - 1.00 | 21.95 | 12.10 | 16.34 |
| Exterior | Table | 10.0 - 28.00 | 0.06 -0.30 | 19.62 | 11.83 | 15.65 |
| Uniform | Cylinder (52 mm) | 6.0 | 0.0 | 28.19 | 27.18 | 27.72 |
| Uniform | Cylinder (114 mm) | 6.0 | 0.0 | 15.31 | 12.52 | 14.96 |
| Uniform | Cylinder (230 mm) | 6.0 | 0.0 | 6.101 | 3.722 | 5.389 |
| Uniform | Cylinder (52 mm) | 6.0 | 0.1 | 24.53 | 23.77 | 24.34 |
| Uniform | Cylinder (114 mm) | 6.0 | 0.1 | 13.92 | 9.988 | 12.49 |
| Uniform | Cylinder (230 mm) | 6.0 | 0.1 | 4.663 | 3.215 | 4.145 |

An example illustrating the need for accurate wall models is presented for a table target located behind a lossless interior profile wall with relative permittivity of $4.0 \leq \varepsilon_r \leq 12.86$. For the aforementioned wall/target scenario, the SINR was computed using both an optimal waveform derived from the actual wall/target scenario and an optimal waveform derived for a lossless uniform profile wall with relative permittivity of $\varepsilon_r = 6.0$ for all aspect angles. The resulting SINR per aspect angle is shown in Figure 3.14 along with the transfer functions of the optimal waveforms, table, and walls considered in the comparison for an aspect angle of zero shown in Figure 3.15. At an aspect angle of zero degrees ($\theta = 180°$, $\phi = 0°$), the SINR resulting from transmitting the interior optimal waveform for the interior wall simulation is over 10 dB higher than transmitting the uniform optimal waveform for the interior wall simulation, and it is clear that this occurs from the uniform optimal waveform placing its energy at a null spectral location of the interior wall's transfer function located around 3.2 GHz. Thus, the waveform doesn't propagate efficiently through the interior wall. Hence, having an accurate wall model which includes its proper material properties is vital part of TWR when utilizing matched illumination waveform design.

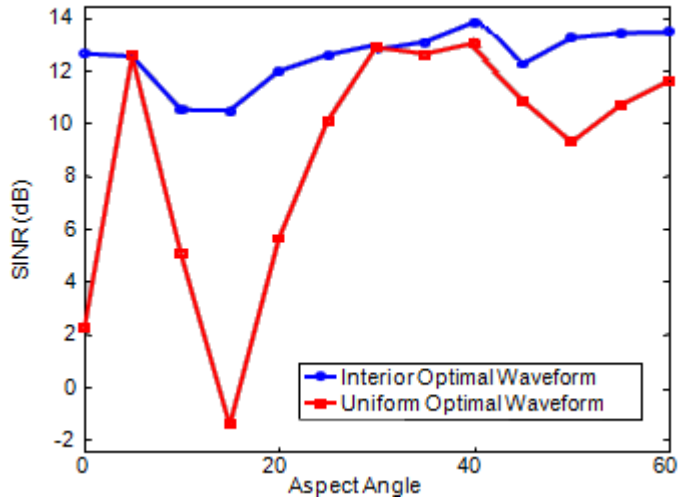


Figure 3.14 Resulting SINR per aspect angle when transmitting either an interior ($4.0 \leq \varepsilon_r \leq 12.86$) or uniform ($\varepsilon_r = 6.0$) optimal waveform through the interior wall model with a table located behind it

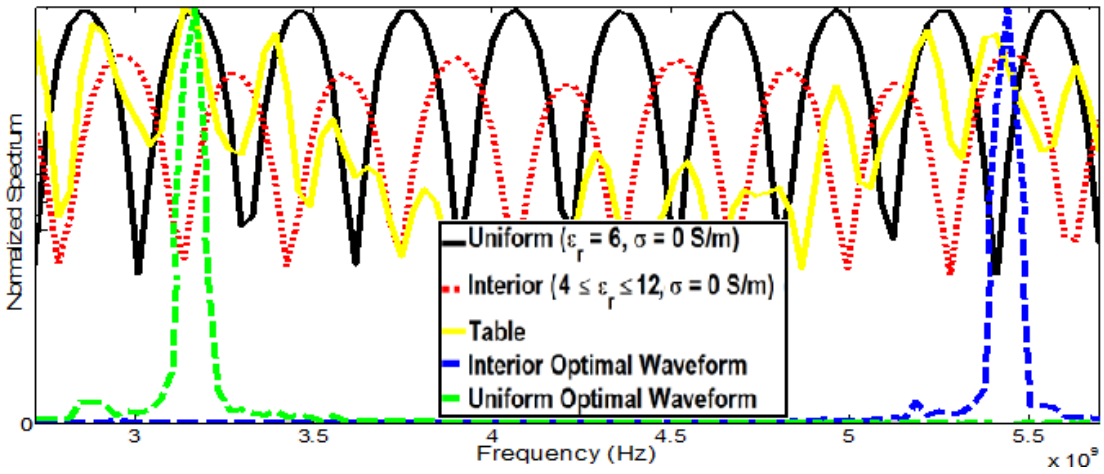


Figure 3.15 Transfer functions at an aspect angle of zero degrees of interior wall model, uniform wall model, and table along with resulting optimal waveforms

## 3.3 Chapter Summary and Conclusions

The matched illumination waveform results shown in Figures 3.7 and 3.11 - 3.12 for the different dielectric property profiles demonstrate that the shape of the wall moisture profile can dramatically impact the spectral composition of the resulting optimal waveform. The SINR enhancements shown through simulation provide good reason to utilize matched illumination waveforms for TWR. Through numerous simulations, it was shown that in general, the wall transmission response sees a fundamental transition in its spectral characteristics at a conductivity threshold between $0.1 \leq \sigma \leq 1.0$ S/m. At conductivities above the threshold, the spectral response of the wall flattens out so that the target scattering response is the main driving force in the design of the optimal waveform.

Meanwhile, it is clear that the resulting optimal transmission waveform's performance perilously relies on the *a priori* information of the model used in derivation of the impulse response information of the radar scene. Furthermore, little information is available on realistic moisture conductivity profiles for commonly used walls and specifically adobe walls. In order to validate the radar performance of the computed matched illumination waveforms as well as provide realistic wall material parameters for commonly encountered walls, the wall's material profile through moisture and dielectric measurement must be obtained and is the topic of discussion in Chapter 4.

# CHAPTER IV

# MOISTURE PROFILE AND DIELECTRIC PROPERTIES FOR ADOBE WALL

As previously discussed, TWR applications may require advanced modeling of the radar system to adequately address wall effects impacting the radar signal waveform. These propagation effects degrade the imaging results and must be accurately modeled to achieve suitable TWR imaging and target detection. Consequently, it is necessary to know the dielectric properties of the wall under consideration. In this study, a coaxial probe measurement technique was used to investigate the dielectric properties of an adobe wall structure in the microwave region of 500 MHz to 7 GHz. Additionally, it is shown that the dielectric properties are moisture-dependent and the moisture profile of the adobe wall is obtained for more accurate and meaningful modeling.

## 4.1 Introduction

Typically, model-based reasoning must be used to design radar systems which allow imaging or detection of objects located behind a wall. In order to properly design a radar system for a TWR scenario, the wall must be accurately accounted for due to the ability of the wall to significantly impact the radar performance. For example, it was shown in [1] and briefly discussed previously that two-way wall attenuation differences of more than 50 dB are likely for through-wall radar performance. Unfortunately, previous research regarding typical dielectric properties of walls is limited and especially

lacking with regards to changes in the dielectric properties as a function of frequency and moisture content [51,59-62,76-78,81-82,92-93]. The moisture content of the wall material enhances the impact of the wall on radar waveforms because it increases the electric conductivity of the material.

The permittivity $\varepsilon$ of a material is defined as

$$\varepsilon = \varepsilon' + j\varepsilon'' \tag{4.1}$$

where the real part $\varepsilon'$ is the absolute permittivity of the material relative to that of free space $\varepsilon_0$, or equivalently $\varepsilon' = \varepsilon_r \varepsilon_0$. The imaginary part $\varepsilon''$ is its dielectric loss factor (also relative to that of free space). Electrical conductivity is a commonly used parameter in modeling materials and is related to dielectric loss factor as

$$\varepsilon'' = \frac{j\sigma}{\omega \varepsilon_0} \tag{4.2}$$

where $\sigma$ is electrical conductivity and $\omega$ is the angular frequency.

The purpose of this chapter is to investigate the microwave dielectric properties, i.e., $\varepsilon$, of a commonly encountered wall structure, adobe, in the frequency range of 500 MHz to 7 GHz. The frequency range studied is chosen to comfortably accommodate the frequencies (1GHz – 4 GHz) which have shown to give the most desirable tradeoff between signal attenuation, scene resolution, and antenna size for TWR [1]. It has been shown in [75, 87-88] and discussed in Chapters 2 and 3 that the moisture profile of the wall structure has a significant impact on the waveform design of TWR using matched illumination theory. The work presented in this chapter specifically addresses the moisture profile of a wall and its correlating dielectric properties to enhance modeling of walls in model-based TWR.

## 4.2 Experimental Procedure

To obtain dielectric data and correlate it to specific levels of moisture content, five adobe wall samples are used. The samples are obtained by extraction through cutting an adobe wall test article. That is, a large adobe wall will be decomposed into five smaller samples which will be used for dielectric property and moisture evaluation and validation.

The adobe wall test article is composed of compressed earthen blocks provided by the Engineer Research and Development Center (ERDC), Geotechnical and Structures Laboratory, Concrete Materials Branch. The compressed earthen blocks, here after referred to as adobe bricks, were identified by ERDC as the best candidate material based on a combination of local availability, sand to clay ratio, homogeneity, and consistency. The bricks are formed from a characterized soil/clay mixture and pressed into blocks using an AECT 3500 Series Compressed Earth Block Machine [102]. The bricks are then assembled into walls using a mortar formed from the same sand and soil mixture with the addition of water in a one to three to one ratio by mass, respectively. The mortar is spread between the joints of the bricks, and the bricks are allowed to settle within the mortar and solidify. The adobe walls provided for the experiments are shown in Figure 4.1 below.

The dielectric data reported in this study were generated from two experiments. The first experiment is dielectric and moisture measurement performed for five adobe wall samples of similar size. The samples are subjected to a constant relative humidity level until they reach a constant weight which is equal to their moisture content at that respective relative humidity level. Then, each sample's dielectric properties are

measured at five spatially different locations on the individual adobe sample using a dielectric probe system described in section 4.2.2 below. The five measurements are then averaged and represent the dielectric data for that particular adobe sample. The results shown later in this chapter are the mean of the five averaged adobe wall samples data for a given moisture level. Thus, at each moisture level shown, the data is representative of 25 distinct dielectric measurements. The five adobe sample's dimensions and dried mass is given in Table 4.1. Note, due to the brittleness of the adobe brick samples, the dimensions are not completely square and represent the maximum measurement for a given dimension.

Table 4.1 Adobe sample dimensions and dried mass used in Experiment 1

| Sample # | Length (cm) | Width (cm) | Thickness (cm) | Mass Dried (g) |
|---|---|---|---|---|
| 1 | 2.50 | 3.30 | 2.20 | 16.23 |
| 2 | 2.85 | 2.60 | 3.40 | 24.63 |
| 3 | 2.85 | 4.10 | 3.40 | 39.93 |
| 4 | 3.70 | 4.50 | 2.10 | 34.31 |
| 5 | 3.45 | 5.10 | 2.00 | 35.91 |

The second experiment is performed for an adobe brick extracted from an adobe test wall article that is subjected to relative humidity levels encountered at room temperature inside the Mississippi State University anechoic chamber. The adobe brick, originally 35.6 × 17.8 × 10.2 cm is then cut in half using a MK-PX3 dry cutting masonry saw and dielectric properties are measured along a determined path (in the direction of waveform propagation, along the 17.8 cm dimension) to measure any dielectric profile arising from a moisture distribution within the brick. The first measurement is taken at

0.1 cm from the brick's edge and subsequent measurements are made 2.2 cm from the previous measurement. Then, the moisture is measured at the given dielectric measurement positions by cutting sub-samples from the brick. The sub-samples are positioned around the dielectric probe measurement. That is, the sub-samples' center is the location of the dielectric probe. Measurements follow the diagram shown in Figure 4.1 below.

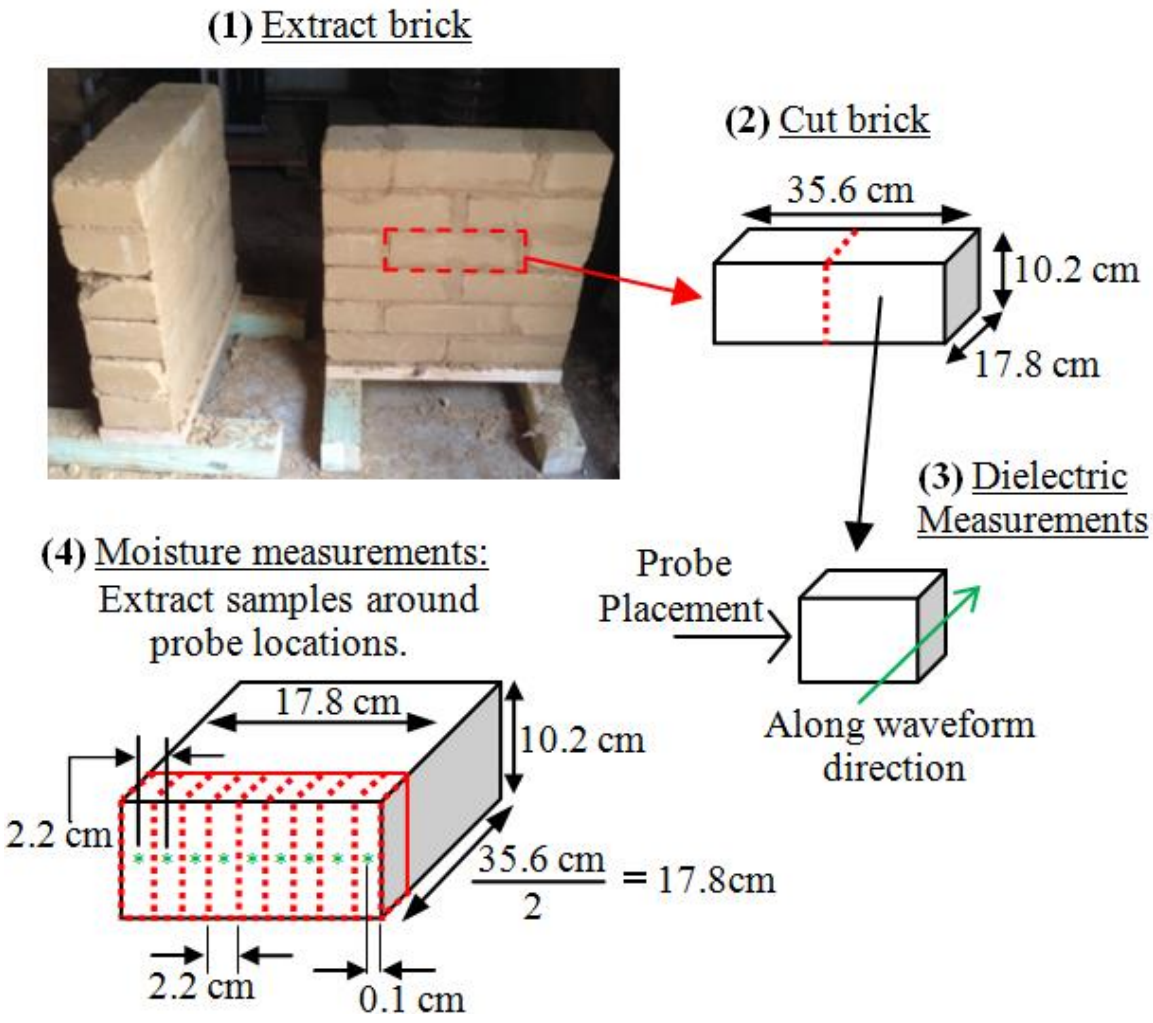


Figure 4.1 Adobe wall test articles and experiment 2 measurement procedure

### 4.2.1 Dielectric Probe Measurement Technique

The permittivity data reported in this work is based on measurements of the complex reflection coefficient of a coaxial probe terminated on the material under test (adobe sample). The dielectric probe system used for this work is implemented with the Agilent 85070E Dielectric Probe Kit and network analyzer consisting of open-ended coaxial probes, application software, calibration standards, cables, and adapters [95]. The network analyzer sweeps and measures the material's response to microwave energy which the probe transmits into the material under test. The software then uses the reflected signal ($S_{11}$) to calculate the complex permittivity $\varepsilon$.

Three different types of dielectric probes from the probe kit were tested and the probe exhibiting the least measurement variability was used. After preliminary testing, it was found that the Slim Form Probe, Option 030, yielded the most consistent measurements and was used for the data reported in this work. The probe has a frequency range of 500 MHz to 50 GHz and is an open-ended coaxial probe as shown in Figure 4.2.

The dielectric measurements are based on a "semi-infinite" material size constraint that, for accurate measured results, a sample must be at least equal to the probe diameter. For the Slim Form Probe, this condition is satisfied if the sample thickness is greater than 5 mm. The sample is also assumed to be non-magnetic, isotropic, and homogeneous. The surface of the sample in contact with the probe must be very flat and smooth to ensure gap free contact. Samples in this study were cut with the dry cutting masonry saw to obtain a nearly flat surface.

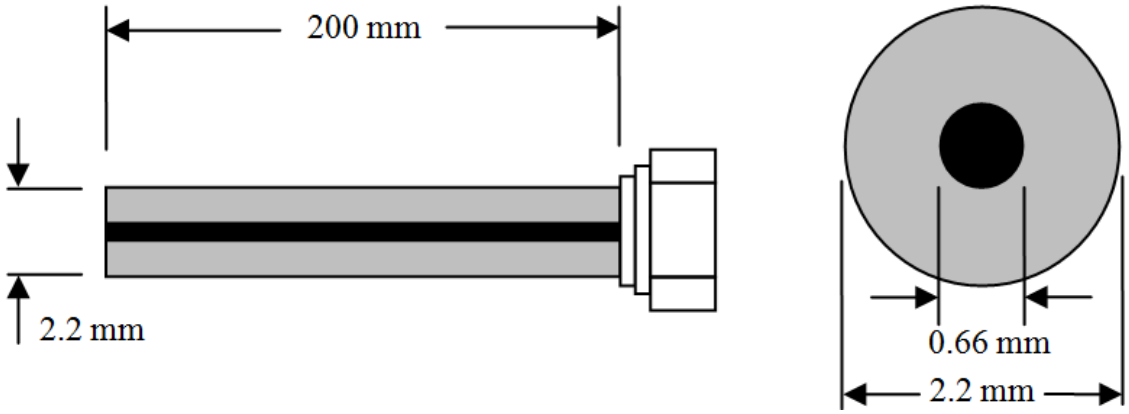


Figure 4.2 Dimensions of the Slim Form Probe used in measurements

All measurements were taken linearly over the frequency range of 500 MHz to 7 GHz in steps of 1 MHz. Prior to each measurement trial, the dielectric probe was calibrated to three known standards which include air, a short circuit, and water. Additionally, to ensure measurement accuracy, a simple mounting bracket stand was used to stabilize the probe in contact with the sample through the measurement.

### 4.2.2 Moisture Profile Measurement Technique

To measure moisture content of a material, gravimetric analysis is often used and has been shown to be one of the most accurate methods for moisture content measurement of solids [77, 94]. This method is based on applying dry-weighing to a material and the moisture content

$$\Psi = \frac{m_w}{m_d + m_w} \times 100\% \tag{4.3}$$

is calculated by weighing the sample (wet), drying the sample, and then weighing the sample (dry) again. In (4.3), $m_w$ is the mass of the sample containing water and $m_d$ is

the mass of the dried sample. Generally, a sample is dried in an oven at 103 ℃ - 110 ℃ for an hour and allowed to cool to room temperature in a desiccator. It is then heated again for 30 minutes, allowed to cool, and weighed a second time. The procedure is then repeated until successive weighings agree to within 0.3 mg [94].

Correlating the dielectric properties to specific moisture content levels of the adobe samples is accomplished with the use of an environmental chamber. To obtain uniform moisture content throughout the sample, the adobe samples are first oven dried to a constant weight and then placed inside an ETS Model 5503 Controlled Environmental Chamber set to a constant relative humidity until the sample reaches a constant weight for the given humidity level. This allows both maximum moisture absorption within the material sample at a given humidity level in addition to providing a uniform moisture profile throughout the sample which ensures the material assumption of the dielectric measurement procedure that assumes a homogeneous material.

The uniform absorption (homogeneous profile) assumption made for the adobe samples subject to the environmental chamber was confirmed in preliminary experiments and is discussed in further detail in Chapter 4.3.1. The preliminary work used gravimetric analysis of different sections of an adobe sample held in the environmental chamber at varying humidity levels and times. The moisture content measured for the subsections of the original sample all contained moisture content within $\pm 0.257\%$ of the entire sample which confirms uniform moisture content throughout the original sample.

## 4.3 Dielectric and Moisture Profile Measurement Results

The permittivity and correlating moisture profiles were measured for an adobe wall in experiment 1 at varying moisture content levels. Then, in experiment 2, the

moisture profile of an adobe wall in a static environment was measured along with its permittivity in order to both validate the measurements of experiment 1 as well as provide a realistic moisture/dielectric profile that adobe walls exhibit in normal conditions. This information is crucial to model-based reasoning and TWR, especially when designing transmitting waveforms through matched illumination theory.

### 4.3.1 Uniform Moisture Throughout Sample

To ensure uniform moisture content throughout the adobe samples used in experiment 1, preliminary testing was conducted on an adobe sample of comparable size to the samples used in experiment 1. This preliminary testing also produced saturation times required to reach moisture uniformity for the sample.

First, an adobe brick was cut to extract a sample having maximum dimensions of $2.6 \times 4.1 \times 3.6$ cm and weighing 37.84 g after drying to a constant weight (dry mass). The sample was then placed in the environmental chamber and exposed to a constant relative humidity level. Over time, the sample was repeatedly weighed until a constant weight was attained. Thus, it is reasonable to assume that the sample is fully saturated and has achieved homogeneous or uniform moisture content. Then, the relative humidity level is increased and the sample is again repeatedly weighed over time until a constant weight is achieved. After this procedure is repeated several times and the sample is exposed to several relative humidity levels, the sample, again at a constant weight for a given humidity level, is cut into five sections and each subsection is dried to a constant weight. If the weight of each subsection is equal, then it is reasonable to assume that the original sample contained a homogeneous moisture profile.

The preliminary testing procedure described above yielded results which confirm that after an adobe sample is exposed to a relative humidity level for a satisfactory period of time, the sample will contain a homogeneous moisture profile. The details of the preliminary testing are shown in Tables 4.2 - 4.3. The time required (in minutes) to reach a constant weight ($m_{brick}$) is provided in Table 4.2 where the relative humidity (RH) level is provided with the corresponding moisture level ($\Psi$) of the adobe brick sample. Furthermore, Table 4.3 provides the gravimetric analysis results of the five subsections ($m_{brick}^{1-5}$) cut from the original adobe sample used in the prior measurements. The five subsections of the original sample should be equal to the moisture content measured in the original sample. The percent difference between the final moisture content of the original sample ( $\Psi_{brick}(RH = 97.9\%)$ ) and the moisture content of each brick subsection sample ($\Psi_{brick}^{1-5}$) is provided in Table 4.3 as $\Delta\%$ which follows $\Delta\% = |\Psi_{brick} - \Psi_{brick}^{1-5}|$ .

Table 4.2 Preliminary testing to ensure complete saturation of adobe sample

| RH (%) | Time (min): | $m_{brick}$( g ) | Ψ(%) |
|---|---|---|---|
| 75.9 | 0 | 37.84 | 0.000 |
| | 870 | 39.09 | 3.198 |
| | 910 | 39.10 | 3.223 |
| | 930 | 39.12 | 3.272 |
| | 1120 | 39.12 | 3.272 |
| | 1142 | 39.12 | 3.272 |
| 80.9 | 0 | 39.12 | 3.272 |
| | 210 | 39.21 | 3.494 |
| | 245 | 39.22 | 3.519 |
| | 270 | 39.20 | 3.469 |
| | 980 | 39.28 | 3.665 |
| | 1115 | 39.28 | 3.665 |
| 85.9 | 0 | 39.24 | 3.568 |
| | 40 | 39.28 | 3.666 |
| | 75 | 39.29 | 3.691 |
| | 345 | 39.37 | 3.886 |
| | 485 | 39.37 | 3.886 |
| 90.9 | 0 | 39.37 | 3.886 |
| | 720 | 39.58 | 4.396 |
| 95.9 | 0 | 39.54 | 4.299 |
| | 270 | 39.74 | 4.781 |
| | 585 | 39.78 | 4.877 |
| 97.9 | 0 | 39.73 | 4.757 |
| | 910 | 40.12 | 5.683 |
| | 920 | 40.10 | 5.636 |
| | 1120 | 40.12 | 5.683 |

Table 4.3 Preliminary testing to ensure uniform saturation of adobe sample

| | $m_w$ ( g ) | $m_d$ ( g ) | Ψ (%) | Δ% |
|---|---|---|---|---|
| $m_{brick}^1$ | 9.34 | 8.79 | 5.89 | 0.206 |
| $m_{brick}^2$ | 5.46 | 5.14 | 5.86 | 0.178 |
| $m_{brick}^3$ | 9.26 | 8.71 | 5.94 | 0.257 |
| $m_{brick}^4$ | 6.03 | 5.68 | 5.80 | 0.121 |
| $m_{brick}^5$ | 2.60 | 2.45 | 5.77 | 0.086 |

It is clear that after approximately 15 hours and 30 minutes, it is reasonable to assume that the adobe sample considered reaches full moisture saturation at the respective relative humidity level. The time to reach that saturation point is confirmed for all relative humidity levels used in the preliminary testing, but the time may actually be much shorter. Saturating the sample from its dry mass to a moisture content of 3.272% would intuitively take longer than saturating the sample from 3.272% to 3.665%, and the 15 hours and 30 minutes time frame corresponds to the sample gaining 3.272% moisture. A more thorough study of the saturation times would be required to place a definitive number on the time required to uniformly increase the moisture content of an adobe sample; however, this is beyond the scope of the work presented. Rather, confidence in obtaining a homogeneous moisture profile after some determined time threshold was desired and the testing was undertaken to provide that.

The percent moisture within each subsection of the original adobe brick sample was within $\pm 0.257\%$ of the final moisture content of the adobe sample which is nearly equal and a sufficiently small enough error to assume that the moisture is uniformly distributed within the adobe sample. All adobe samples measured throughout experiment 1 were exposed to a constant relative humidity level for over 24 hours which is greater

than the threshold limit observed in preliminary testing. In doing so, the dielectric probe assumptions of the material being measured having a homogeneous composition and containing uniform moisture saturation is met.

### 4.3.2 Dielectric Properties with Correlating Moisture Content

The first experiment, previously referred to as experiment 1, which measured the dielectric properties of adobe brick samples at varied levels of moisture content, showed good agreement in permittivity being impacted by the amount of moisture present within the adobe sample. Among the five samples and 25 combined measurements at each relative humidity level, the measured value of relative permittivity, $\varepsilon_r$, ranged between 1.654 and 6.273. Additionally, the measured value of electric conductivity, $\sigma$, ranged between 0 and 0.2389 S/m for all measurements. The ranges of relative permittivity and conductivity for a given moisture content level are presented in horizontal bar-chart format in Figures 4.3 - 4.4. The square and diamond markers on each line represent the mean of the measured values at 500 MHz and 7 GHz, respectively. It is noted that the change in relative permittivity from 500 MHz to 7 GHz is relatively small whereas the change in electrical conductivity is significant due to the effects that moisture has on dielectric properties and its major effect on the conductivity of materials.

As seen in Figures 4.3 - 4.4, the variation of measurements can be significant, and this can be attributed to error in repeatability of the dielectric probe measurements as well as the different probe position on the sample which likely contains non-uniform densities throughout the sample due to the inherent composition of the adobe bricks. However, after further analysis, it was found that the adobe bricks maintained measurements within

$\pm 5\%$ which is in agreement with Agilent's typical probe accuracy of $\varepsilon' = \varepsilon' \pm 0.05\,|\varepsilon|$ and $\varepsilon'' = \varepsilon'' \pm |\varepsilon|$ found in [95].

It should be noted that the electric conductivity values measured for the brick samples at 0% moisture content (completely dried) are not displayed in the figures because the values were inconsistent and sometimes contained negative values of the dielectric loss factor, $\varepsilon''$. This error may be due to the material being too low lossy as it is recommended that the minimum recommended loss tangent be greater than 0.05 for the measurement tools utilized in this study [95].

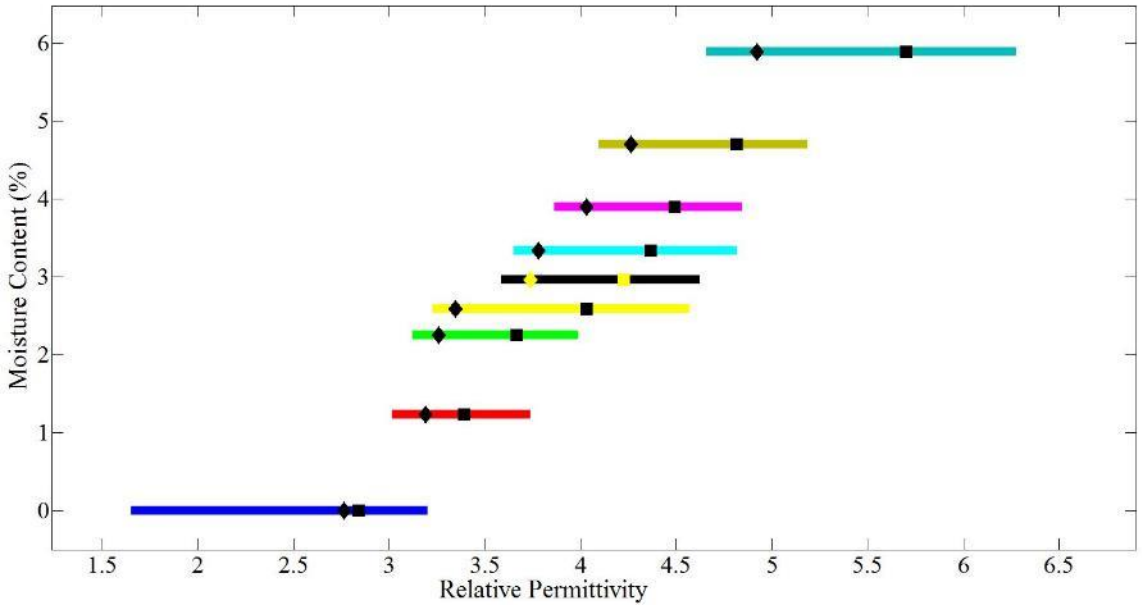


Figure 4.3 Relative permittivity ($\varepsilon_r$) measured at given moisture content levels

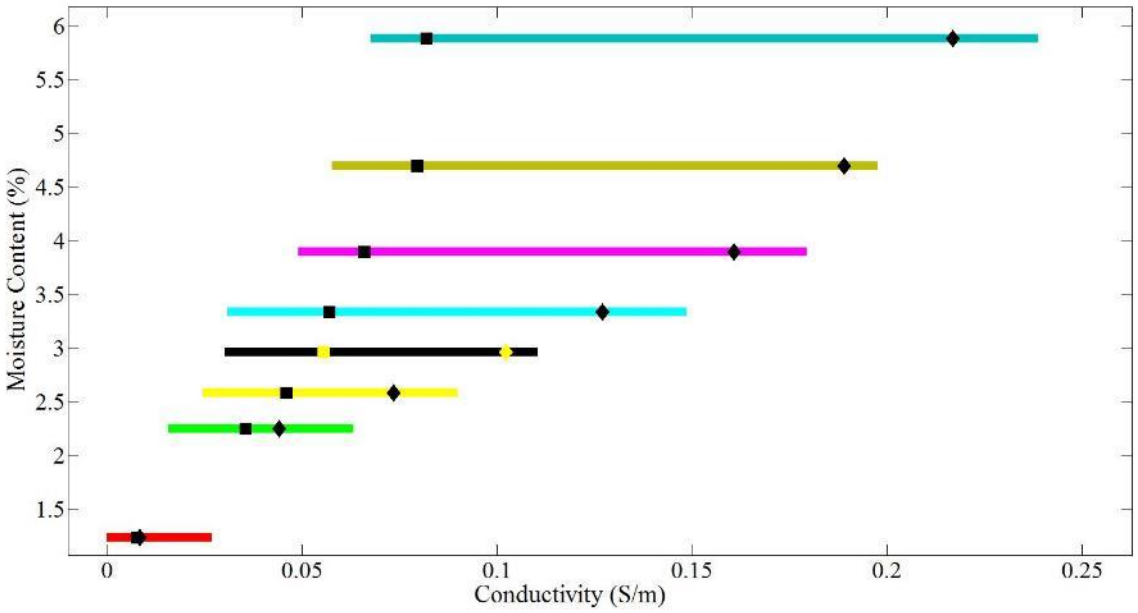


Figure 4.4 Electrical conductivity ($\sigma$) measured at given moisture content levels

To combat outliers within the measured data and more clearly bring out frequency dependencies, least-squares linear regression approximations are applied to the means of the dielectric measurements. The regression models of relative permittivity and electrical conductivity are shown in Figures 4.5 - 4.6 below with uncertainty margins which correspond to the maximum and minimum measured value at the respective frequency of all measured data. All measurements and their corresponding regression models are in good agreement with one another in terms of their dielectric property value location with regards to change in moisture content. That is, as the moisture content of the adobe samples increase, the corresponding relative permittivity values increase. Similarly, the electrical conductivity values increase in accordance to an increase in moisture content.

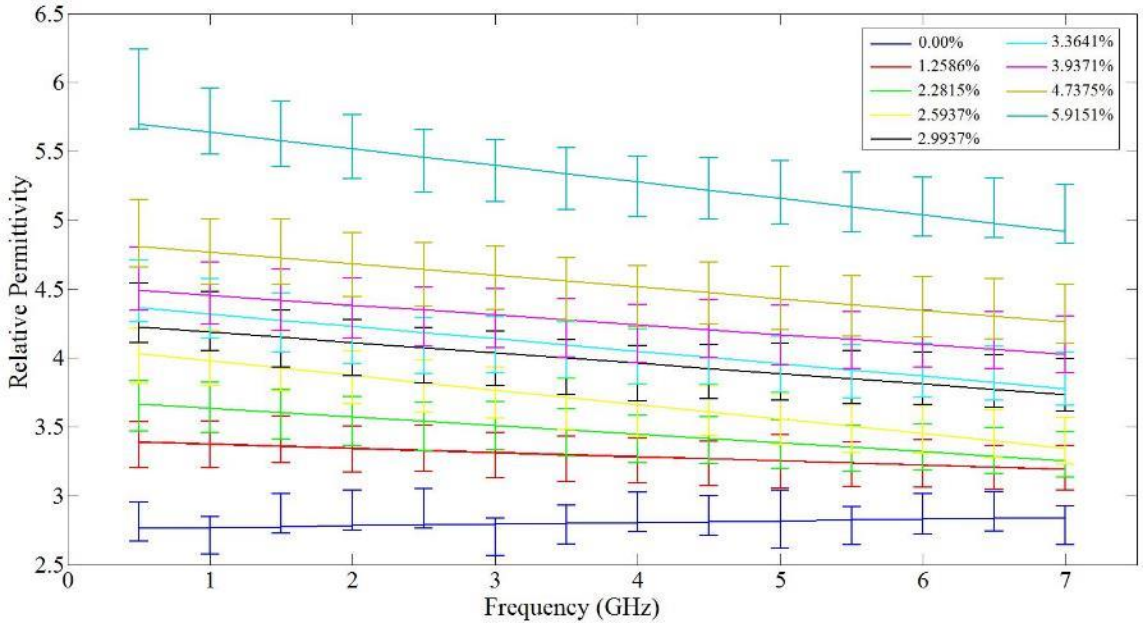


Figure 4.5 Linear regression model of relative permittivity measurements for each moisture content level considered

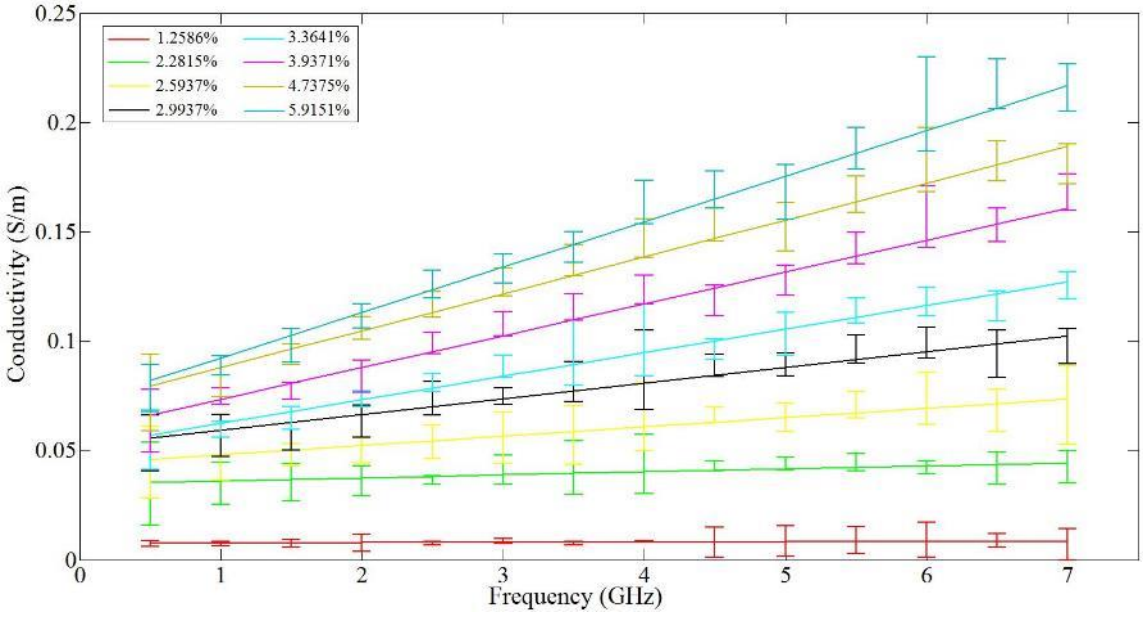


Figure 4.6 Linear regression model of electrical conductivity measurements for each moisture content level considered

For completeness of presenting results of experiment 1, Figure 4.7 provides the moisture content present within the measured brick samples after being subjected to the constant relative humidity level maintained in the environmental chamber. The moisture content appears to follow an exponential curve with regard to its increase given a particular relative humidity. This information may be useful for modeling adobe walls in particular environments and allow libraries of optimal radar parameters for different climatic conditions and events.

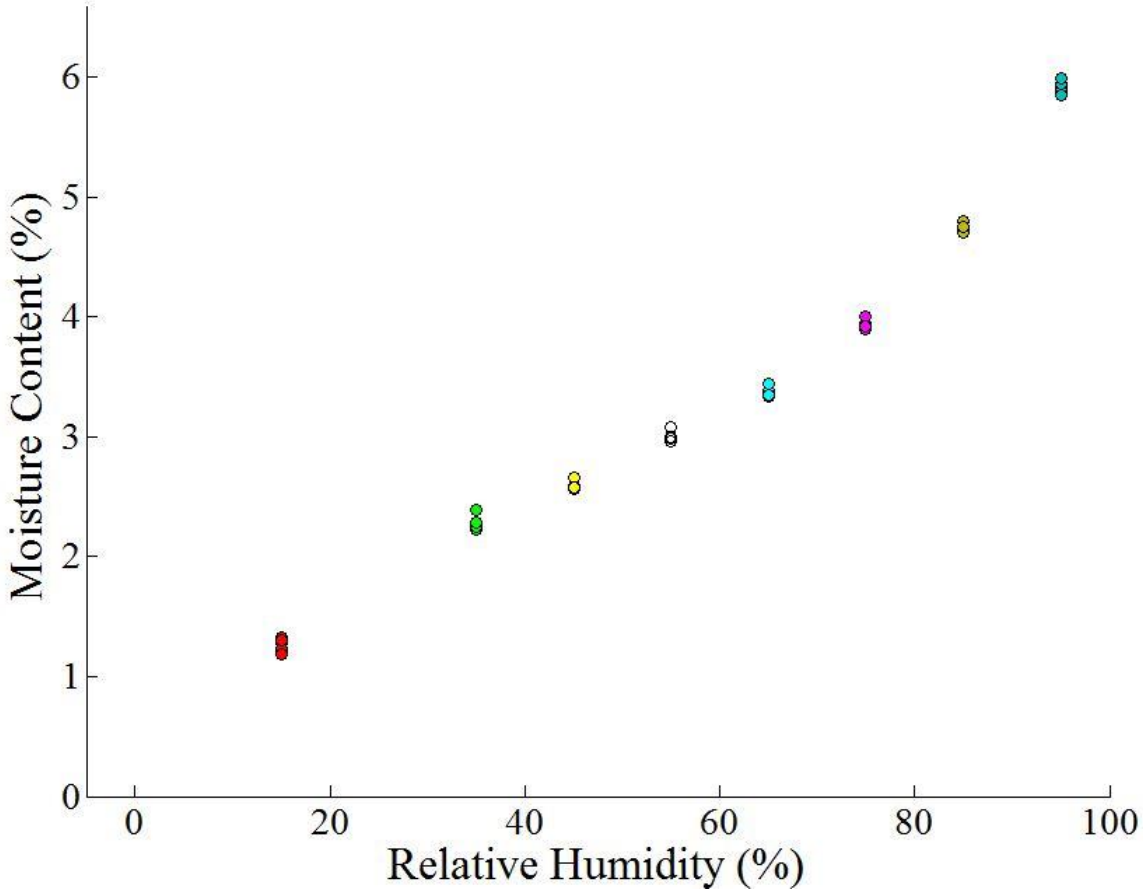


Figure 4.7 Moisture content of adobe samples for each relative humidity level

For validation and realization of an accurate, realistic moisture profile for an adobe wall at normal conditions, experiment 2 produced moisture and dielectric measurements of an adobe wall subjected to a relative humidity level experienced in an indoor facility. In this manner, the moisture profile of the wall will be measured for non-uniformity with regards to moisture content present along a particular dimension of the wall as described earlier in Figure 4.1.

### 4.3.3 Validation of Measurements and Proof of Moisture Profile

To confirm the data measured for the adobe samples as well as investigate accurate moisture profiles for adobe walls, the dielectric properties and moisture content was measured for an adobe brick along the typical radar waveform's path of propagation. The adobe brick was extracted from a complete adobe wall structure and follows the diagram in Figure 4.1. The resulting measured data of dielectric properties and moisture content for the adobe brick agree well with the results of the measured adobe samples from experiment 1.

In Figures 4.8 - 4.9, the relative permittivity and electrical conductivity for the brick is shown with regard to its measured position along the brick and compared with the data obtained for the brick samples in experiment 1. Results in Table 4.4 detail the moisture content present at the measured positions. Additionally, the relative permittivity and electrical conductivity measured at 500 MHz and 7 GHz are given to allow insight to be drawn into the measurements and how the moisture profile directly shapes the dielectric property profile of the adobe wall. The overall moisture profile of the brick along the measured path is shown in Figure 4.10. The data shown for Position 1 in Figures 4.8 - 4.10 as well as in Table 4.4 is the leftmost measurement located at 0.1 cm

from the extracted adobe brick's edge. This follows directly with the measurement procedure described earlier in Chapter 4.2 and illustrated in Figure 4.1 and Figure 4.10. Again, measurements progress along the brick in steps of 2.2 cm; thus, Position 2 is located 2.3 cm from the bricks edge, Position 3 is located at 4.5 cm from the brick's edge, and so on.

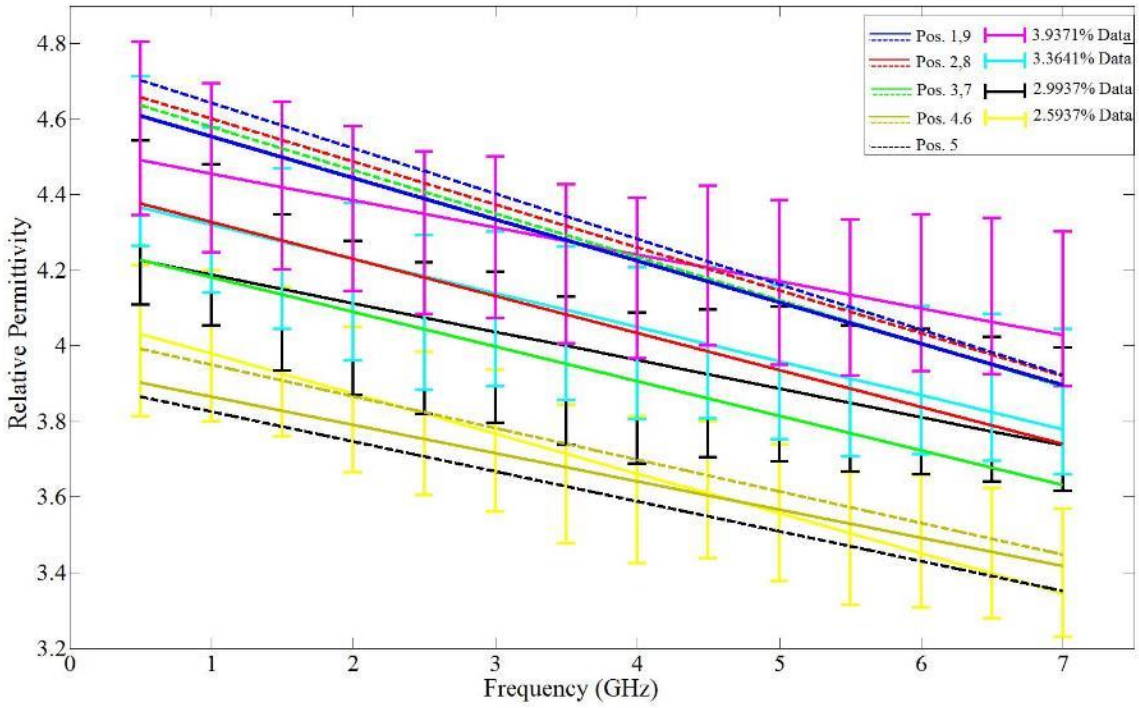


Figure 4.8 Linear regression model of relative permittivity measurements of adobe brick taken during experiment 2

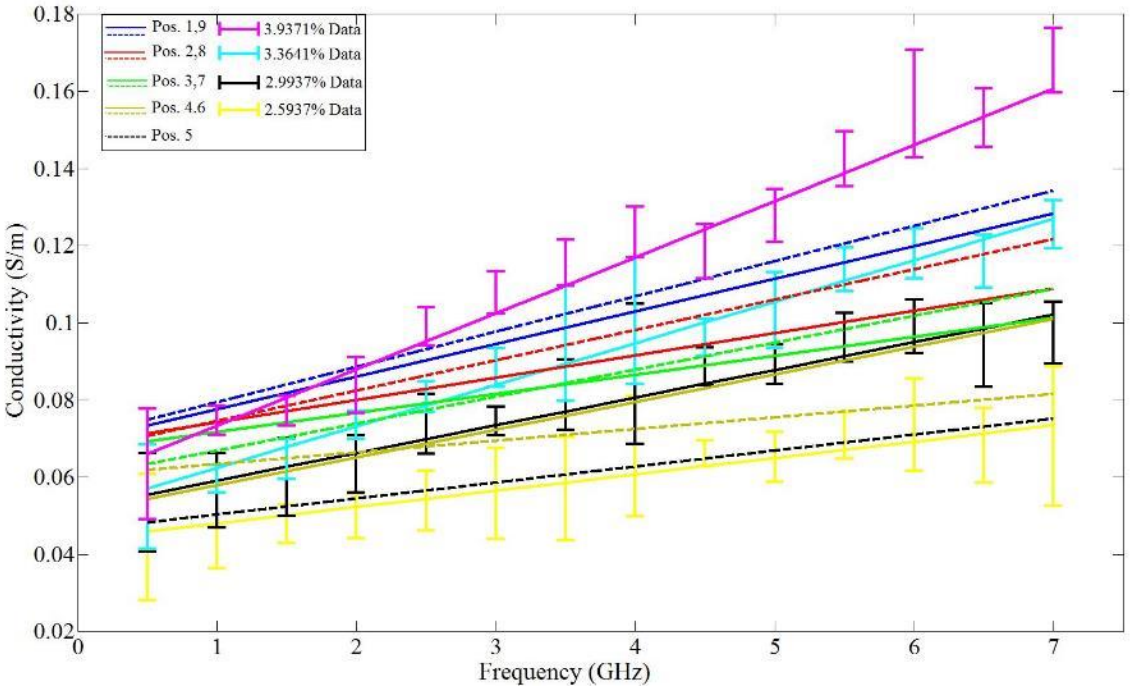


Figure 4.9 Linear regression model of electrical conductivity measurements of adobe brick taken during experiment 2

There is good agreement between the measured dielectric properties of the extracted brick and the properties of the brick samples data when comparing moisture content. For instance, the extracted brick's first position moisture content was measured to be 3.11% and yielded a relative permittivity measure of 3.857 at 7 GHz and 4.609 at 500 MHz. Comparatively, the data of the brick samples resulted in a relative permittivity value of 3.736 at 7 GHz and 4.226 at 500 MHz for a moisture content of 2.967% which shows good agreement between measurements. The results of the extracted brick are shown below in Table 4.4.

Table 4.4 Measurements taken for adobe brick in experiment 2

| Position | Ψ(%) | $\varepsilon_r$ | | $\sigma\ (S/m)$ | |
|---|---|---|---|---|---|
| | | 500 MHz | 7 GHz | 500 MHz | 7 GHz |
| 1 | 3.11 | 4.6092 | 3.8566 | 0.0733 | 0.1283 |
| 2 | 3.09 | 4.377 | 3.7404 | 0.0713 | 0.1089 |
| 3 | 3.04 | 4.2274 | 3.6317 | 0.0692 | 0.1013 |
| 4 | 2.78 | 3.9028 | 3.4172 | 0.0543 | 0.1009 |
| 5 | 2.56 | 3.8655 | 3.351 | 0.0482 | 0.0751 |
| 6 | 2.98 | 3.992 | 3.4473 | 0.0619 | 0.0815 |
| 7 | 3.17 | 4.6371 | 3.8921 | 0.0634 | 0.1088 |
| 8 | 3.22 | 4.6583 | 3.92 | 0.0706 | 0.1217 |
| 9 | 3.25 | 4.7033 | 3.9233 | 0.0749 | 0.1342 |

For a more illustrative comparison, Figures 4.8 - 4.9 compare the dielectric properties of the extracted brick against the data from the brick samples at similar moisture levels. In terms of moisture levels matching adobe samples moisture levels based on dielectric property measurement, the extracted brick from experiment 2 closely matches the dielectric properties measured for similar moisture levels of the adobe samples in experiment 1. The measured electrical conductivity matched well across the entire frequency range as seen in Figure 4.9. There is good agreement in terms of increased moisture content increases the value of conductivity as well as the moisture content of the relative position matching well with the moisture content of the adobe samples for similarly valued conductivity. Meanwhile, the measured relative permittivity closely matches at all frequencies with the exception of the outermost positions at higher frequencies. The relative permittivity measurements align themselves well throughout lower frequencies, but the outermost measurements differ from comparable adobe samples measurements for similar moisture content by a relative permittivity value of

approximately 0.2  at 7 GHz.  With the exception of the small relative permittivity disagreement at the higher frequencies, the dielectric properties and corresponding moisture content measured in experiment 2 matches very well with the dielectric property and moisture measurements taken in experiment 1.  As seen through inspection of Figures 4.8 - 4.9, the moisture content and dielectric property profiles are corroborated through both experiments and confirm the existence of non-uniform moisture profiles present within an adobe brick.

The moisture profile measured for the adobe brick in experiment 2 is shown in Figure 4.10.  Because the moisture content decreases severely at the center of the brick and remains relatively constant at the edges, it can be assumed that the adobe wall will contain a Gaussian shaped moisture profile, and the permittivity measurements on the same brick agree with this assumption as seen especially well in Figure 4.10 by noticing the symmetry of the conductivity values with regards to position.  Thus, an inverted interior wall model previously used in Chapter 3 appears to be a good model profile for adobe walls.

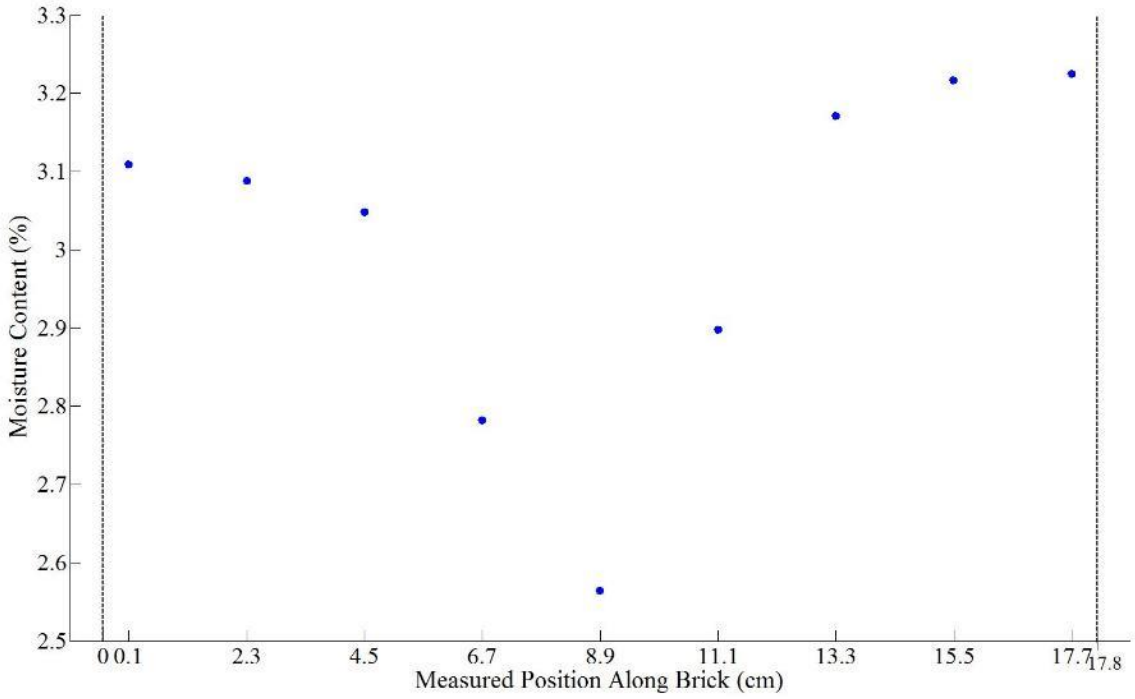


Figure 4.10 Moisture profile measured for adobe brick

## 4.4 Chapter Summary

A rigorous study was undertaken to determine the presence of a non-uniform moisture profile within a wall structure. The measured results show good correlation between multiple experiments and relate the moisture content of the wall to its dielectric properties. The adobe wall tested shows the existence of a non-uniform moisture profile and its impact on the dielectric properties of the adobe material. With accurate models now available for an adobe wall, Chapter 5 details the validation of SINR enhancement provided through the use of matched illumination waveforms designed for TWR which incorporate the moisture profile of the wall. Also, by modeling the wall, theoretical results can be obtained and the dielectric measurements of the wall can be further validated if the radar measurements agree with the simulation results.

# CHAPTER V

# VALIDATION THROUGH USE OF A SIMPLE RADAR SYSTEM TO TRANSMIT OPTIMAL WAVEFORMS

The results and discussions of previous chapters illustrate the potential benefit of using matched illumination waveforms to enhance TWR. Thus far, literature of attempts to validate the simulated radar performance results of computed matched illumination waveforms for TWR is severely lacking; rather, it has only been done for targets located in free space [46]. The following work in this chapter provides validation of the benefits provided through the use of matched illumination waveforms designed for wall models which include accurate moisture profile information by realizing a radar system which transmits the derived optimal waveforms and comparing the results to results occurring in simulation. A conventional radar system is used to produce the optimal waveforms; thus, demonstrating the applicability of using matched illumination waveforms for use in simple, low-cost radar systems.

## 5.1 Introduction

To evaluate the radar performance of transmitting matched illumination waveforms in TWR applications, the waveform must first be designed given *a priori* information of the radar scene. Because the previous work presented in this study has yielded accurate material properties of an adobe wall, this information can be used in the

design of an optimal transmission waveform through matched illumination theory. Then, the optimal waveform can be applied to an adobe wall that matches the measured properties of the adobe wall. That is, a TWR scenario including an adobe wall and simple target is set up in an anechoic chamber and evaluated for radar performance (specifically received power and resulting SNR). The anechoic chamber is ideal for performing a comparison to simulation results as it creates a near-ideal environment for wave propagation. The anechoic chamber is a shielded room which eliminates noise from the outside environment while the interior floors and walls are filled with pyramidal absorbers which reduce or eliminate unwanted reflections.

For all measurements in the anechoic chamber, FDTD simulation results are used for comparison. Again, the Angora FDTD software package is used for these simulations which models the adobe wall according to the measured dielectric properties with the given target located behind the wall. To create the adobe wall model which matches the measured results, a multiple linear regression model is produced using the moisture and dielectric properties over the frequency range considered.

Multiple linear regression attempts to model the relationship between two or more independent variables and a response variable by fitting a least squares function to the observed data. Thus, in the case of modeling the adobe wall's dielectric properties, the multiple linear regression model is of the form

$$\varepsilon_r^i = \beta_0 + \beta_1 \Psi_i + \beta_2 f_i + \beta_3 \Psi_i f_i$$

where $\beta$ is the regression coefficients, $\varepsilon_r^i$ is the relative permittivity, $\Psi$ is the moisture content, and $f$ is the frequency of the $i$th observation (measurement). Similarly, the

regression model for electrical conductivity follows the same format, but replace $\varepsilon_r^i$ with $\sigma^i$. After minimizing the sum of the square error of the model function, the best fit line is found for $\beta$ coefficients. Resultantly, given the regression $\beta$ coefficients, the dielectric properties can be estimated for any value of moisture content $\Psi$ and frequency $f$. In this work, this is accomplished using the *regress* function in MATLAB, and the resulting adobe wall model properties are estimated for the moisture profile measured in Chapter 4 and shown in Figure 4.10 which is then modeled in Angora. The relative permittivity and conductivity profile of the adobe wall modeled in Angora was estimated using multiple linear regression models with independent variables of moisture and frequency and are shown in Figure 5.1.

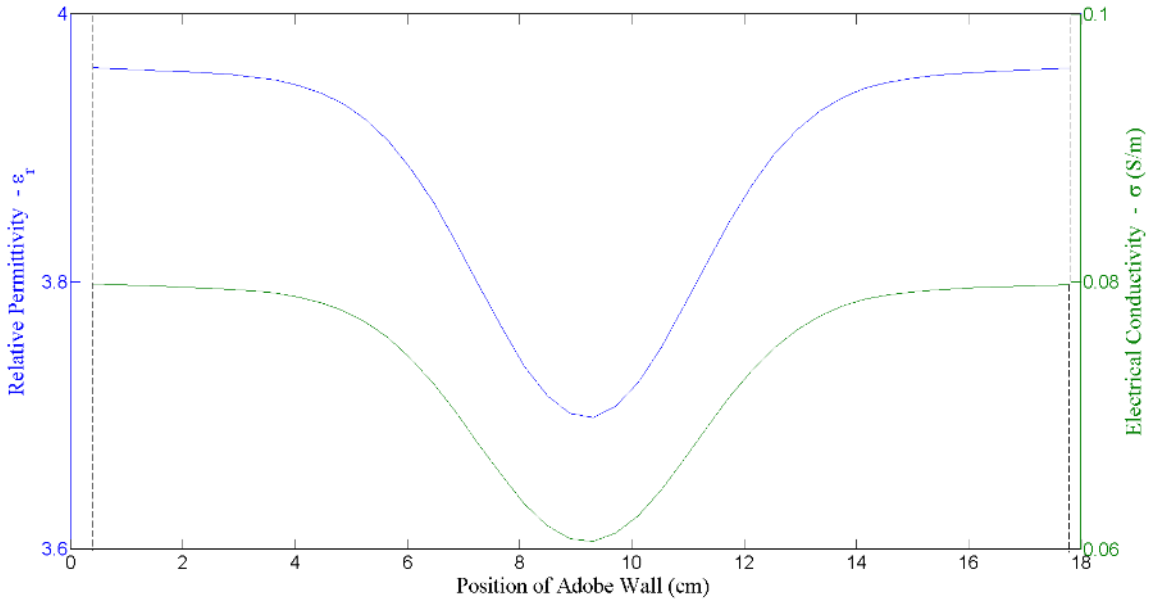


Figure 5.1 Adobe wall dielectric profile as modeled in Angora using measured moisture and dielectric properties

### 5.1.1 Attenuation Due To Adobe Wall

The first experiment conducted in the anechoic chamber is the measurement of attenuation versus frequency for an adobe wall over the frequency range of 1 - 4 GHz to ensure that the dielectric properties of the adobe wall measured previously and presented in Chapter 4 are accurate. Additionally, attenuation experienced propagating through a certain wall is useful information to radar system design of through-the-wall environments. The measured through-wall attenuation is compared to the attenuation predicted by the simulated through-wall model using measured dielectric property values. A line of sight radar configuration is used for measurements of the power received in this experiment.

To provide this comparison, the path loss was first measured in the anechoic chamber so that loss due only to wave propagation in free space could be accounted for in the case of the wave propagating through the wall. The free space path loss (FSPL) is often used in RF applications for predicting signal strength that may be expected in communications systems. The FSPL is derived from the Friis transmission equation which estimates the signal strength at a given point in a transmit-receive system. That is, the power received at an antenna in free space is

$$P_r = \frac{P_t G_t G_r}{L L_t L_r} \tag{5.1}$$

where $P_t$ is the transmitted power, $G_t$ and $G_r$ are the gains of the transmitting and receiving antennas, $L_t$ and $L_r$ are the losses of the radar system (transmitting losses, receiving losses) and $L$ is the free space path loss [101]. All units of gains $G$ and losses $L$

are expressed as power ratios and the powers $P$ are in Watts. In the far field of the transmit antenna, the FSPL is given by

$$L = \frac{(4\pi)^2 d^2}{\lambda^2} \tag{5.2}$$

where $d$ is the distance between the antennas and $\lambda$ is the transmitted wavelength. Thus, the FSPL only depends on the distance traveled and transmission frequency and can be used to approximate the power received for the radar system used in a line of sight radar configuration. After, the power received is measured in free space ($P_{fs}$), the adobe wall is placed between the two antennas and the power received is again measured ($P_w$). Resultantly, the power loss or attenuation due to the wall ($L_w$) can now be calculated as $L_w = P_{fs} - P_w$.

To compare the attenuation due to the wall ($L_w$), the attenuation constant $\alpha$ is calculated for an adobe wall given the measured values of its dielectric properties. Propagation losses or attenuation due to a homogeneous wall ($L_w$) can be computed as

$$L_w = e^{-2t_w\alpha} \tag{5.3}$$

where $t_w$ is the thickness of the wall and $\alpha$ is the attenuation constant derived from the solution of the plane wave equations of electromagnetic fields. The attenuation constant $\alpha$ is calculated as

$$\alpha = 2\pi f \sqrt{\frac{\varepsilon'_w \mu_w}{2}\left(1 + \left(\frac{\sigma_w}{2\pi f \varepsilon'_w}\right)^2 - 1\right)} \tag{5.4}$$

where $\varepsilon'_w$ is the permittivity (real) of the wall ($\varepsilon'_w = \varepsilon_{rw}\varepsilon_0$), $\mu_w$ is the permeability of the wall ($\mu_w = \mu_r\mu_0$), and $f$ is the frequency of the propagating wave in Hz.

Because the wall is not homogeneous, the dielectric properties within the walls change as a matter of position; thus, the attenuation due to the wall has to account for the change in dielectric properties as the wave propagates through the wall. That is, the attenuation constant must be calculated for each layer considered (measured or modeled) and then summed across all layers to give a total level of attenuation. Hence, the attenuation for the multilayered wall is

$$L_w = \sum e^{-2t_w^i \alpha_i} \tag{5.5}$$

where $t_w^i$ is the thickness of the $i$th layer and $\alpha_i$ is the attenuation constant of the $i$th layer. Expressed in decibels, the loss due to the wall is $L_w(\text{dB}) = 10\log_{10} L_w$.

### 5.1.2 Radar Performance of Matched Illumination Waveforms

To evaluate the radar performance of transmitting matched illumination waveforms designed for the adobe wall and target, optimal waveforms are generated and transmitted through a monostatic radar system in order to determine the level of target echo power the antenna receives and the resulting SNR. The wall considered is an adobe wall and the target is an aluminum plate. Of particular concern in this study is the ability of the signal generator to produce an exact replica of the optimal waveform; as later discussed, the generator cannot always exactly match the optimal waveforms (or at least the waveforms designed in this study) and consequently must produce a near-optimal waveform. The resulting SNR of the optimal matched illumination waveforms are compared to non-optimal waveforms to illustrate the radar performance enhancements created through the use of matched illumination waveforms for TWR problems. The matched filter SNR output is provided by (1.10) where the scattered field autocorrelation

matrix $\boldsymbol{R}_S$ is formed by the scattered field received at the antenna in the anechoic chamber measurements.

## 5.2 Equipment and Experimental Setup

The radar system used in this work utilizes two identical horn antennas which construct either a line of sight transmit/receive configuration or a pseudo-monostatic configuration. Figure 5.2 provides a block diagram of the hardware used during the testing. The line of sight configuration is used for measurements detailed in Chapter 5.1.1, whereas the pseudo-monostatic configuration is used for radar measurements detailed in 5.1.2. The antenna configurations used in this work are shown in Figure 5.3 and Figures 5.5 - 5.7. While technically the pseudo-monostatic configuration used is a bistatic radar system comprising of a separate transmitter and receiver, the bistatic angle is near zero and the antennas are collocated. Resultantly, this bistatic configuration can be regarded as monostatic. The monostatic configuration is preferable for the measurements in this study because it matches typical through-wall surveillance missions wishing to have as little footprint as possible while also allowing simpler, normal incidence calculations simulations to be used.

The horn antennas are both Com-Power Corp. Model AH-118 antennas which are double ridged waveguide broadband horn antennas [104]. This antenna is linearly polarized and designed to operate in the $1 - 18\ GHz$ frequency range. The transmit and receive antennas are set up for vertical polarization (ridges are perpendicular to floor) for all tests completed in this work. When the antenna setup was in a monostatic configuration, ECCOSORB LS-30 absorbing material was placed between the antennas to reduce the antenna coupling.

The transmitted radar waveform is generated with an Agilent N5183A MXG signal generator and output to the transmit antenna through an amplifier. The signal sent to the transmit antenna from the amplifier is amplified to 40 dBm. The signal generator used in this work is capable of providing continuous wave (CW) signals from 100 kHz to 20 GHz. It also has the ability to transmit modulated signals in the form of amplitude modulation (AM), frequency modulation (FM), and phase modulation (ΦM). The receive antenna's data is collected using a Tektronix DPO 72004 Digital Phosphor Oscilloscope. The oscilloscope's bandwidth is 20 GHz, with a 50 GS/s sample rate capable of recording 62.5 Msamples.

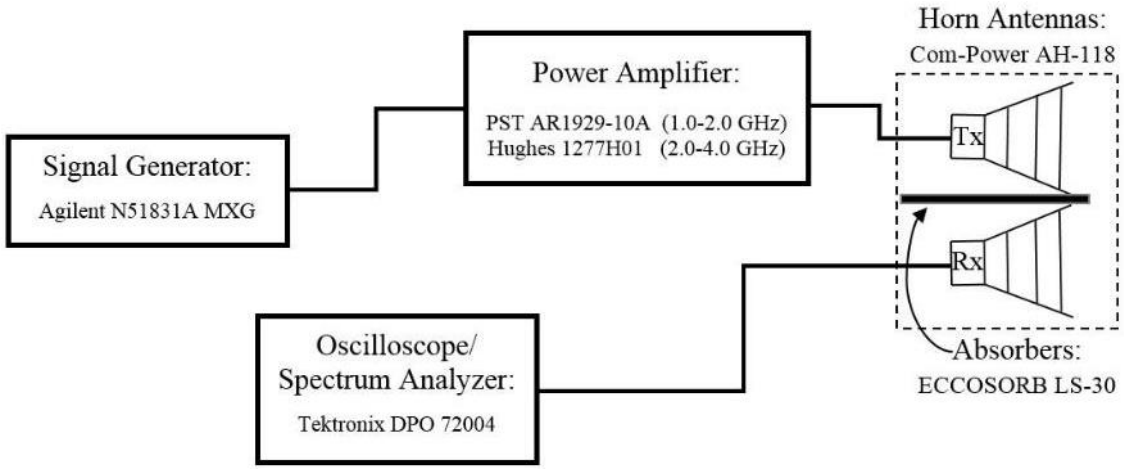


Figure 5.2 Anechoic chamber measurement equipment

For all anechoic chamber experiments completed in this work, a set of typical hardware parameters were used during testing. To provide information and comparison data across the frequency range of interest for all radar tests, uniform (unmodulated) pulses of equal energy (40 dBm) and extent (50 μs) were transmitted at frequencies

ranging from 1 to 4 GHz in steps of 100 MHz. To ensure complete measurement of the radar signals with high resolution, the oscilloscope was set to measure at a sample rate of 25 GS/s over a duration of 80 μs which yields a record length of 2 Msamples at a resolution of 40 ps.

Multiple adobe wall test articles were available for the measurements and testing throughout this work. One of the adobe wall test articles was used for measurement which resulted in destruction of the wall, and another adobe wall was used as the wall in the radar testing completed in the anechoic chamber. Both adobe walls were composed using identically fabricated adobe bricks which were arranged and mortared together to form the wall in a similar manner. Thus, each adobe wall was created to resemble one another as closely as possible in order to allow the wall used in radar testing to match the wall used in dielectric property and moisture measurement. The adobe wall used during testing in the anechoic chamber was 1' 7" × 2' 1" × 7" or equivalently 0.45 m × 0.63 m × 0.18 m (height × width × thickness). However, 4" of absorbing material was placed around all edges of the wall as seen in Figure 5.3 (b.); thus, with the absorbing material placed around the edges of the wall, the exposed area of the adobe wall used during testing in the anechoic chamber was 11" × 1' 5" or equivalently 0.2794 m × 0.4318 m (thickness remains unchanged).

To maintain plane wave conditions for the entire area of the illuminated wall, numerical calculations were undertaken which calculated the radiation pattern of the antenna and the area in which the transmitted wavefront met plane wave criteria. How to ensure plane wave conditions and the calculations showing that plane wave conditions were met for all experiments in this work is presented in Appendix B. Additionally, to

ensure the wall in the anechoic chamber matches the simulations and appeared “infinite”, the absorbing material was placed around all edges of the wall to minimize edge effects.

### 5.2.1 Attenuation Due to Wall - Experimental Setup

To begin the first experiment, the two horn antennas are placed 5.785 m from one another as illustrated in Figure 5.3 with the exception of the wall being absent (wall thickness is 18 cm). Then, the free space loss (path loss) was measured and compared to the calculated FSPL for the radar system. Next, an adobe wall was placed inside the anechoic chamber. For the line of sight configuration, the adobe wall was placed 5.105 m from the transmitting antenna and the receiving antenna was located 0.5 m behind the wall as illustrated in Figure 5.3. The transmit and receive antennas were placed at those respective distances from the wall due to ease of setup within the chamber while also maintaining plane wave illumination of the material under test (MUT) and far field conditions.

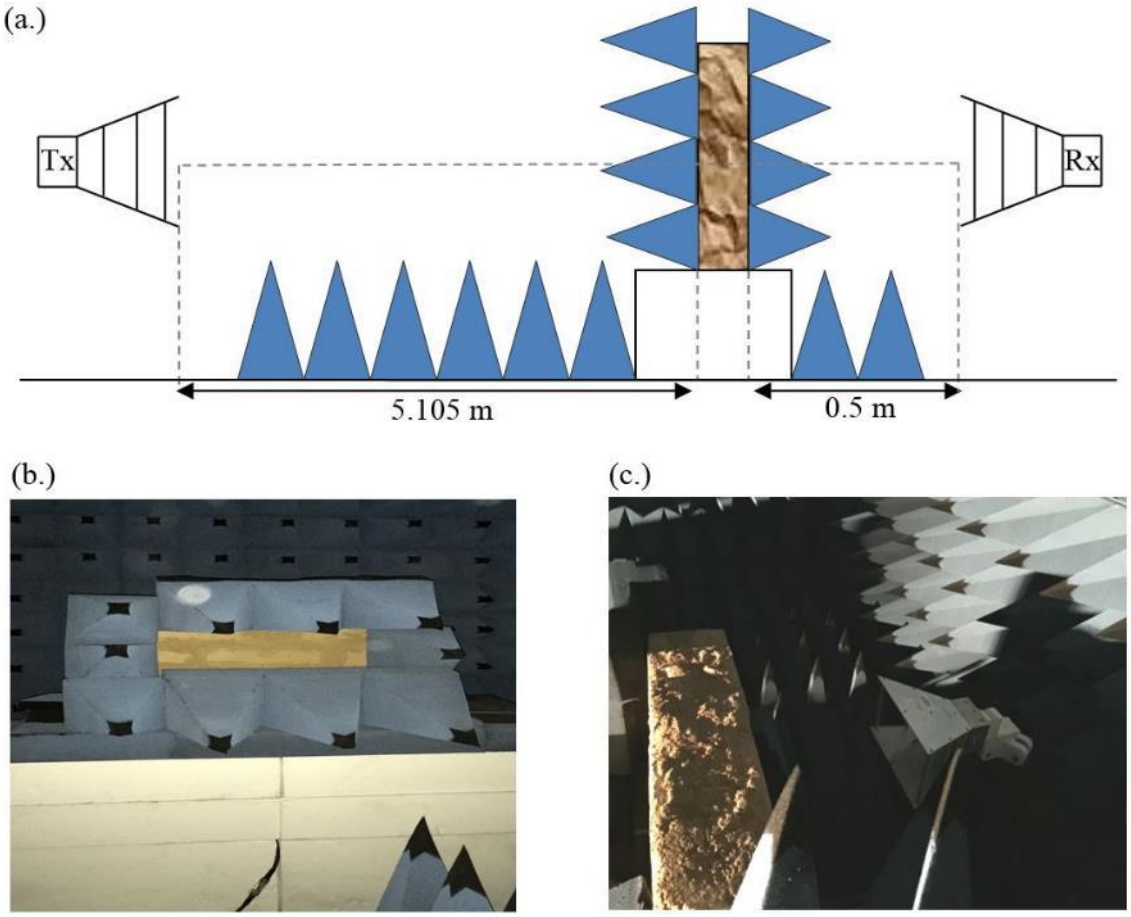


Figure 5.3 Line of sight radar system configuration with wall

(a.) Diagram of line of sight radar system configuration
(b.) Transmission side of radar system with MUT shown
(c.) Receiving side of radar system with MUT shown

Again, the transmitter antenna was used to propagate uniform pulses of equal power and length at a specific, narrowband carrier frequency $f_c$. The carrier frequencies varied from 1 GHz to 4 GHz in steps of 100 MHz. The power received by the antenna was recorded by the oscilloscope which recorded both field and spectrum measurements (time-domain and frequency-domain) for each frequency. The measurements are then compared to the expected received power calculated from (5.1) - (5.5) using the dielectric properties measured for the adobe wall.

### 5.2.2 Radar Performance of Matched Illumination Waveforms - Experimental Setup

Figures 5.5-5.6 detail the measurement setups of the monostatic radar system. The horn antennas are positioned close to one another and remain in identical orientations. They are located 5.105 m from the front of the adobe wall so that the plane wave illumination and far field conditions of the MUT are met. In the first set of monostatic testing, an aluminum plate ($8'' \times 8'' \times 0.08''$) is placed 16.5 cm behind the adobe wall. Note that the plate is tested in two different arrangements to provide more comparison data as well as measure frequency responses which will provide clear illustration of the benefits provided through matched illumination waveform design. The plate arrangements are such that the transmission waveform will be incident upon the plate face as well as incident upon the edge of the plate as illustrated in Figure 5.4 below. It is also noted that the edge-on plate arrangement shown in Figure 5.4 (b.) features the same aluminum plate cut to dimensions of $8'' \times 1'' \times 0.08''$. The different plate sizes and orientations considered here produce target resonances at different frequencies over the frequency band of interest. Below, Table 5.1 details the series of experiments completed during the monostatic configuration testing. The series of tests listed are completed for both arrangements of the target (face-on and edge-on).

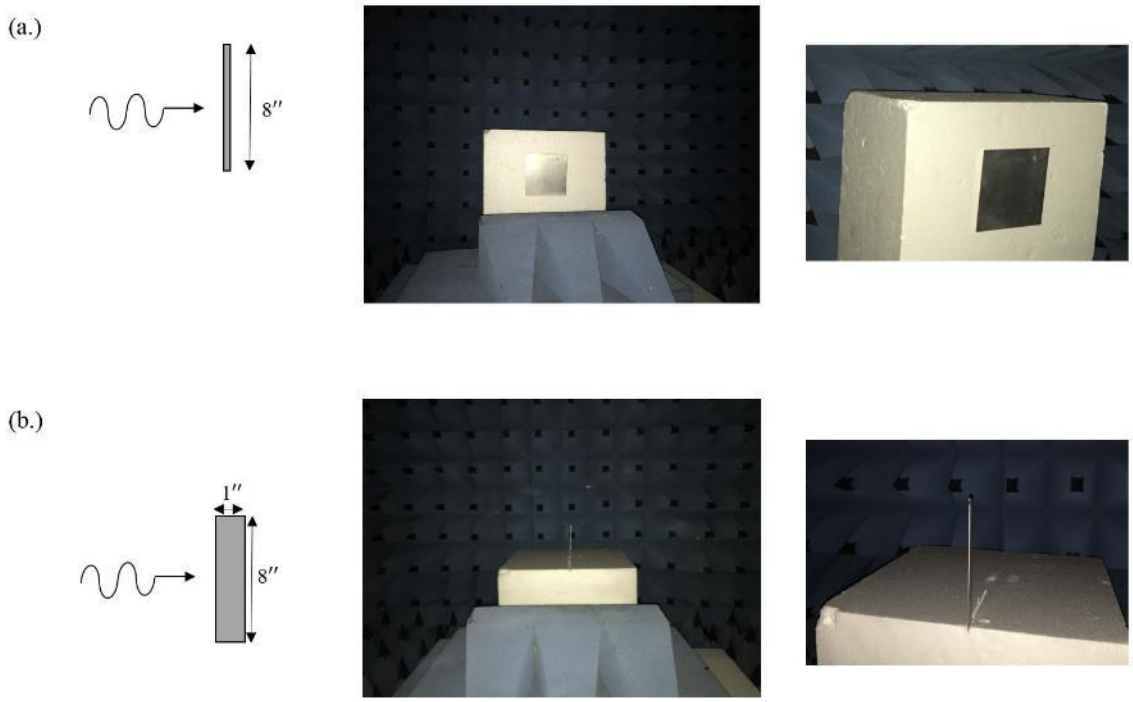


Figure 5.4 Plate target positioning detailing face-on and edge-on arrangements

(a.) Face-on plate target arrangement
(b.) Edge-on plate target arrangement

Table 5.1 Details of anechoic chamber test series for monostatic configuration

| Test # | Setup | Reason |
|---|---|---|
| 1 | Freespace | Eliminate any remaining antenna coupling/crosstalk |
| 2 | Target only | Confirm simulated frequency response |
| 3 | Wall only | Wall reflection removal from wall/target data |
| 4 | Target behind wall | Compare SNR for waveforms |

Again, the base transmitted signals during this testing are narrowband, uniform pulses of equal power and length at specific carrier frequencies from 1-4 GHz. However, the matched illumination waveforms derived in simulation are also propagated. For the wall/target scenarios considered here, the resulting optimal waveforms contain only one major frequency component and a close approximation of the waveforms can be

generated using simple modulation schemes. In fact, when the optimal waveform contains one major frequency component, it is well approximated by a uniform pulse waveform provided that the transmission duration is sufficiently long ($t \gg \frac{1}{f_c}$) where time $t$ is in seconds and the major frequency component $f_c$ is in Hz [35]. Given that the length of the optimal waveform's is directly dependent on the number of columns in the target's impulse response matrix (1.14), an appropriate pulse length can be defined in the optimization process by simply zero-padding the matrix such that the desired pulse width is attained [31, 35]. Additionally, to compare to conventionally used radar waveforms, linearly frequency modulated (LFM) waveforms were also transmitted. The LFM waveforms used were carried at frequencies of (3.04 GHz, 3.12 GHz, …, 3.96 GHz) with maximum frequency deviations of 40 MHz based on the FM limitations of the signal generator. The LFM waveform is commonly used in radar applications due to its near constant spectrum over the specified frequency band.

The data in this experiment was collected in the time domain by the receive antenna and recorded with the oscilloscope. The exact timing of the trigger level is a vitally important parameter for these measurements due to removal of the antenna crosstalk and wall reflection data. Hence, for measurements recorded in this study, it was found that using an oscilloscope measurement setup which recorded the average of 5000 waveforms (echoes), the timing of the recorded data aligned nearly perfectly for all data. The averaging also considerably decreased the noise in the measurement. In the event, that the data was not perfectly aligned in the time-domain, signal processing techniques were used to determine the number of samples needed to adjust the misaligned measurement to the correct time through cross correlation of the antenna crosstalk.

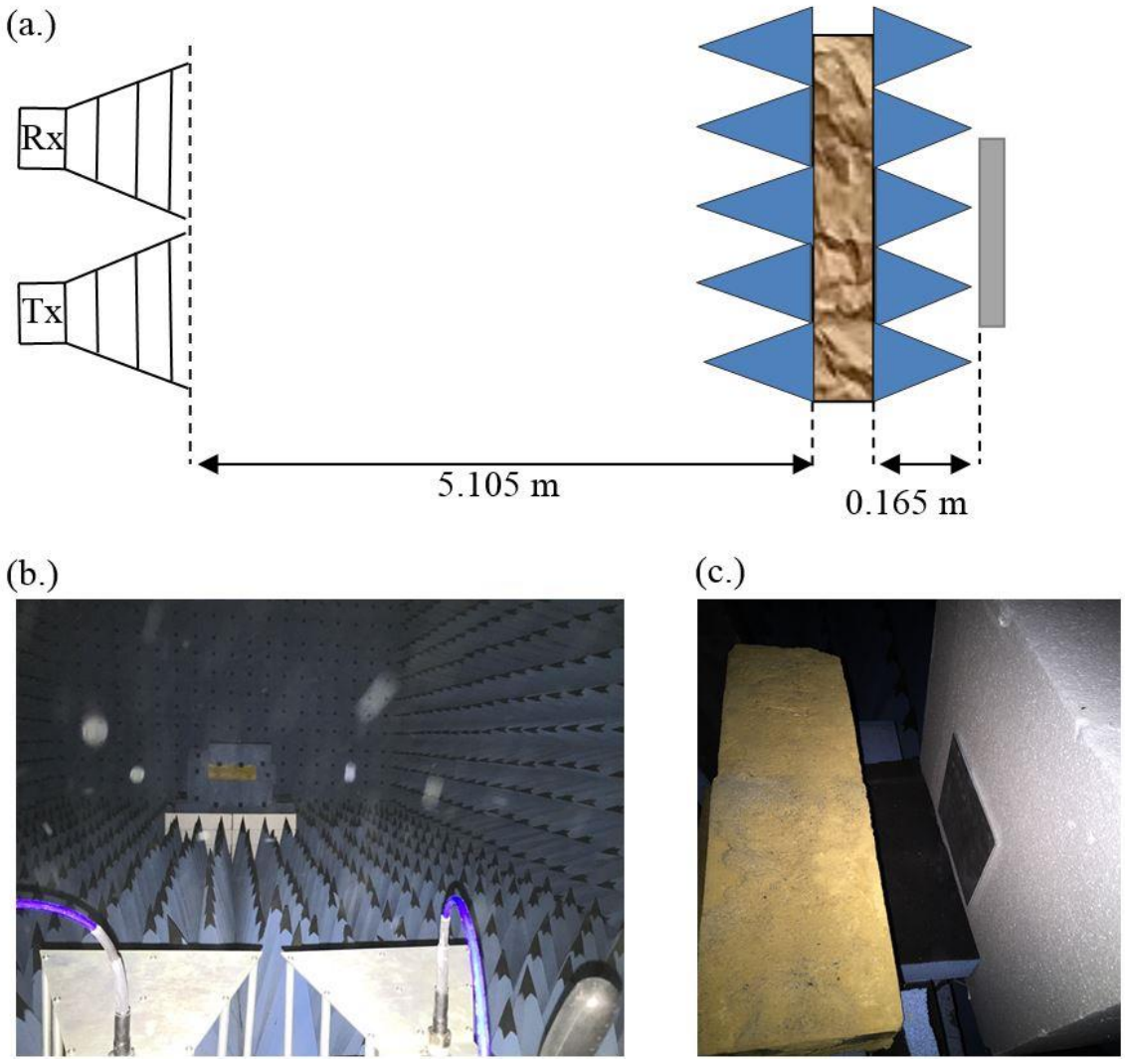


Figure 5.5 Monostatic configuration for adobe wall and face-on aluminum plate target

(a.) Diagram of monostatic configuration from a top-down view
(b.) View of monostatic configuration from behind the antennas
(c.) Aluminum plate target (face-on) placed behind wall

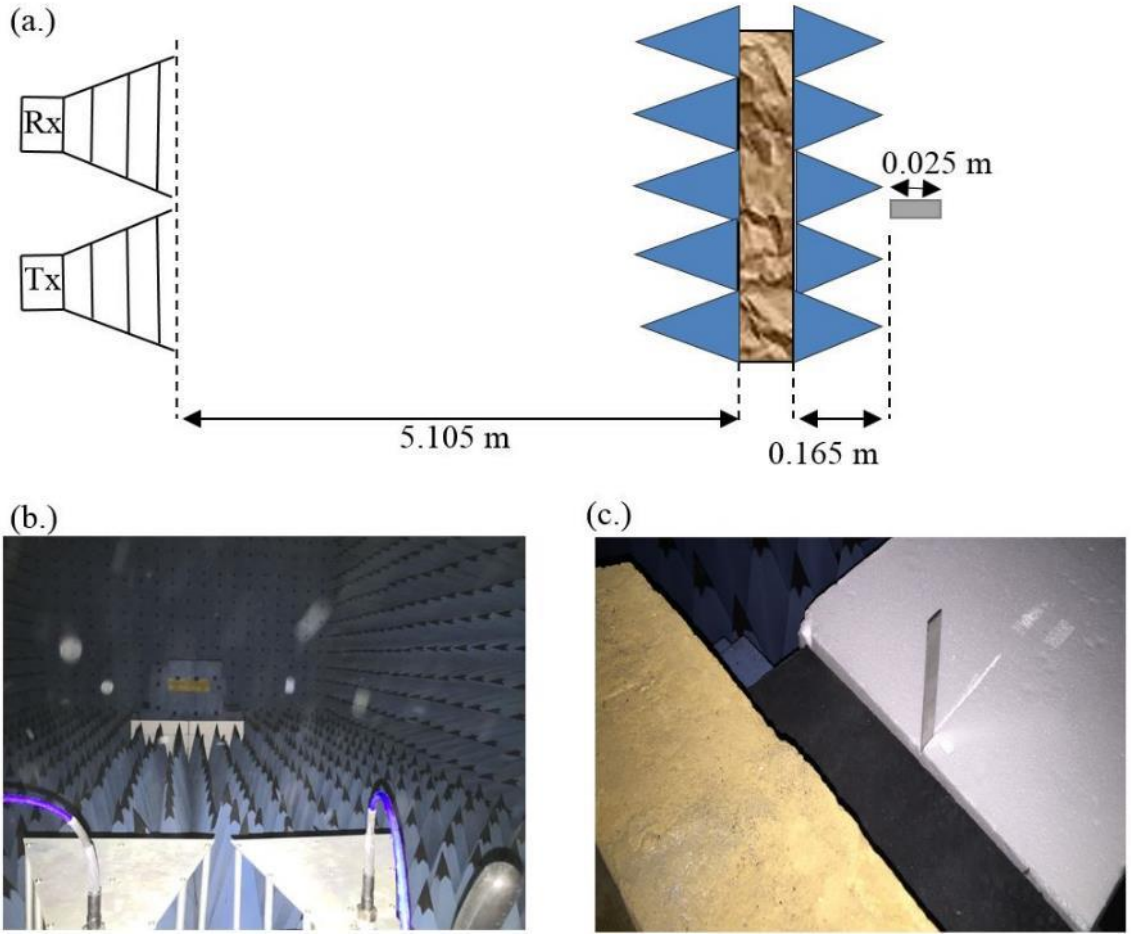


Figure 5.6 Monostatic configuration for adobe wall and edge-on aluminum plate target

(a.) Diagram of monostatic configuration from a top-down view
(b.) View of monostatic configuration from behind the antennas
(c.) Aluminum plate target (edge-on) place behind wall

Antenna crosstalk or coupling consists of waveform energy directly traveling from the transmitting antenna to the receiving antenna. Thus, for a fixed configuration, this energy is present for all measurements. In the monostatic configuration used during testing, significant antenna crosstalk was present. To combat this crosstalk effect, ECCOSORB LS-30 absorbing material was placed directly between the two horn antennas to attenuate any signals traveling perpendicular to the desired transmission

direction. As illustrated in Figure 5.7, four sheets of ECCOSORB were placed between the horn antennas shown in Figures 5.5 - 5.6 (b) during testing with each absorbing sheet being 0.32 cm thick and rated for attenuation of at least 24 dB/cm from 1 - 26 GHz. Additionally, the free space measurements were used to remove any remaining crosstalk energy in the signal by direct signal subtraction (similar to wall reflection removal).

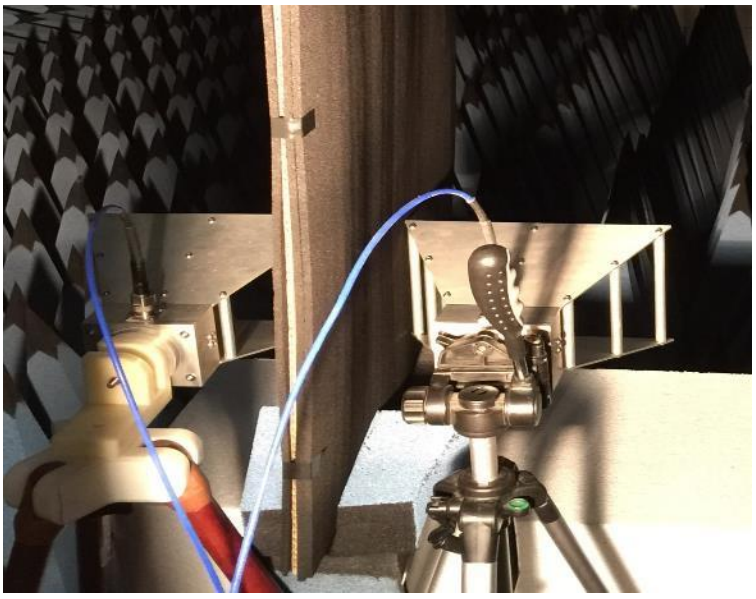

Figure 5.7 Absorbing material placed between horn antennas during monostatic operation

## 5.3 Measurements and Results

All frequency response measurements performed here utilized 50 μs uniform pulses transmitted at frequencies of $f_c^i = [1.0\ \text{GHz}, 1.1\ \text{GHz}, \ldots, 4.0\ \text{GHz}]$. For the monostatic radar experiment, LFM radar waveforms were also transmitted from 3 GHz to 4 GHz with frequency deviations of 40 MHz to compare to the uniform pulses and optimal waveforms. The oscilloscope sampled 25 GS/s for 80 μs which easily met the

Nyquist sampling criterion for the frequencies transmitted and measured in this work while allowing sufficient travel and echo convergence times. The cable losses of the system were also measured at each frequency and used in processing the calculations provided. As discussed below, the radar measurements taken in the anechoic chamber were in agreement with both the calculated results and FDTD simulations.

### 5.3.1 Attenuation Due to Adobe Wall - Results

Following the configuration of Figure 5.2 and setup described in Chapter 5.2.1, Figure 5.8 shows the comparisons between the calculated and measured received power in free space and behind the adobe wall. Figure 5.9 displays the measured power loss that occurs after propagating through the adobe wall as well as the simulated and estimated power loss.

The estimation of the power received from the Friis transmission equation differs slightly from the measured power received in free space as seen in Figure 5.8. However, the difference remains within $\pm$ 3 dB which is typical for pyramidal horn antennas [96]. Differences are attributed to errors in the measurement setup and non-exact values of gain for all frequencies evaluated. There is also good correlation between the power received behind the wall for two separate measurements, labeled trial 1 and 2. Following the procedure defined in Chapter 5.1.1 and subtracting the free space power received from the power received behind a wall will provide the power loss caused by the adobe wall ($L_w = P_{fs} - P_w$). In Figure 5.9, the measured power loss caused by the adobe wall is compared to both the simulated attenuation and estimated wall attenuation based on the wall attenuation constant calculation of (5.5). Again, there is good agreement between the simulated and estimated wall power losses with the measured wall power loss. Thus,

the wall model created with measurements of the adobe samples in Chapter 4 is an accurate representation and yields results comparable to measured data. With the regression model's resulting dielectric properties matching well with the measured results, the benefits of matched illumination waveforms is investigated next with confidence that the wall model well represents the actual wall encountered in measurement.

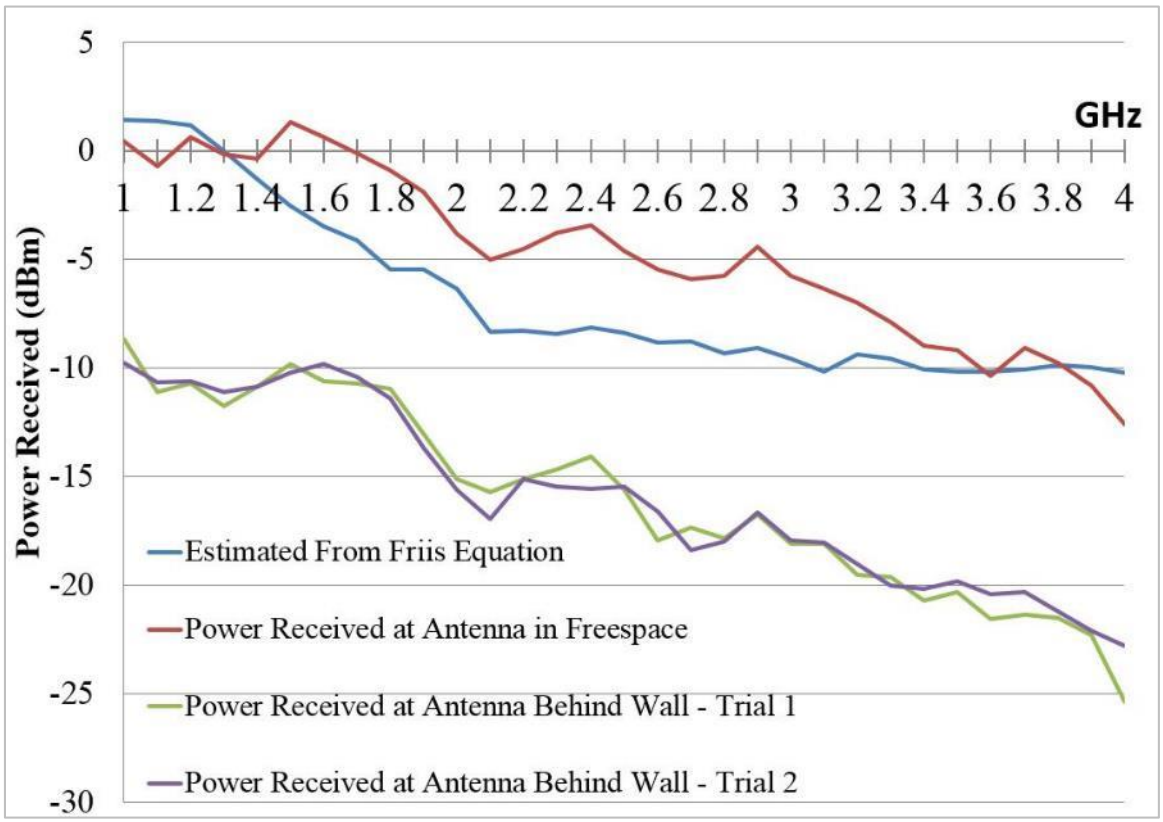


Figure 5.8 Power received at antenna using line of sight radar configuration (free space and behind wall)

The estimated power received from Friis transmission equation uses the equal respective transmitted powers, distance, frequency, antenna gains, and cable losses as experienced in the anechoic chamber. The power received behind the wall was taken for two separate trials.

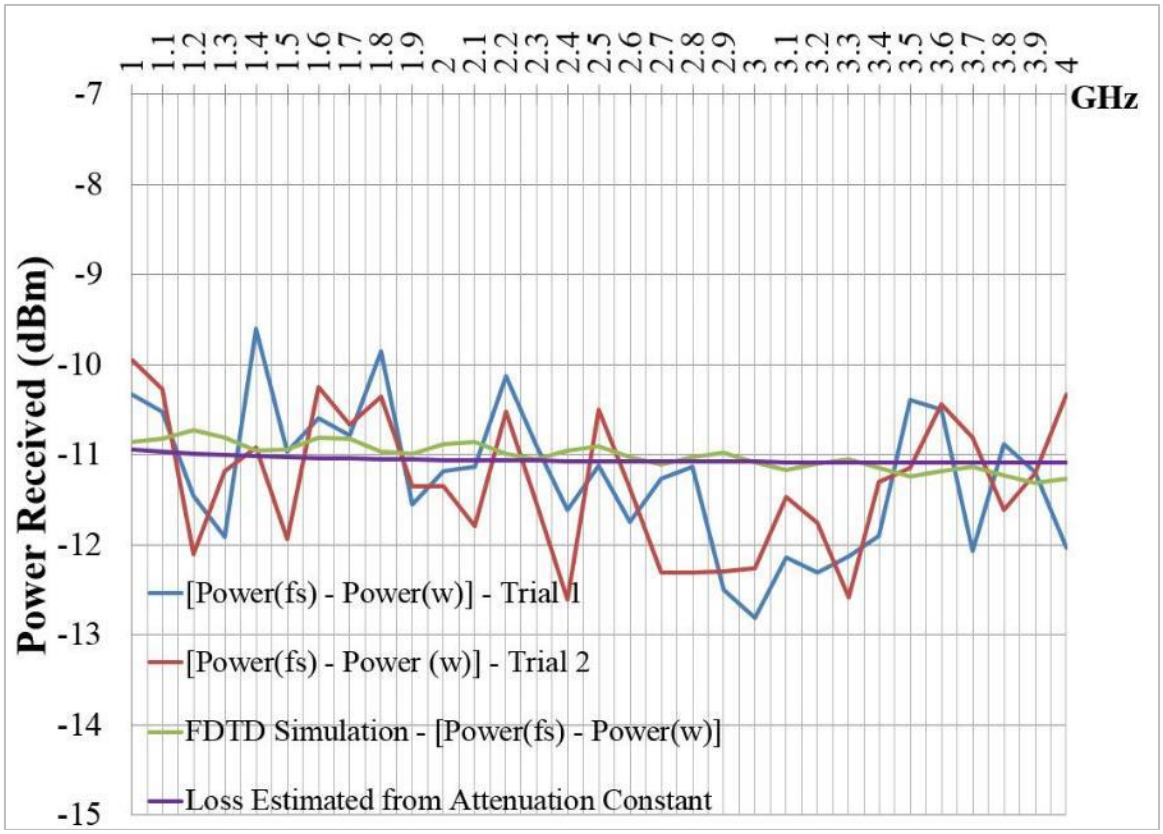


Figure 5.9 Attenuation due to the adobe wall where Power(fs) is the power received in free space and Power(w) is the power received behind the adobe wall

### 5.3.2 Radar Performance of Matched Illumination Waveforms - Results

To compare the radar performance of matched illumination waveforms, the monostatic radar system discussed in Chapter 5.2.2 and shown in Figures 5.5 – 5.6 were used. The noise floor used in SNR calculations is shown in Figure 5.10 and was measured with the oscilloscope over the frequency range of interest. The noise floor measured exhibits a relatively flat response with a mean noise level of -95.4055 dBm.

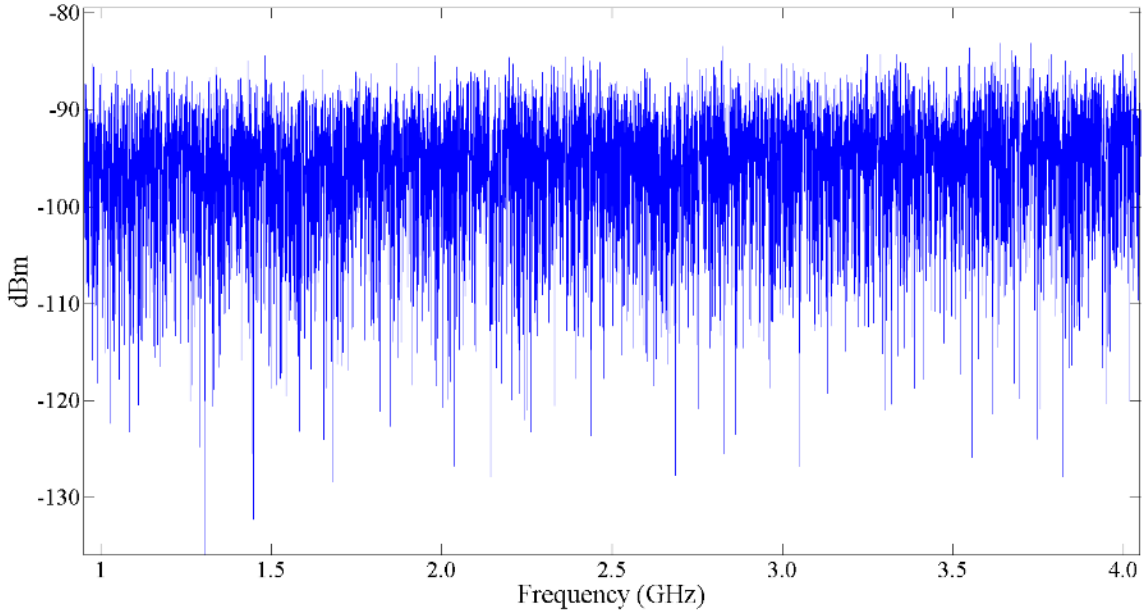


Figure 5.10 Measured noise floor over frequency range of interest

#### 5.3.2.1 Results of Face-on Aluminum Plate Target Arrangement

First, Figure 5.11 is shown to illustrate the simulated transfer functions of the adobe wall, face-on aluminum plate target, and combined wall/target response along with the resulting matched illumination waveform for the matching simulation setup using the adobe wall model produced through the multiple linear regression model mentioned previously. The wall's transmission frequency response is relatively flat across the spectrum whereas the face-on plate target's response is somewhat exponential as the frequency increases. Hence, the target's scattering response more heavily influences the optimal waveform derivation which designs an optimal waveform which contains significant energy at the upper most frequency point considered. This is where the target's scattering response peaks as well as the full-wave wall/target impulse response peaks. To confirm proper simulation and anechoic chamber measurements, the target's

scattering response is measured and compared with simulation in Figure 5.12 below. The face-on target's response matches very well with the simulated results by having only a 0.8177 dBm absolute mean error while also matching the increasing nature of the target's response over the entire frequency range.

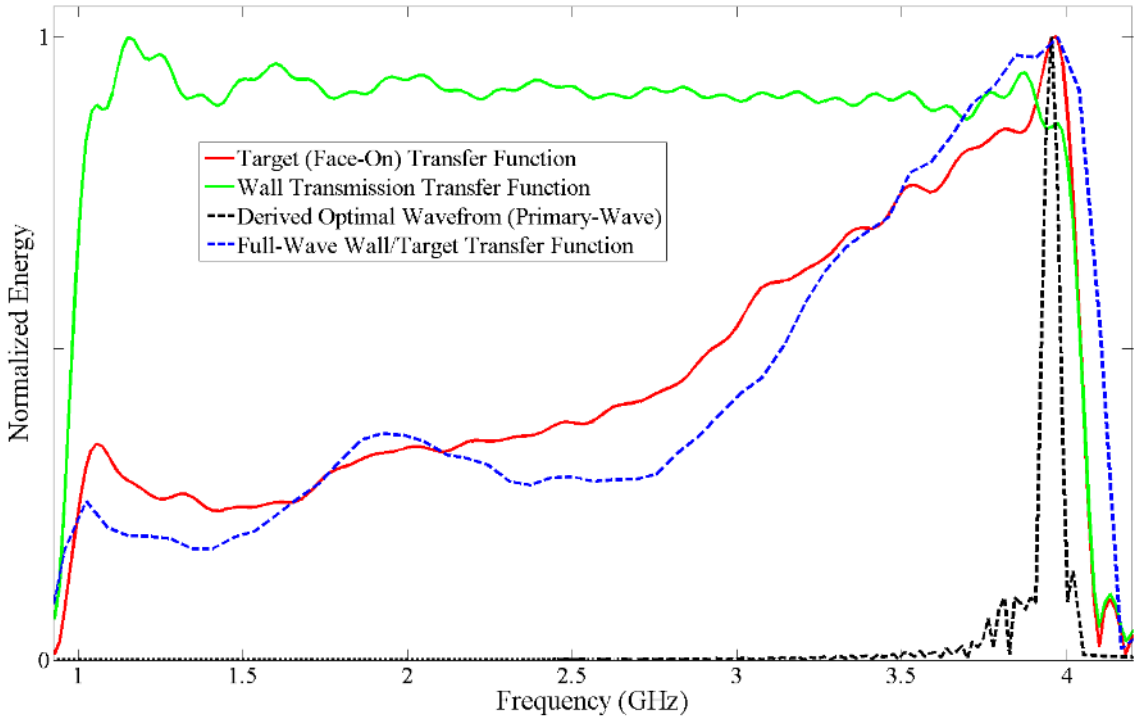


Figure 5.11 Wall and target transfer functions along with the primary-wave and full-wave wall/target transfer functions and derived optimum waveform for adobe wall and face-on aluminum plate target

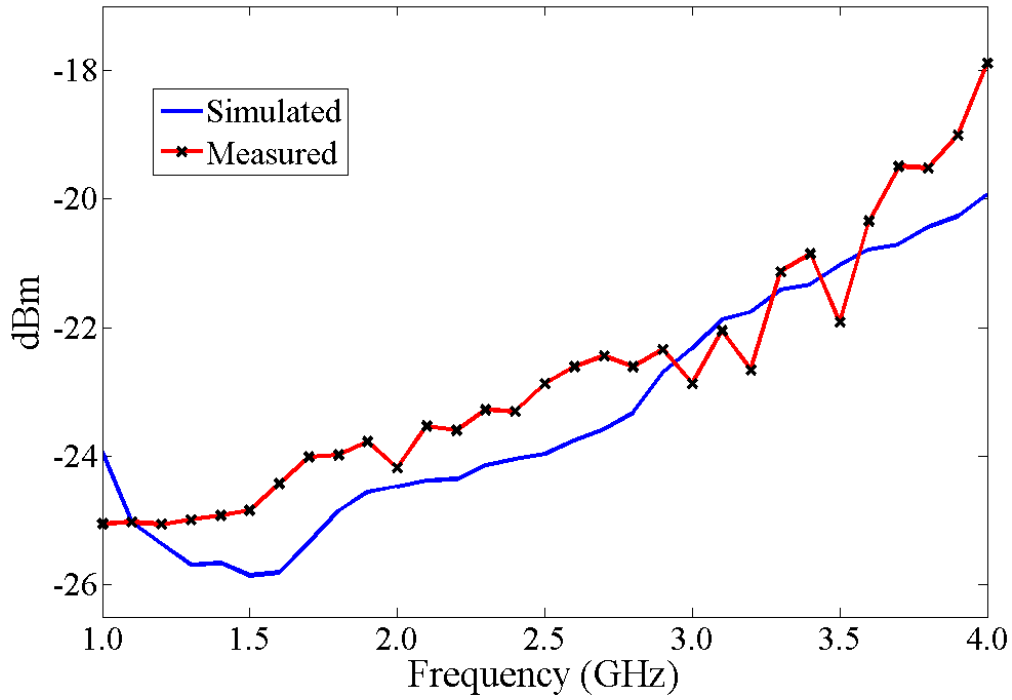


Figure 5.12 Face-on aluminum plate target scattering response comparison

The derived matched illumination waveform is found for the primary-wave wall/target impulse response as formulated in [31-36, 75, 87-88], but it is clear that the true optimal waveform would have significant energy located at the peak of the full-wave wall/target impulse response which is located at 4.0 GHz rather than 3.95 GHz. Thus, the slightly sub-optimal waveform production is a result of assumptions in the waveform derivation scheme using the primary-wave impulse response as previously discussed in Chapter 2. The matched illumination waveform derived in simulation was then generated using the Agilent waveform generator by simply adding amplitude modulation to the uniform pulse carried at a frequency of 3.95 GHz. The designed optimal waveform and generated optimal waveform are shown below in Figure 5.13. To properly generate the optimal waveform, the time from the max amplitude of the derived waveform to its zero

convergence point was measured and the AM rate was inferred. Because the time of the pulse width is approximately 25 ns, the AM rate was found to be approximately 20 MHz found via $\left(\frac{1}{2}\right)\left(\frac{1}{25\text{ ns}}\right) \approx 20$ MHz where only half of the sinusoidal modulation cycle over that time length is needed. Noticing that the derived waveform appears to go from zero to its maximum, it can also be inferred that the AM depth is 100%.

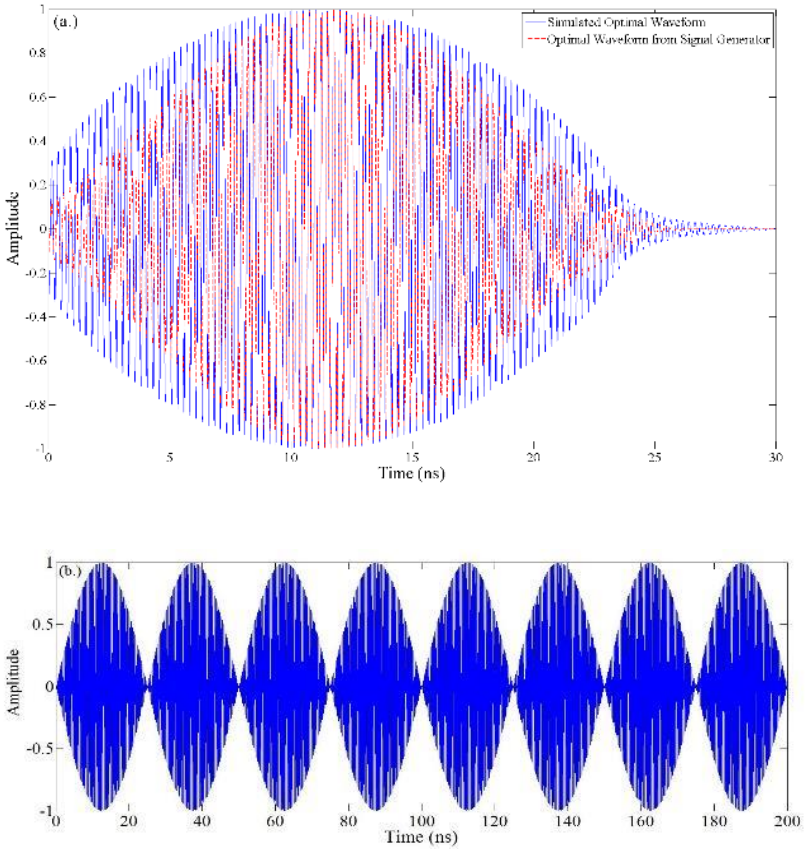


Figure 5.13 Optimal waveform generated by signal generator
(a.) Waveform generation of AM waveform to match derived result
(b.) Entire AM waveform over 200 ns

Only the trailing AM pulse is shown for comparison of originally designed optimal waveform from simulation due to repeated nature of the AM waveform over the 200 ns pulse length as seen in Figure 5.13 (b.).

However, the signal generator can only create pulses of 200 ns or greater. Thus, this optimal waveform pulse formed by the generator using these parameters is only a portion of the overall waveform and actually repeats over the entire pulse length (at a rate of 20 MHz). Thus, cutting the signal off after the initial AM pulse is not possible with the simple signal generator equipment available and consequently, a 200 ns pulse will contain approximately 8 of the 'optimum pulses' and generation of a comparable length waveform lasting 50 μs will contain approximately 2000 of the 'optimum pulses' which significantly changes the spectral content of the transmitted waveform and no longer resembles the optimally derived waveform.

Because limitations of the signal generator did not allow for waveforms of such narrow pulse width (the signal generator can only create pulses greater than 200 ns and 20 MHz AM rate relates to a 25 ns pulse), a modified optimum waveform needed to be used in order to properly represent the derived optimum waveform. As previously mentioned, an acceptable modification of the optimal waveform can be achieved by adjusting the length of the target matrix of (1.14) used in the optimal waveform derivation. Thus, a modified optimum waveform was created with the signal generator to match the shape of the optimal waveform derived through simulation while also matching the power levels and length of the uniform pulses that are used for comparison. That is, the spectral information remains constant when deriving optimal waveforms with varying vector lengths. Furthermore, the optimal waveform length is directly determined by the number of columns in the waveform convolution matrix found in (1.14), and consequently, the optimal waveform is approximately a uniform waveform due to its finite length $N$ and will become increasingly narrowband as $N \rightarrow \infty$ [31, 35]. To match

the 50 $\mu$s pulse width of the uniform pulse waveforms, the vector lengths associated with (1.14) were set to appropriate time lengths during the matched illumination design process; however, due to the increased computational burden brought by increasing the matrix size of (1.4), the memory burden became too large for the computer equipment used during this study. Thus, basic parameters associated with the pulse shape and pulse length were approximated and used. The AM rate was set to 10 kHz ($\left(\frac{1}{2}\right)\left(\frac{1}{50\mu s}\right)$ =10 kHz), and the AM depth was set to 100%. Using these parameters for amplitude modulation, the modified optimal waveform generated by the signal generator and output by the amplifier is shown in Figure 5.14 and compared with an equivalent time and energy uniform waveform transmitted at 4 GHz. It is clear that the uniform waveform focuses more energy at the transmitted frequency than the generated optimal waveform and the difference between the signal energy at 4 GHz is 0.9180 dB.

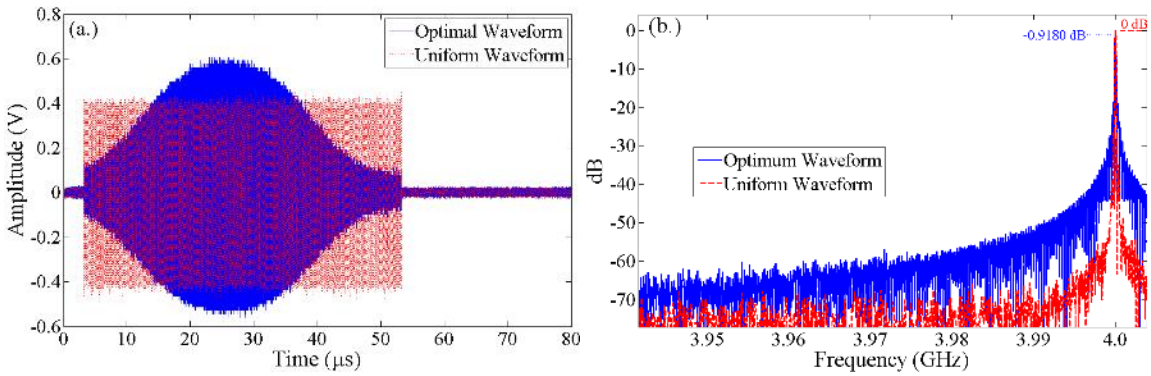


Figure 5.14 Extended duration optimal waveform compared with equivalent energy uniform waveform generated by signal generator and output by amplifier

(a.) Time domain
(b.) Frequency domain

To compare a commonly used radar waveform to the optimal waveforms, a series of LFM waveforms were generated and transmitted for the experiment setup and the resulting SNR was measured. The signal generator's capabilities somewhat limited the wideband LFM waveforms desired because it is only capable of generating LFM waveforms with maximum frequency deviation of 40 MHz between 3 GHz and 4 GHz. At lower frequencies, the maximum frequency deviation possible decreases; thus, the LFM waveforms generated by the signal generator are shown below in Figure 5.15. The generated waveforms are structured very well and have a flat spectrum over the frequencies considered and serve as a good comparison to the optimal waveforms.

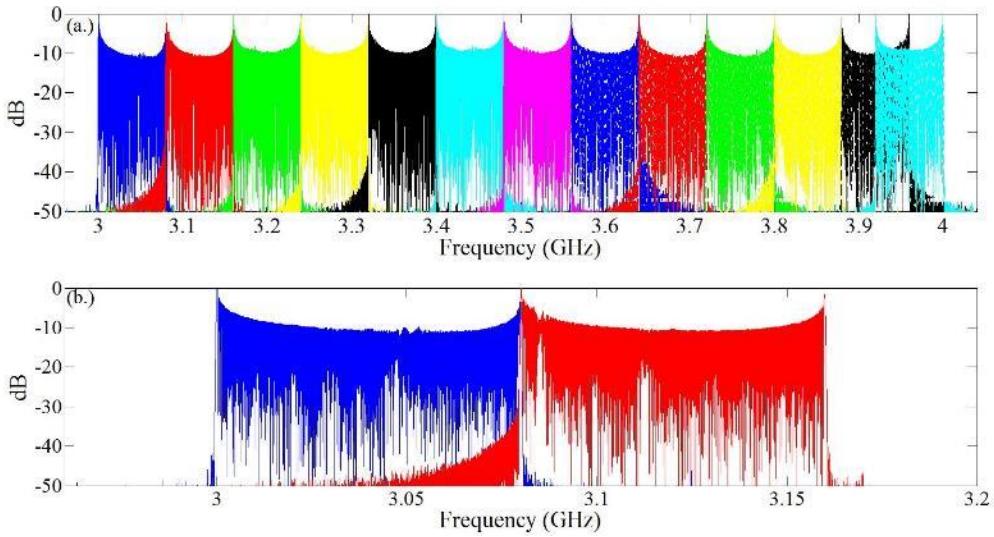


Figure 5.15 LFM waveforms measured at amplifier output

The received power at the antenna for all uniform pulses, LFM pulses, and optimal waveforms transmitted in this experiment were collected and the resulting SNR is shown below in Figure 5.16 and Table 5.2. The resulting SNR of the simulations are

also included for comparison. The simulation results considered the full-wave impulse response of the wall and target setup. The SNR measured at the receiver differs from the simulation results by an absolute mean error of 2.692 dB which shows good agreement between simulated and measured results. The overall shape of the simulation and measured SNR curves are similar, with all sets of data following an increasing slope and better SNR performance at the higher considered frequencies. It is interesting to note that the transmitted optimal waveform appears to perform sub-optimally to the transmitted uniform pulse that was transmitted at same frequency. This could be attributed to error in the transmission of the optimal waveform shape inherent to the signal generator, or it could be that the optimal waveform transmitted was a sub-optimal waveform that was produced through errors in assumptions between the primary-wave and full-wave impulse responses. First, upon inspection of the transmitted waveforms at 4 GHz as previously shown in Figure 5.14, it is clear that the uniform waveform focuses more transmitted energy at 4 GHz whereas the optimal waveform generated slightly spreads its energy around 4 GHz and can most likely explain the sub-optimal performance when compared to the uniform waveforms.

Optimal waveforms were produced for both the primary-wave response and full-wave response and the measured returned power for each waveform further illustrates the accuracy limitations of the primary-wave response. As seen in Figure 5.16 and Table 5.2, the optimal waveform transmitted at 4 GHz returns more power than the optimal waveform transmitted at 3.95 GHz. The uniform waveforms transmitted at both 3.9 and 4 GHz performed better than their respective optimal waveforms, but the returned power for all waveforms matched the shape of the simulated wall and target responses which

show good agreement between simulated and measured results. Again, the uniform waveforms outperforming the optimal waveforms is likely due to the uniform waveforms transmitting more energy at their respective frequencies rather than spreading the energy out, but it is clear that the full-wave transfer function is a better representation of the wall/target scene than the primary-wave transfer function due to the SNR peaks located at 4 GHz. Further inspection of Table 5.2 shows that the measured SNR difference between the optimum and uniform transmission waveforms at 4.0 GHz was 0.762 dB while the transmitted signal energy difference between the two waveforms at 4.0 GHz was 0.9180 dB illustrating a close relationship between the transmitted energy at the single frequency corresponding to the peak of the wall/target transfer function considered (Figure 5.11).

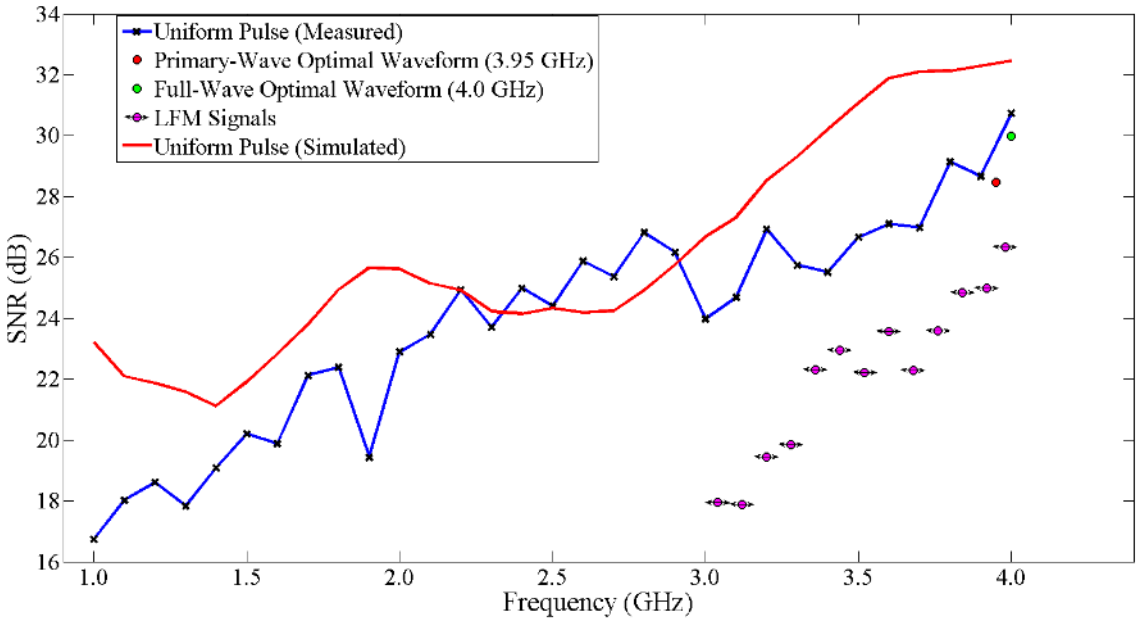


Figure 5.16 Resulting SNR measured for through-wall experiments with face-on aluminum plate target

It is shown that the optimal waveforms outperform the LFM waveforms, which are relatively narrowband given the FM limitations of the signal generator. Furthermore, the SNR improvements of the optimal waveforms would be even greater when compared to LFM waveforms of broader bandwidth. Meanwhile, the primary-wave impulse response has been shown to be sub-optimal (as in simulation); however, compared to transmitting at other frequencies (such as from 1-2 GHz), the matched illumination waveform (shaped as an AM waveform) does provide more signal power back to the receiver. Unfortunately, the AM waveform shape that was inherent to the optimal waveforms considered in this experiment did not perform as well as the uniform pulses and is likely due to the uniform waveforms' characteristic of focusing more signal energy at more narrowbands of the wall/target transfer functions. However, this could be beneficial to the radar designer wishing to use simple, low-cost radar techniques in that it was shown that the performance of the AM waveforms and the uniform pulses performed comparably well. Additionally, it is shown that uniform pulses are clearly a good approximation to the derived optimal waveforms as they actually outperformed all signals during this experiment which considered SNR performance.

Table 5.2 SNR of measured and simulated results for face-on aluminum plate target behind an adobe wall

| **Simulation** | | **Anechoic Chamber Measurements** | | | | | |
|---|---|---|---|---|---|---|---|
| $f$ | $SNR_{CW}$ (dB) | $f$ | $SNR_{CW}$ (dB) | $f_{\min} - f_{\max}$ | $SNR_{LFM}$ (dB) | $f$ | $SNR_{opt}$ (dB) |
| 1.0 | 21.223 | 1.0 | 14.741 | | | | |
| 1.1 | 20.098 | 1.1 | 16.023 | | | | |
| 1.2 | 19.867 | 1.2 | 16.611 | | | | |
| 1.3 | 19.582 | 1.3 | 15.838 | | | | |
| 1.4 | 19.120 | 1.4 | 17.088 | | | | |
| 1.5 | 19.919 | 1.5 | 18.203 | | | | |
| 1.6 | 20.831 | 1.6 | 17.877 | | | | |
| 1.7 | 21.807 | 1.7 | 20.121 | | | | |
| 1.8 | 22.930 | 1.8 | 20.386 | | | | |
| 1.9 | 23.660 | 1.9 | 17.432 | | | | |
| 2.0 | 23.616 | 2.0 | 20.899 | | | | |
| 2.1 | 23.144 | 2.1 | 21.470 | | | | |
| 2.2 | 22.927 | 2.2 | 22.937 | | | | |
| 2.3 | 22.229 | 2.3 | 21.704 | | | | |
| 2.4 | 22.157 | 2.4 | 22.988 | | | | |
| 2.5 | 22.335 | 2.5 | 22.404 | | | | |
| 2.6 | 22.185 | 2.6 | 23.877 | | | | |
| 2.7 | 22.245 | 2.7 | 23.365 | | | | |
| 2.8 | 22.927 | 2.8 | 24.820 | 3.00 - 3.08 | 15.960 | | |
| 2.9 | 23.765 | 2.9 | 24.163 | 3.08 - 3.16 | 15.876 | | |
| 3.0 | 24.678 | 3.0 | 22.978 | 3.16 - 3.24 | 17.440 | | |
| 3.1 | 25.319 | 3.1 | 22.686 | 3.24 - 3.32 | 17.851 | | |
| 3.2 | 26.523 | 3.2 | 24.930 | 3.32 - 3.40 | 20.303 | | |
| 3.3 | 27.327 | 3.3 | 23.748 | 3.40 - 3.48 | 20.947 | | |
| 3.4 | 28.127 | 3.4 | 23.519 | 3.48 - 3.56 | 20.217 | | |
| 3.5 | 29.084 | 3.5 | 24.665 | 3.56 - 3.64 | 21.576 | | |
| 3.6 | 29.882 | 3.6 | 25.105 | 3.64 - 3.72 | 20.290 | | |
| 3.7 | 30.098 | 3.7 | 24.978 | 3.72 - 3.80 | 21.590 | | |
| 3.8 | 30.133 | 3.8 | 27.140 | 3.80 - 3.88 | 22.842 | | |
| 3.9 | 30.294 | 3.9 | 26.670 | 3.88 - 3.96 | 22.997 | 3.95 | 26.47 |
| 4.0 | 30.836 | 4.0 | 28.742 | 3.92 - 4.00 | 24.347 | 4.0 | 27.98 |

#### 5.3.2.2 Results of Edge-on Aluminum Plate Target Arrangement

First, Figure 5.17 is shown to illustrate the simulated transfer functions of the wall, edge-on aluminum plate target, and combined wall/target response along with the resulting matched illumination waveform for the matching simulation setup using the adobe wall model. Clearly, the edge-on plate target features a much different frequency response than the face-on plate target and responds well around frequencies of 1 GHz, 2 GHz, and 3.5 GHz. When the edge-on plate target is located behind the wall, the combined wall/target frequency response actually further increases its response at 2 GHz which will allow a clear illustration of how incorporating the wall response to matched illumination waveform design is crucial to improvement of TWR systems. If only the target were considered, one might believe that energy at either 1GHz, 2 GHz, or 3.5 GHz would result in nearly equal radar performance for through the wall radar systems; however, it is seen in simulation and measurements that the wall/target combination yields a significantly higher response at 2 GHz than at 1GHz. Thus, the arrangement of the edge-on target serves as a good test arrangement for the matched illumination technique.

The measured scattering response of the edge-on aluminum plate target is shown in Figure 5.18 and compared to simulation. Again, for the base comparisons, uniform pulses are transmitted at frequencies from 1GHz to 4 GHz in steps of 0.1 GHz. The measured power returned from the target matches well with the simulated results with only an absolute mean error of 1.8652 dBm. The shape of the measured response over the frequency range also is consistent with the simulated response having nulls around 1.5 GHz and 3 GHz while having peaks near 1 GHz, 2 GHz, and 3.5 GHz.

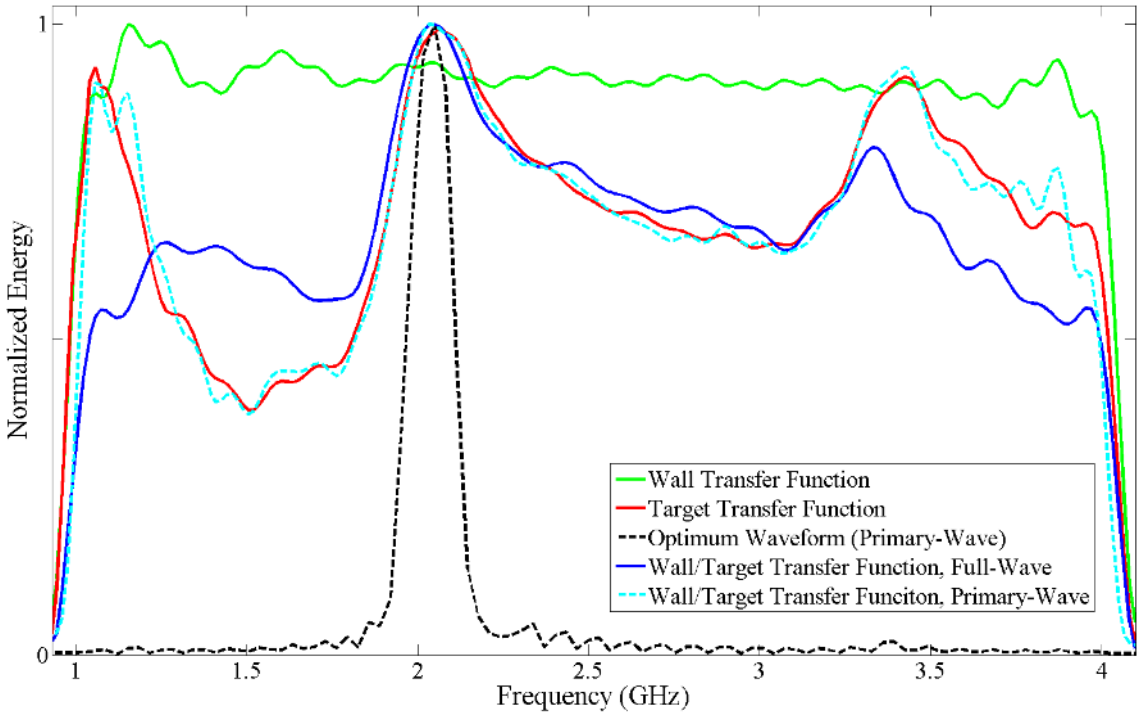


Figure 5.17 Wall and target transfer functions along with the primary-wave and full-wave wall/target transfer functions and derived optimum waveform for adobe wall and edge-on aluminum plate target

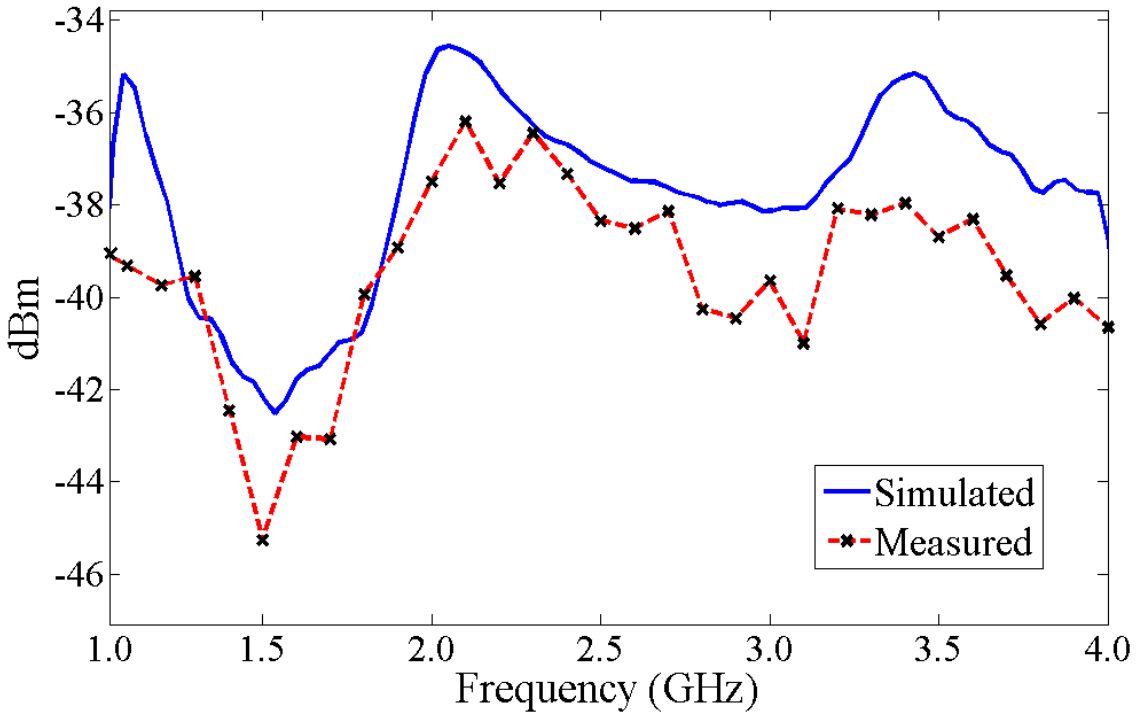


Figure 5.18 Edge-on aluminum plate target response comparison

To compare the through-wall radar scenario, again an optimal waveform is derived using the matched illumination technique and the simulation of the wall and target (edge-on) as before and found to be a single frequency waveform transmitted at 2.05 GHz as seen in Figure 5.17 above. Again, the resulting optimal waveform was formed as a pulse shorter than the signal generator could create; thus, the pulse was generated using the appropriate pulse length and transmission frequency. Similarly shaped AM waveforms were generated at frequencies around 2.05 GHz (1.9 GHz, 2.0 GHz, 2.1 GHz, 2.2 GHz) in order to investigate the accuracy in frequency of the matched illumination derivation. Similarly, LFM waveforms used previously were again tested in addition to more appropriately placed LFM waveforms around the peak of the considered

wall/target setup (around 2 GHz). Again, the signal generator's capabilities are somewhat limited in producing wideband LFM waveforms especially at lower frequencies and for frequencies between 1.5 GHz and 3 GHz, the maximum frequency deviation is 20 MHz. Thus, five additional LFM waveforms are tested for this setup and cover frequencies between 1.90 GHz and 2.10 GHz.

The received power at the antenna for all uniform pulses, LFM pulses, and optimal waveforms transmitted in this experiment were collected and the resulting SNR is shown below in Figure 5.19 and Table 5.3. The resulting SNR of the simulations are also included for comparison. The simulation results considered the full-wave impulse response of the wall and target setup. The SNR measured at the receiver differs from the simulation results by an absolute mean error of 2.7058 dB which again shows good agreement between simulated and measured results. Also, the overall shape of the simulation and measured results are similar with a main peak around 2 GHz. However, for both the uniform and optimal waveforms, the waveforms transmitted at 2.0 GHz performed better than the optimal waveform transmitted at 2.05 GHz which both the full-wave and primary-wave derivation produced. This error could be a product of errors in the measurement or simulation setup; however, the power returned at frequencies around 2GHz are very similar. Interestingly, inspection of the LFM waveforms' performance around 2GHz shows better agreement with the shape of the simulated results as its peak is measured for the LFM waveform over 2.02 - 2.06 GHz.

As with the face-on aluminum plate target, the optimal waveforms transmitted for the edge-on aluminum plate target provided slightly lower SNR performance than the uniform pulses (within 1 dB difference). As previously discussed, the difference is likely

due to the uniform waveform focusing more energy at the transmitted frequency rather than slightly spreading it out around the transmitted frequency as is the case of the generated optimum waveform. The LFM waveforms were again clearly outperformed by the uniform and optimal waveforms transmitted at similar frequencies; however, due to the LFM waveforms around 2 GHz having more narrowband characteristics than the LFM waveforms tested for frequencies between 3-4 GHz, the performance difference between the LFM waveforms and their respective counterparts were not as great around 2 GHz as seen for the face-on aluminum plate target arrangement around 4 GHz.

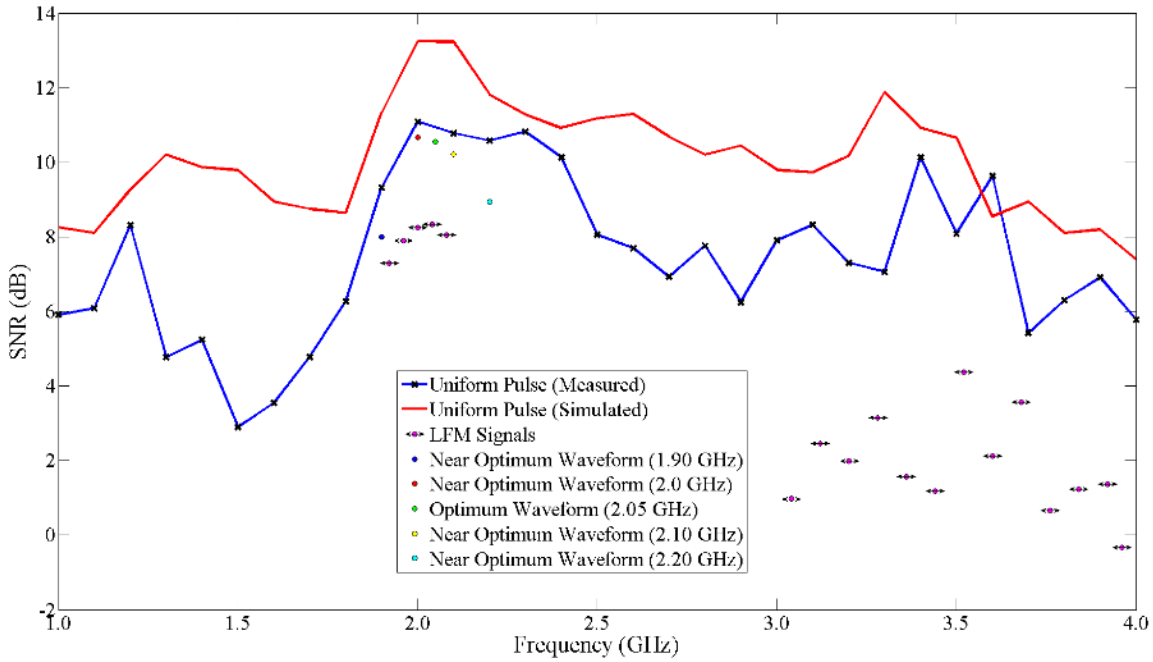


Figure 5.19 Resulting SNR measured for through-wall experiments with edge-on aluminum plate target

Table 5.3 SNR of measured and simulated results for edge-on aluminum plate target behind an adobe wall

| **Simulation** | | **Anechoic Chamber Measurements** | | | | | |
|---|---|---|---|---|---|---|---|
| $f$ | $SNR_{CW}$ (dB) | $f$ | $SNR_{CW}$ (dB) | $f_{\min} - f_{\max}$ | $SNR_{LFM}$ (dB) | $f$ | $SNR_{opt}$ (dB) |
| 1.0 | 8.2607 | 1.0 | 5.9086 | | | | |
| 1.1 | 8.1072 | 1.1 | 6.0842 | | | | |
| 1.2 | 9.2646 | 1.2 | 8.3097 | | | | |
| 1.3 | 10.207 | 1.3 | 4.7731 | | | | |
| 1.4 | 9.8637 | 1.4 | 5.2410 | | | | |
| 1.5 | 9.7927 | 1.5 | 2.8973 | | | | |
| 1.6 | 8.949 | 1.6 | 3.5456 | | | | |
| 1.7 | 8.7460 | 1.7 | 4.7815 | | | | |
| 1.8 | 8.6390 | 1.8 | 6.2763 | | | | |
| 1.9 | 11.330 | 1.9 | 9.3231 | 1.90 – 1.94 | 7.2905 | | |
| 2.0 | 13.238 | 2.0 | 11.086 | 1.94 – 1.98 | 7.9030 | | |
| 2.1 | 13.234 | 2.1 | 10.777 | 1.98 – 2.02 | 8.2562 | | |
| 2.2 | 11.822 | 2.2 | 10.581 | 2.02 – 2.06 | 8.3324 | | |
| 2.3 | 11.279 | 2.3 | 10.819 | 2.06 – 2.10 | 8.0441 | | |
| 2.4 | 10.916 | 2.4 | 10.137 | | | | |
| 2.5 | 11.173 | 2.5 | 8.0563 | | | | |
| 2.6 | 11.289 | 2.6 | 7.6769 | | | | |
| 2.7 | 10.684 | 2.7 | 6.9264 | | | | |
| 2.8 | 10.205 | 2.8 | 7.7618 | 3.00 - 3.08 | 0.9851 | | |
| 2.9 | 10.442 | 2.9 | 6.2436 | 3.08 - 3.16 | 2.4654 | | |
| 3.0 | 9.7938 | 3.0 | 7.9063 | 3.16 - 3.24 | 1.9946 | | |
| 3.1 | 9.7330 | 3.1 | 8.3244 | 3.24 - 3.32 | 3.1461 | | |
| 3.2 | 10.165 | 3.2 | 7.3017 | 3.32 - 3.40 | 1.5639 | | |
| 3.3 | 11.884 | 3.3 | 7.0517 | 3.40 - 3.48 | 1.1846 | | |
| 3.4 | 10.923 | 3.4 | 10.133 | 3.48 - 3.56 | 4.3711 | | |
| 3.5 | 10.656 | 3.5 | 8.0832 | 3.56 - 3.64 | 2.1242 | | |
| 3.6 | 8.5470 | 3.6 | 9.6292 | 3.64 - 3.72 | 3.5735 | 1.90 | 7.9902 |
| 3.7 | 8.9477 | 3.7 | 5.4196 | 3.72 - 3.80 | 0.6583 | 2.00 | 10.665 |
| 3.8 | 8.0993 | 3.8 | 6.2963 | 3.80 - 3.88 | 1.2260 | 2.05 | 10.547 |
| 3.9 | 8.1985 | 3.9 | 6.9143 | 3.88 - 3.96 | 1.3654 | 2.10 | 10.212 |
| 4.0 | 7.3912 | 4.0 | 5.7761 | 3.92 - 4.00 | -0.3282 | 2.20 | 8.9380 |

The resulting radar performance of the matched illumination waveforms as well as the uniform pulses transmitted at narrowband frequencies of 1-4 GHz have illustrated that the matched illumination technique serves TWR well. The measured power received back to the antenna follow the combined transfer functions formed from the simulated impulse response information as seen upon inspection of the SNR across all frequencies considered. This confirms both the usefulness of matched illumination waveform design for TWR but also the accuracy of the adobe wall model created through the dielectric measurements discussed in Chapter 4. With the noise being a near-stationary signal, the resulting SINR (in this case, just SNR) from the anechoic chamber measurements of the adobe wall and aluminum plate targets are shown in Figures 5.16 and 5.19 which follow directly with Figures 5.11 and 5.17, respectively. Consequently, it is clear that the performance of the radar can be significantly increased through matched illumination waveform design.

An important finding shown through simulations and confirmed through the anechoic chamber measurements is that the defining AM shape of the matched illumination waveforms may simply be an artifact of the signal processing used in the derivation. As shown in Figures 5.16 and 5.19 (and Tables 5.2 and 5.3), the SNR of the uniform (single frequency) pulses outperform the derived optimum waveforms. It is inferred that this is due to the more narrowband nature of the uniform waveforms. Below, Figures 5.20 – 5.21 detail the temporal and normalized spectral characteristics of optimum waveforms generated for full-wave impulse response of the face-on aluminum plate target located behind an adobe wall for varying vector lengths $N$ of (1.4). Clearly, the generated optimum waveform of increasing vector length produced a more

narrowband signal; however, the characteristic AM shape of the derived matched illumination waveform is maintained. Following the trend shown, as $N \rightarrow \infty$, the optimum waveform will focus its energy at a single frequency that corresponds to the wall/target transfer function's maximum spectral response.

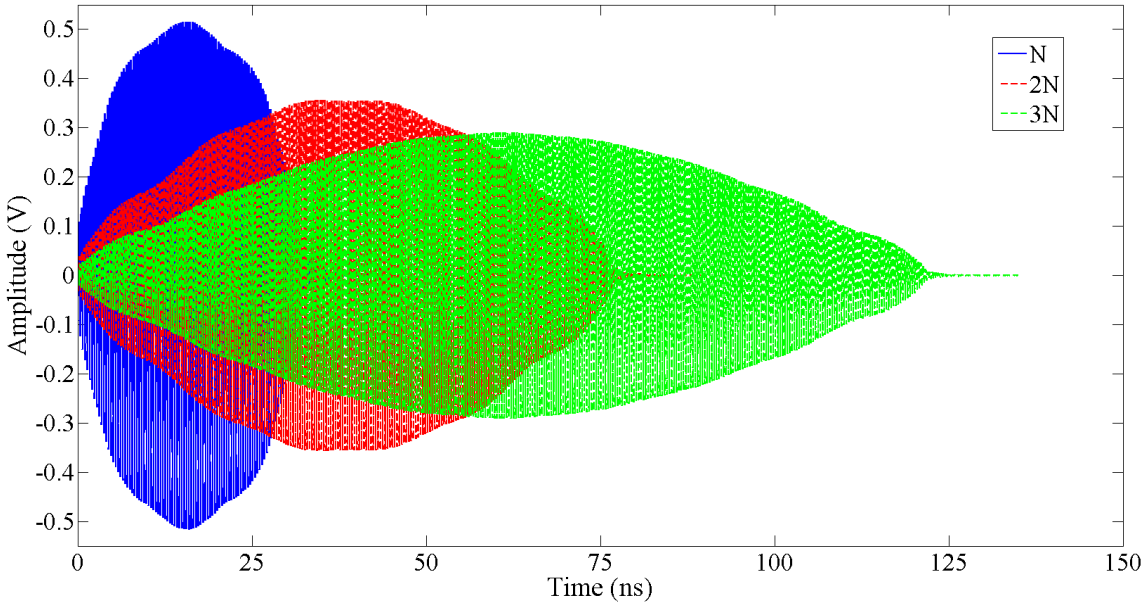


Figure 5.20 Temporal representation of optimum waveforms derived for varying vector length N

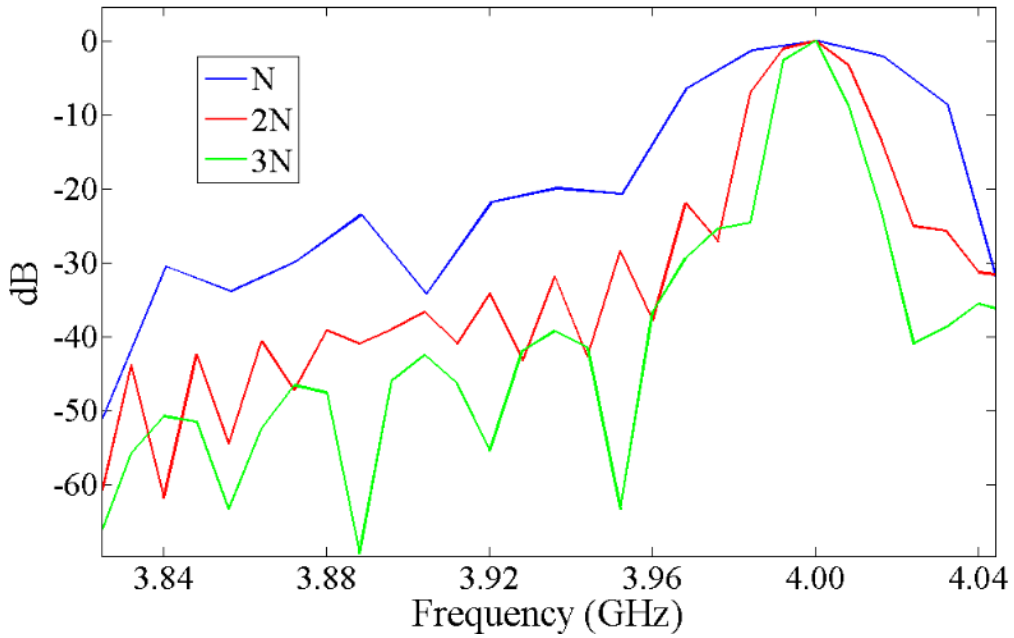


Figure 5.21 Spectral characteristics of optimum waveforms derived for varying vector lengths N

Note that throughout this work, stationary white noise and zero clutter were considered and the wall and target transfer functions contained a clear maximum. Thus, the resulting optimum waveform only contained a single frequency peak rather than multiple significant peaks in the resulting optimum waveform's spectral characteristics. Thus, in the case of a single significant peak in the wall/target transfer function, the true optimum waveform may in fact be a pure sinusoid at the corresponding single frequency of the transfer function's peak, and this principle has been shown in the results of this work. Intuitively, focusing all of the transmission energy at a single point which matches the peak in the wall/target transfer function would yield better radar performance than spreading the energy (however slightly) over an area of the wall/target spectral response.

# CHAPTER VI

# CONCLUSIONS

It has been shown through this work that matched illumination waveform design can enhance the radar performance of TWR systems when accurate wall model information is used in the design process. The wall-target interactions effects in matched illumination waveform design has shown that suboptimal radar performance can occur from assumptions created in the implementation of the simple radar target model. As seen in Chapter 2 and Chapter 5, the waveform designed using the primary-wave impulse response may yield sub-optimal waveforms; however, the flexibility in terms of implementation is great enough to outweigh the sub-optimal performance encountered through the waveform design scheme's inherent assumptions. Additionally, through this work, the impacts resulting from non-uniform moisture profiles have illustrated the need of accurate wall models, and resultantly, accurate wall models have been measured and created for adobe walls and should provide useful information in wall modeling. Finally, the validation of matched illumination waveforms for radar performance enhancement in TWR applications as well as verification of the measured moisture and dielectric properties of an adobe wall have been completed through this work. Original contributions presented in this work follow directly with Chapters 2-5.

In Chapter 2, the accuracy of the matched illumination waveform design scheme was investigated with regards to using primary-wave and full-wave impulse response

information. That is, the impacts of wall-target interaction on matched illumination waveforms for TWR were examined. It was shown that the returns from different wall-target scenarios with varying target sizes, wall-to-target distances, and wall types could be affected through the information that is left out of the primary-wave response which only takes into consideration the target and wall transmission impulse response. The primary-wave wall-target response has been shown to effectively maximize the SINR in through-wall radar applications where wall-target interaction is minor and the primary-wave wall-target transfer function is an accurate representation of the full-wave wall-target transfer function. However, the SINR performance of matched illumination waveforms based on the primary-wave wall-target response can be degraded by relatively minor errors in the wall-target transfer function caused by the incomplete wall-target physics inherent to the scheme. In such cases, the resulting matched illumination waveform spectrum is generally characterized by narrowband energy concentrated at suboptimal frequencies.

In Chapter 3, the impact of the wall's moisture profile on resulting matched illumination waveforms was investigated. Significant differences in the resulting matched illumination waveforms were shown through numerical simulation of representative wall moisture profiles. The different dielectric property profiles demonstrated that the shape of the wall moisture profile can dramatically impact the spectral composition of the resulting optimal waveform. The SINR enhancements shown through simulation illustrate the utility of matched illumination waveforms in TWR applications. Through numerous simulations, it was shown that in general, the wall transmission response sees a fundamental transition in its spectral characteristics at a

conductivity threshold. At conductivities above the threshold, the spectral response of the wall flattens out so that the target scattering response is the main driving force in the design of the optimal waveform.

In Chapter 4, a realistic moisture profile for an adobe wall was determined through measurement. The dielectric properties of the adobe wall material correlating to moisture content were also measured and presented. It was shown that the moisture profile of an adobe wall follows an inverted Gaussian shape or follows an inverted interior moisture profile that was considered in Chapter 2. That is the exterior portions of the wall contain higher amounts of moisture than the interior. It was shown that for the adobe wall considered, the relative permittivity could range from $1.5 \leq \varepsilon_r \leq 6.5$ while the electrical conductivity could range from $0 \leq \sigma \leq 0.25$ S/m for a given moisture content level.

In Chapter 5, the measurements performed on the adobe wall were validated, as well as the verification that the matched illumination waveforms provide radar performance increases (increased SINR). Through measurement in an anechoic chamber, an adobe wall was also evaluated in terms of attenuation and compared to calculations using the measured dielectric properties. It was found that for a 0.18 cm thick adobe wall, roughly 11 dB attenuation of the radar signal can be expected for one way propagation. The TWR enhancement provided by matched illumination waveform design was also confirmed by the amount of signal energy received at frequencies exhibiting good responses in the combined wall transmission and target transfer functions. While the matched illumination waveform did not outperform the uniform pulses in this study, it was shown that the AM shape inherent to the derived optimum

waveforms is likely a result of the signal processing required, and resultantly uniform waveforms transmitted at a single frequency corresponding to the wall/target transfer function peak yield the best radar performance increase. Additionally, the use of linear regression models in modeling the adobe wall for simulation shown to be an accurate method of adobe wall modeling given accurate moisture/dielectric property measurements as the measured and simulated data showed good correlation.

In conclusion, it has been shown that the matched illumination technique serves TWR applications well; however, it critically depends on the *a priori* information of the target and wall impulse responses. The wall's moisture profile must be accurately modeled and incorporated into the waveform design scheme because it has a significant impact on radar performance. Having the moisture profile information and correlating dielectric properties of realistic, commonly encountered walls, better *a priori* information can be given to TWR applications; consequently, the matched illumination waveform technique can be used to enhance radar performance for these applications. The measurement of a realistic moisture profile can also be used in modeling walls of similar composition and make-up as the existence of heterogeneous moisture profiles are likely.

REFERENCES

[1] Mark Farwell, Jennifer Ross, Richard Luttrell, Douglas Cohen, Wilbur Chin, and Traian Dogaru, "Sense through the wall system development and design considerations," Journal of the Franklin Institute, Vol. 345, no. 6, pp. 570-591, Sept. 2008.

[2] E. Baranoski, "Through-wall sensing; radar signal processing; model-based reasoning; Propagation effects," *J. Franklin Inst.—Special Issue on "Advances in Indoor Radar Imaging"*, vol. 345, no. 6, pp. 556–569, Sep. 2008.

[3] P.Withington, H. Fluhler, and S. Nag, "Enhancing homeland security with advanced UWB sensors," *IEEE Microw. Mag.*, vol. 4, no. 3, pp. 51–58, Sep. 2003.

[4] D.D. Ferris Jr., N.C. Currie, "A survey of current technologies for through-the-wall surveillance (TWS)," in *SPIE Conference on Sensors and Technologies for Law Enforcement*, vol. 3577, Boston, MA, pp 62–72, Nov. 1998.

[5] E.A. Robinson, S. Treitel, *Geophysical Signal Analysis*, Prentice-Hall, Englewood Cliffs, NJ, 1980.

[6] A.C. Kak, M. Slaney, *Principles of Computerized Tomographic Imaging*, IEEE Press, New York, 1988.

[7] Borek, S.E., "An overview of through the wall surveillance for homeland security," in: *Proceedings of the 34th, Applied Imagery and Pattern Recognition Workshop*, vol. 6, pp. 19–21, Oct. 2005.

[8] D.D. Ferris Jr., N.C. Currie, "Microwave and millimeter wave systems for wall penetration," in *Proceedings of SPIE–Vol. 3375, Targets and Backgrounds: Characterization and Representation IV*, pp. 269–279, July 1998.

[9] L.M. Frazier, "Surveillance through walls and other opaque materials," *Proc. IEEE Natl. Radar Conf. Electron. Syst.*, pp. 27–31, 1996.

[10] L.M. Frazier, "Motion detection radar (MDR) for law enforcement," *IEEE Potentials 16* (5) (2004) 3079–3082.

[11] S. Nag, M.A. Barnes, T. Payment., G. Holladay, "An ultra-wideband through-the-wall radar for detecting the motion of people in real time," *Proc. SPIE: Radar Sensor Technol. Data Visualization 4744*, pp.48–57, Nov. 1998.

[12] R.J. Fontana," Recent system applications of short-pulse ultra-wideband (UWB) technology," *IEEE Trans. Microwave Theory Tech*. Vol. 52 no.9, 2004.

[13] D.G. Falconer, R.W. Ficklin, K.G. Konolige, "Robot-mounted through-wall radar for detecting, locating, and identifying building occupants," *Proc. IEEE Int. Conf. Robot. Automat. 2*, pp. 1868–1875, 2002.

[14] F. Ahmad, M.G. Amin, P. Setlur, "Through-the-wall target localization using dual-frequency CW radars," in *Proceedings of SPIE Symposium on Defense and Security Conference*, vol. 6201, Orlando, FL, April 2006.

[15] M. Amin, P. Zemany, P. Setlur, F. Ahmad," Moving target localization for indoor imaging using dual frequency CW radars," in *Proceedings of the Fourth IEEE Workshop on Sensor Array and Multi-Channel Processing*, Waltham, MA, July 2006, pp. 367–371.

[16] F. Ahmad, M.G. Amin, P.D. Zemany, "Performance analysis of dual-frequency CW radars for motion detection and ranging in urban sensing applications," in *Proceedings of SPIE Symposium on Defense and Security, Radar Sensor Technology XI Conference*, vol. 6547, Orlando, FL, April 2007.

[17] P. Setlur, F. Ahmad, M.G. Amin, P.D. Zemany, "Experiments on through-the-wall motion detection and ranging," in *Proceedings of SPIE Symposium on Defense and Security VI Conference*, vol. 6538, Orlando, FL, April 2007.

[18] P. Setlur, M. Amin, F. Ahmad, Cramer-Rao, "Bounds for range and motion parameter estimations using dual frequency radars," in *Proceedings of IEEE International Conference on Acoustics, Speech, and Signal Processing*, vol. 3, Honolulu, HI, April 2007, pp. 813–816.

[19] T. Thayaparan, et al., "Micro-doppler human signature detection and its application to gait Recognition and indoor imaging," *J. Franklin Inst.,* 2008.

[20] S. Sundar, et al., "Doppler-based detection and tracking of humans in indoor environments," *J. Franklin Inst.* (2008).

[21] E.F. Greneker III, "RADAR flashlight for through-the-wall detection of humans," *Proc. SPIE Targets Backgrounds: Charact. Representation IV 3375* pp. 280–285, 1998.

[22] F. Ahmad, M.G. Amin, S.A. Kassan, "Synthetic aperture beamformer for imaging through a dielectric wall," *IEEE Trans. Aerosp. Electron. Syst*. 41,pp. 263–271, 2005.

[23]F. Ahmad, M.G. Amin, G. Mandapati, "Autofocusing of through-the-wall radar imagery under unknown wall characteristics," *IEEE Trans. Image Process.*, Vol. 16 no. 7, pp. 1785–1795, 2005.

[24] F. Aryanfar, K. Sarabandi, “Through wall imaging at microwave frequencies using space-time focusing,” *Antennas Propag. Soc. Int. Symp.*, pp.3063–3066, 2004.

[25] Ahmad, F., Amin, M.G., and Mandapati, G., “Autofocusing of through-the-wall radar imagery under unknown wall characteristics,” *IEEE Trans. Image Process.* Vol. 16, no. 7, pp. 1785–1795, 2007.

[26] Ahmad, F.; Amin, M. G., “Noncoherent Approach to Through-the-Wall Radar Localization,” *IEEE Transactions on Aerospace and Electronic Systems,* Vol. 42, no. 4 ,pp. 1405-1419, 2006.

[27] Ahmad, F. and Amin, M. G., “Performance of autofocusing schemes for single target and populated scenes behind unknown walls,” In *Proceedings of SPIE - Radar Sensor Technology XI*, vol. 6547, Orlando, FL, April, 2007.

[28] Mandapati, G. and M. Amin, “Blurness and focusing-defocusing for through the wall radar imaging with wall ambiguities," *IEEE International Symposium on Signal Processing and Information Technology*, pp. 246-249, 2004.

[29] Y. Jia*, L. J. Kong, and X. B. Yang, “A Novel Approach to Target Localization Through Unknown Walls For Through-The_Wall Radar Imaging,” *Progress in Electromgnetics Research,* Vol. 119, pp. 107-132, 2011.

[30] Ahmad, F.; Amin, M.G.; Kassam, S.A., "Synthetic aperture beamformer for imaging through a dielectric wall," *Aerospace and Electronic Systems, IEEE Transactions on* , vol.41, no.1, pp.271,283, Jan. 2005

[31] H. Estephan, M. Amin, and K. Yemelyanov, "Optimal Waveform Design for Improved Indoor Target Detection in Sensing Through-the-Wall Applications,' *IEEE Trans. Geosci. Remote Sens*., vol. 48, no. 7, pp. 2930-2941, July 2010.

[32] F. Ahmad and M. Amin, “Optimal waveform design for through-thewall radar imaging,” in *Proc. SPIE Symp. Defense, Security, Sens., Radar Sensor Technol. XIII Conf.*, Orlando, FL, Apr. 2009.

[33] H. Estephan, M. Amin, K. Yemelyanov, and A. Hoorfar, “Waveform design for through-the-wall radar imaging applications,” in *Proc. SPIE Symp. Defense Security, (C3I)*, Orlando, FL, Mar. 2008, vol. 6943, pp. 694.

[34] F. Ahmad, M. Amin, “Matched-Illumination Waveform Design for a Multistatic Through-the-Wall Radar System”, *IEEE Journal of Selcted topics in Signal Processing*, vol 4, no. 1, Feb. 2010.

[35] D. A. Garren, A. C. Odom,M. K. Osborn, J. S. Goldstein, S. U. Pillai, and J. R. Guerci, “Enhanced target detection and identification via optimized radar transmission pulse shape,” *Proc. Inst. Elect. Eng.—Radar, Sonar Navig.*, vol. 148, no. 3, pp. 130–138, Jun. 2001.

[36] D. A. Garren, A. C. Odom,M. K. Osborn, J. S. Goldstein, S. U. Pillai, and J. R. Guerci, “Full-polarization matched-illumination for target detection and identification,” *IEEE Trans. Aerosp. Electron. Syst.*, vol. 38, no. 3, pp. 824–837, Jul. 2002.

[37] L. S. Riggs, M. A. Richards, T. H. Shumpert, and C. R. Smith, “On waveform design for optimal target discrimination,” *Int. J. Imaging Syst. Technol.*, vol. 4, no. 4, pp. 327–335, 1992.

[38] S. Blunt and P. Yantham, “Waveform design for radar-embedded communications,” in *Proc. Int. Waveform Diversity Des. Conf.*, Pisa, Italy, Jun. 2008, pp. 214–218.

[39] G. Frazer, B. Johnson, and Y. Abramovich, “Orthogonal waveform support in MIMO HF OTH radars,” in *Proc. Int. Waveform Diversity Des. Conf.*, Pisa, Italy, Jun. 2008, pp. 423–427.

[40] S. U. Pillai, H. S. Oh, D. C. Youla, and J. R. Guerci, “Optimum transmit receiver design in the presence of signal-dependent interference and channel noise,” *IEEE Trans. Inf. Theory*, vol. 46, no. 2, pp. 577–584, Mar. 2000.

[41] Romero, R.A.; Junhyeong Bae; Goodman, N.A., "Theory and Application of SNR and Mutual Information Matched Illumination Waveforms," *Aerospace and Electronic Systems, IEEE Transactions on*, vol.47, no.2, pp.912-927, April 2011.

[42] S. Kay, “Optimal signal design for detection of Gaussian point targets in stationary Gaussian clutter/reverberation,” *IEEE J. Sel. Topics Signal Process.*, vol. 1, no. 1, pp. 31–41, Jun. 2007.

[43] Y. Yang and R. Blum, “Waveform design for MIMO radar based on mutual information and minimum mean-square error estimation,” in *Proc. 40th Annu. Conf. Inf. Sci. Syst.*, Mar. 2006, pp. 111–116.

[44] F. Ahmad, M. Amin, “Radar Waveform Design for Detection of Weapons,” *Proc. SPIE – Radar Sensor Technology XIV*, 2010.

[45] F. Dai, H. Liu, “Matched Illumination Waveforms Design for Range-spread Target in Heterogeneous Clutter plus Noise,” *IEEE CIE International Conference on Radar*, 2011.

[46] Soldani, F.; Alabaster, C.M., "The benefits of matched illumination for radar detection of ground based targets," *Waveform Diversity and Design Conference, 2007. International* , vol., no., pp.23,27, 4-8 June 2007.

[47] R. Wilson, “Propagation Losses Through Common Building Materials,” *Report for Magis Networks, Inc*. 2002.

[48] S. Kim, B. Bougerolles, and H. L. Bertoni, "Transmission and Reflection Properties of Interior Walls, " *Proc. IEEE ICUPC'94*, p. 124-128, 1994.

[49] J. F. Lafortune and M. Lecours, "Measurement and Modeling of Propagation Losses in a Building at 900 MHz," *IEEE Trans Veh. Technol.,* vol. 39, pp. 101-108, 1990.

[49] U. Halabe, A. Sotoodehnia, K. Maser, and E. Kausel, "Modeling the Electrogmagnetic Properties of Concrete," *ACI Materials Journal* Title no. 09-M55, Dec. 1993, pp. 552-563.

[50] A. Ogunsola, U. Reggiani, and L. Sandrolini, " Modelling shielding properties of concrete," *17th International Zurich Symposium on Electromagnetic Compatibility*, pp. 34-37 ,2006.

[51] A. Robert, "Dielectric permittivity of concrete between 50 Mhz and 1 Ghz and GPR measurements for building materials evaluation," *Journal of Applied Geophysics 40*, pp. 89-94. 1998.

[52] U. Halabe, K. Maser, E. Kausel, "Propagation characteristics of Electromagnetic Waves in Concrete," *Technical Report for U.S. Army Research Office*. Jan 1988.

[53] E. Rirsch, Z. Zhang, "Rising Damp in Masonry Walls and the Importance of Mortar Properties," *Construction and Builiding Material 24*, pp. 1815-1820, 2010.

[54] S. Hong, K. Kim, and J. Lee, "Moisture Effects on the Penetration Loss through Exterior Building Walls*," IEEE VTC*, 1998.

[55] D. Pena, R. Feick, et. al., "Measurement and Modeling of Propagation Losses in Brick and Concrete Walls for the 900-MHz Band" *IEEE Trans on Antennas and Propagation*, vol 51. No. 1 Jan 2003.

[56] Pidanic, J.; Cermak, D.; Schejbal, V., "Through-wall propagation measurements," *Applied Electromagnetics and Communications, 2007. ICECom 2007. 19th International Conference on* , vol., no., pp.1,4, 24-26 Sept. 2007.

[57] W. Stone, "Electromagnetic Signal Attenuation in Construction Materials," *NIST Construction Automation Program Report No. 3*, Oct. 1997.

[58] A. Muqaibel, A. Safaai-Jazi, et. al., "Ultrawideband through-the-wall propagation," *IEE Proc.-Microw. Antennas Propag*., Vol. 152, No. 6, pp.581-588 Dec 2005.

[59] S.D. Beyea, B.J. Balcom, et. al., " Magnetic Resonance Imaging and Moisture Content Profiles of Drying Concrete," *Cement and Concrete Research*,Vol. 28, No. 3. Pp. 456-463, 1998.

[60] C. Thajudeen, A. Hoorfar, et. al., " Measured Complex Permittivity of Walls with Different Hydration Levels and the Effect of Power Estimation of TWRI Target Returns*," Progress in Electromagnetics Research B*, Vol. 30, pp 177-199. 2011.

[61] F. Menke, R. Knochel, et. al., "Moisture Measurement in Walls using Microwaves," *IEEE MTT-S Digest*, 1995.

[62] R.A. Huizinga, "Assessment on the moisture content in the brick walls of the Church in Bergeijk with the use of a microwave meter," Master project [online], Feb 2012.

[63] M.A. Richards, *Fundamentals of Radar Signal Processing*, 1st ed.,2005.

[64] Romero, R.; Goodman, N.A., "Information-theoretic matched waveform in signal dependent interference," *Radar Conference, 2008. RADAR '08. IEEE* , vol., no., pp.1,6, 26-30 May 2008.

[65] E. J. Rothwell and W. Sun, "Time domain deconvolution of transient radar data," *IEEE Trans. Antennas Propag.*, vol. 38, no. 4, pp. 470–475, Apr. 1990.

[66] B. R. Hunt, "A theorem *on* the difficulty of numerical deconvolution," *IEEE Trans. Audio Electroacoust.,* vol. AU-20, pp. 94-95, Mar. 1972.

[67] B. Drachman, "Two methods to deconvolve: LI-method using simplex algorithm and L2-method using least squares and a parameter," *IEEE* Trans. *Antennas Propagat.,* vol. AP-32, pp. 219-225, Mar. 1984.

[68] T. Sarkar, F. Tseng, et. al., "Deconvolution of Impulse Response From Time-Limited Input and Output: Theory and Experiment," *IEEE Trans. On instrumentation and measurement*, vol. IM-34, No. 4. Dec. 1985.

[69] N. Goodman, P. Venkata, and M. Neifeld, "Adaptive Waveform Design and Sequential Hypothesis Testing for Target Recognition with Active Sensors, *IEEE J. Sel. Topics in Sig. Proc. Mag.*, vol. 1, no. 1, pp. 105-113, Jun. 2007.

[70] M. R. Bell, "Information theory and radar waveform design, *IEEE Trans. Inform. Theory*, vol. 39, no. 5, pp. 1578-1597, Sep. 1993.

[71] J. Rovnakova, D. Kocur, "Application of Estimated Wall Parameters for Through-Wall Target Tracking*, 22nd International Conference Radioelectronika,* 2012.

[72] Protiva, P.; Mrkvica, J.; Machac, J., "Estimation of Wall Parameters From Time-Delay-Only Through-Wall Radar Measurements," *Antennas and Propagation, IEEE Transactions on* , vol.59, no.11, p.4268,4278, Nov. 2011.

[73] Shahid, A.; Ghafoor, A.; Riaz, M.M., "Wall parameter estimation using propagation time delay," *Radar Conference 2013, IET International* , pp.1,6, 14-16 April 2013.

[74] Protiva, P.; Mrkvica, J.; Safarik, M.; Sikl, R.; Vlasak, V.; Machac, J., "An improved technique for estimating wall parameters from time-delay through-wall radar measurements," *Radioelektronika (RADIOELEKTRONIKA), 2012 22nd International Conference* , pp.1,4, 17-18 April 2012.

[75] S. Price, J. P. Donohoe, and J. Fairley, "The Effects of Wall Moisture Profiles on Matched Illumination Waveforms ," presented at the IEEE AP-S/USNC-URSI Symposium, Orlando, FL, 2013.

[76] H. Kaariainen, M Rudolph, et. al., "Moisture measurements in building materials with microwaves," *NDT&E International 34*, pp. 389-394, 2001.

[77] Ch. Maierhofe, J. Wostmann, "Investigation of dielectric properties of brick materials as a function of moisture and salt content using a microwave impulse technique at very high frequencies," *NDT&E International*, Vol. 31, No. 4, pp. 259-263, 1998.

[78] M.N. Soutsos, J.H. Bungey, et. al., "Dielectric properties of concrete and their influence on radar testing," *NDT&E International 34*, pp. 419-425, 2001.

[79] K. Ling-jiang, G. Cui, et. al., "Wall parameters estimation method for through-the-wall radar imaging," *2008 International Conference on Radar*, pp. 297-301, Sept. 2008.

[80] F. Sandrolini, E. Franzoni, "An operative protocol for reliable measurements of moisture in porous materials of ancient buildings," *Building and Environment 41*, pp. 1372-1380, 2006.

[81] T. Hauschild, F. Menke, "Moisture measurement in masonry walls using a non-invasive reflectometer, "*IEE Electronic Letters Online,* No. 19981659, Oct. 1998.

[82] Z.M. Sbartai, S. Laurens, et. al., "Non-destructive evaluation of concrete physical condition using radar and artificial neural networks," *Construction and Building Materials 23*, pp. 837-845, 2009.

[83] E.H. Waters, "Measurement of moisture in concrete and masonry with special reference to neutron scattering techniques," *Nuclear Structural Engineering*, Volume 2, Issue 5, pp. 494-500, Dec. 1965.

[84] Pel L, Kopinga K, Brocken H. "Determination of moisture profiles in porous building materials by NMR," *Magnetic Resonance Imaging*, 1996.

[85] Pel L, Huinink HP, Kopinga K, Rijniers LA, Kaasschieter EF., "Ion transport in porous media studied by NMR," *Magnetic Resonance Imaging*, pp. 549–550, 2001.

[86] I.R.Capoglu. (2015). *Angora 0.20.0* [Onlines]. Available: http://www.angorafdtd.org

[87] S.Price, J.P. Donhoe, J. Fairley, "Effects of Wall Moisture Profiles on Matched Illumination Waveforms - Simulation and Measurement," in *Proc. of the 2014 IEEE Radar Conference*, May 2014.

[88] S.R. Price, J.P. Donohoe, J. Fairley, "Impacts of Wall-Target Interaction on Matched Illumination Waveforms for TWRI," *IEEE Geoscience and Remote Sensing Letters*, Volume 12, Issue 7, 2015.

[89] T. Jin, B Chen, and Z. Zhou, "Image-Domain Estimation of Wall Parameters for Autofocusing of Through-the-Wall SAR Imagery," *IEEE Trans. Geosci. Remote Sens*., vol. 51, no. 3, pp. 1836-1843, Mar. 2013.

[90] M. Aftanas, J. Rovnakova, et. al., "Efficient Method of TOA Estimation for Through Wall Imaging by UWB Radar," *IEEE International Conference on Ultra-Wideband, ICUWB 2008*, vol. 2, pp. 101-104, Sept. 2008.

[91] R. Souma, S. Kidera, and T. Kirimoto, "Accurate Permittivity Estimation Method by Compensating Waveform Deformation for UWB Internal Imaging Radar," *IEEE International Conference on Ultra-Wideband, ICUWB 2012*, pp. 496-500, Sept. 2012.

[92] F. Sandrolini, E. Franzoni, "An operative protocol for reliable measurements of moisture in porous materials of ancient buildings," Building and Environment 41, pp. 1372-1380, 2006.

[93] A. Yahalom, Y. Pinhasi, et. al., "Transmission through Single and Multiple Layers in the 3-10 GHz Band and the Implications for Communications of Frequency Varying Material Dielectric Constants," *WSEAS Trans. on Communications*, Vol. 9, Issue 12, pp. 759-772, Dec. 2010.

[94] D.A Reckhow, "Chapter XV: Gravimetric Methods," [Online]. Available: www.ecs.umass.edu/cee/reckhow/courses/572/572bk15/572BK15.html

[95] Technical Overview, "Agilent 805070E Dielectric Probe Kit 200 MHz to 50 GHz." [Online]. Available: http://literature.cdn.keysight.com/litweb/pdf/5989-0222EN.pdf

[96] User Manual, "Model 3160 Series - Pyramidal Horn Antenna," ETS-Lindgren Inc., (July 2014). [Online]. Available: http://ets-lindgren.com/manuals/3160.pdf

[97] Rahman, Jahangir, et al., "Deconvolution and Total Least Squares in Finding the Impulse Response of an Electromagnetic System from Measured Data," *IEEE Transactions on Antennas and Propagation*, Vol. 43, No. 4, April 1995.

[98] *Antenna Measurement Theory*, ORBIT/FR Inc. [Online]. Available: http://www.keysight.com/upload/cmc_upload/All/ORFR-Theory.pdf?&cc=US&lc=eng

[99] Nikolova, Natalia, (2014). *Basic Methods in Antenna Measurements* [Online]. Available:http://www.ece.mcmaster.ca/faculty/nikolova/antenna_dload/current_lectures/L08_Measure.pdf

[100] Balanis, Constantine, "Antenna Theory: Analysis and Design," 3rd ed. Wiley-Interscience, 2005.

[101] H.T. Friis, "A Note on a Simple Transmission Formula*," Proceedings of the IRE, Vol. 34, May 1946, p. 254.

[102] Equipment Overview, "AECT 3500 Series Compressed Earth Block Machine." [Online]. Available: http://aectearthblock.com/3500series.html

[103] Controlled Environment Chamber, "Model 5503-00 & 5503-11." [Online]. Available: http://www.electrotechsystems.com/manuals/1-%20PDF%20Environmental%20Control%20Manuals/Chambers/5503%20Manual%20Pkg%20A,B%20Rev0%201-07.pdf

[104] Equipment Datasheet, "Double Ridge Horn Antenna – AH-118." [Online]. Available: http://www.com-power.com/datasheets/AH-118.pdf

# APPENDIX A

# TECHNIQUES FOR ACCRUATE DECONVOLUTION

In this Appendix, techniques useful in the determination of an impulse response via deconvolution are discussed because of the importance to the matched illumination waveform design. Throughout this work, all techniques described were used and compared against one another to determine the most accurate impulse response information.

The determination of the impulse response is complicated by the presence of an ill conditioned matrix in the deconvolution process. To get the impulse response $\boldsymbol{q}$ of a scattered target echo $\boldsymbol{s}$, the incident waveform $\boldsymbol{z}$ must be put into a deconvolution matrix $\boldsymbol{Z}$ because we know that the convolution of the incident waveform with the impulse response will yield the scattered field (i.e., $\boldsymbol{z} * \boldsymbol{q} = \boldsymbol{s}$). Thus, to find $\boldsymbol{q}$ given $\boldsymbol{z}$ and $\boldsymbol{s}$, we must reverse the convolution. In matrix-vector form, the convolution would be accomplished by forming the incident waveform ($\boldsymbol{z} = [z_1, z_2, \dots, z_N]^T$) into a convolution matrix $\boldsymbol{Z}$ as:

$$\mathbf{Z} = \begin{bmatrix} z_1 & 0 & 0 & \cdots & 0 \\ z_2 & z_1 & 0 & \cdots & 0 \\ \vdots & z_2 & z_1 & \ddots & \vdots \\ z_{N-1} & \vdots & \vdots & \ddots & 0 \\ z_N & z_{N-1} & \cdots & z_2 & z_1 \end{bmatrix} \tag{A.1}$$

Then, through convolution, the scattered field is simply $\boldsymbol{s} = \boldsymbol{Z}\boldsymbol{q}$. Thus, to deconvolve the incident waveform from the scattered field, the inverse is undertaken such that

$$\boldsymbol{q} = \boldsymbol{Z}^{-1}\boldsymbol{s}. \tag{A.2}$$

It has been shown and is well known that (A.2) is a highly instable solution due to small values in the deconvolution matrix $\boldsymbol{Z}^{-1}$ [65]. To overcome this issue, a frequency domain approach, a singular value decomposition technique, and a least square error solution can be used.

## A.1 Frequency Domain Approach

The simplest technique used to find the solution to the deconvolution problem is provided by making calculations in the frequency domain. If we transform the convolution into the time domain, the calculation is a simple multiplication. That is,

$$\boldsymbol{s} = \boldsymbol{z} * \boldsymbol{q} \overset{\boldsymbol{DFT}}{\Longleftrightarrow} S(j\omega) = Z(j\omega) \times Q(j\omega). \tag{A.3}$$

The deconvolution can now be written as

$$Q(j\omega) = \frac{S(j\omega)}{Z(j\omega)} \tag{A.4}$$

However, this approach is severely susceptible to error. The error that arises in this approach stems from having small values (near-zero) in the denominator of the calculation. Additionally, aliasing can occur if the sampling is not taken into account when transforming the data because the signals are not band-limited.

## A.2 Singular Value Decomposition (SVD) Technique

To overcome the shortcomings of the frequency domain approach, [65] used a singular value decomposition technique which follows. Let the incident waveform matrix $\boldsymbol{Z}$ be decomposed using SVD as

$$\boldsymbol{Z} = \boldsymbol{U}\Sigma\boldsymbol{V}^T \tag{A.5}$$

where $\boldsymbol{U}$ and $\boldsymbol{V}$ are $N \times N$ orthogonal matrices and $\Sigma$ is an $N \times N$ diagonal matrix whose diagonal entries are the singular values of $\boldsymbol{Z}$. The solution of (A.2) can be written as

$$\boldsymbol{q} = \boldsymbol{V}\eta \tag{A.6}$$

where $\eta$ is a vector with the entries

$$\eta = \frac{(\boldsymbol{U}^T\boldsymbol{s})_i}{\sigma_i}. \tag{A.7}$$

In (A.7), $\sigma_i$ are the entries of the matrix $(\Sigma)_{ii} = \sigma_i, \sigma_i \geq \sigma_{i+1}$. If $\boldsymbol{Z}$ is ill-conditioned, its singular values will cause $\eta$ to be large, emphasizing the contribution of $\boldsymbol{q}$. It is also suggested in [65] that simply disregarding small singular values ($\sigma_i \sim 0$) and replacing the corresponding $\eta_i$ with 0 results in the solution of least norm which is equivalent to discarding columns of $\boldsymbol{V}$ which cannot be excited by $\boldsymbol{Z}$.

### A.3 Least Square Error Solution

The least square solution is another approach which simply follows the least squares solutions found in [97]. That is,

$$\boldsymbol{q} = (\boldsymbol{Z}^T\boldsymbol{Z})^{-1}\boldsymbol{Z}^T\boldsymbol{s}. \tag{A.8}$$

This is easily implemented in MATLAB using the function $lsqr$ or by noting that $(\boldsymbol{Z}^T\boldsymbol{Z})^{-1}\boldsymbol{Z}^T$ is the pseudo-inverse of $\boldsymbol{Z}$.

By comparing all three approaches, an accurate impulse response can be found and used for derivation of matched illumination waveforms for a given target and wall transmission impulse response.

# APPENDIX B

# ENSURING PLANE WAVE BEHAVIOR OVER ILLUMINATION AREA

In this Appendix, plane wave conditions are discussed as well as the work done to ensure plane wave behavior was met for the illumination area upon the adobe wall test article. Because the FDTD simulations assume plane waves incident upon the wall and target model, it is critical to the comparisons that the wavefronts in the anechoic chamber are planar as well. It is also essential that the wall, target, and receive antenna are located in the far field of the transmitting antenna because the gain parameters used in the calculations assume far field conditions.

## B.1 Plane Wave Conditions

The far-field of an antenna is a condition that is met when the wave front of the transmitted waveform can be considered to have constant field vectors over some area of consideration. For example, the area of consideration in this work is the receive antenna's aperture as well as the illumination area of the wall and target. That is, the wall and target should experience an incident wave front with constant field vectors over the entire area of the wall and target.

In practice, antennas generate far fields in 3-D space which are closely approximated by spherical wave fronts. As the distance from the transmit antenna increases, the curvature of the wave front at the area of consideration decreases and can be considered planar. Thus, the transmitted wave can be well approximated by a plane wave at sufficiently large distances. Below, Figure B.1 illustrates a simple demonstration of the wave front appearing planar at an area far from the transmission location.

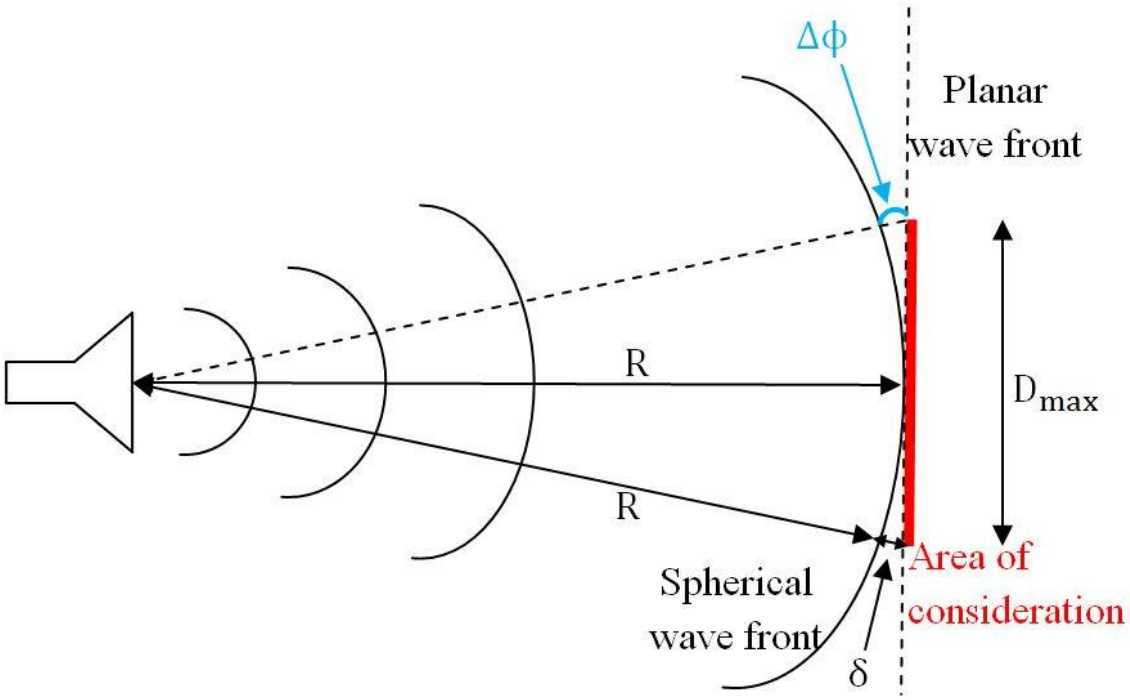


Figure B.1 Illustration of transmitting wave front as distance increases

Typically, a general rule of thumb for far field conditions is followed which states that far field conditions are met if

$$R \geq \frac{2D_{\max,t}^2}{\lambda} \tag{B.1}$$

where $R$ is the distance from the source to the area of consideration, $D_{\max,t}$ is the maximum dimension of the source (or transmitting) antenna, and $\lambda$ is the wavelength of the transmitted waveform. This rule of thumb follows the plane wave assumption that the maximum phase difference ($\Delta\phi$) between the actual incident field and its far-zone approximation does not exceed $\frac{\pi}{8}$ rad ($\equiv 22.5°$) [98-99]. Similarly, it has been shown that if $D_{\max}$ is taken as the maximum dimension of the area of consideration (the area considered in the far-field), a distance of $R_{\min}$ from the source of a spherical wave

ensures that the maximum phase difference between a plane wave and the spherical wave at the area of consideration is $\Delta\phi_{\max} = 22.5°$ when

$$R_{\min} = \frac{2D_{\max}^2}{\lambda}. \tag{B.2}$$

As illustrated in Figure B.1, the largest phase difference between the spherical wave and the plane wave appears at the edges of the area of consideration and specifically at the edges of the largest dimension of that area. This corresponds to the difference in the wave paths $\delta$, and the phase difference must fulfill the requirement:

$$k\delta \leq \frac{\pi}{8}. \tag{B.3}$$

The difference in the wave paths $\delta$ is determined by solving the quadratic equation

$$(R+\delta)^2 = R^2 + \left(\frac{D_{\max}}{2}\right)^2 \tag{B.4}$$

given by the geometry of Figure B.1. Thus,

$$\delta = \sqrt{R^2 + \left(\frac{D_{\max}}{2}\right)^2} - R \tag{B.5}$$

and (B.5) is approximated by the use of the binomial expansion as

$$\delta = R\left[\sqrt{1+\left(\frac{D_{\max}}{2R}\right)^2} - 1\right] \approx R\left[1 + \frac{1}{2}\left(\frac{D_{\max}}{2R}\right)^2 - 1\right] = \frac{D_{\max}^2}{4R}. \tag{B.6}$$

The minimum distance from the source of the spherical wave is now determined from the requirement in (B.3),

$$k\frac{D_{\max}^2}{4R} = \frac{2\pi}{\lambda}\frac{D_{\max}^2}{4R} \leq \frac{\pi}{8} \tag{B.7}$$

which is equal to (B.2).

Below, Table B.2 details the criteria for which far field conditions are met using this general rule of thumb for the adobe wall considered in this work. The maximum dimension $D_{\max,t}$ shown in the top of the table considers the maximum dimension of the transmitting horn antenna used in this work; the maximum dimension $D_{\max,r}$ shown in the bottom half of the table considers the maximum dimension of the adobe wall used during testing in the anechoic chamber. Hence, the maximum distance for the line of sight configuration is met if the distance between the antennas is greater than 1.5538 m for the frequency range considered, and the maximum distance for the monostatic operation intending to full illuminate the adobe wall is met if the distance between the transmitting antenna and adobe wall is 4.9755 m. For both configurations, the far-field (plane wave) conditions are met with the distance between the source and area of consideration being 5.105 m which is greater than 4.9755 m.

Table B.1 Far-field conditions for adobe wall radar measurement tests

| $f$ (GHz) | $\lambda$ (m) | $D_{\max,t}$ (m) | $R_{\min}$ (m) |
|---|---|---|---|
| 1 | 0.2998 | 0.2413 | 0.3884 |
| 4 | 0.0749 | 0.2413 | 1.5538 |
| | | | |
| $f$ (GHz) | $\lambda$ (m) | $D_{\max,r}$(m) | $R_{\min}$ (m) |
| 1 | 0.2998 | 0.4318 | 1.2439 |
| 4 | 0.0749 | 0.4318 | 4.9755 |

## B.2 Numerical Calculations of Pyramidal Horn Antenna

To confirm the general rule of thumb calculations, the radiation pattern for a pyramidal horn antenna with identical dimensions of the horn antennas used during testing is calculated using [100]. The radiation pattern is calculated on a $1\ \mathrm{m}^2$ plane

located 5 m from the source at frequencies of 1 GHz and 4 GHz; the results are shown below in Figure B.2. The radiation pattern is plotted with regards to phase change from the origin. The area that exhibits $\Delta\phi \leq 22.5°$ is marked on the phase plots and would be the area that contains a planar wave front. Thus, the wave front on a plane located 5 m from a pyramidal horn antenna of identical dimensions as the antennas used in the anechoic chamber would exhibit plane wave characteristics for an ellipsoidal area with a maximum radius of approximately 0.27m and minimum radius of 0.24m at 4 GHz. Hence, a circle with diameter of 0.48 m would encompass the entire exposed area of the adobe wall ($D_{\max}$ =0.4318 m) and the calculations of the radiation pattern confirms the plane wave behavior experienced in the anechoic chamber.

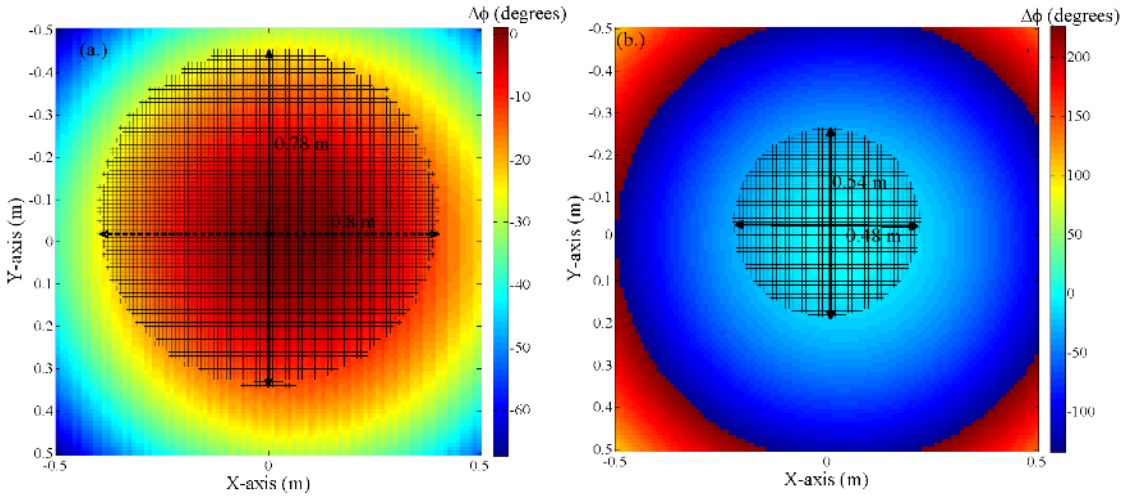


Figure B.2 Phase plots ($\Delta\phi$) of radiation pattern for a pyramidal horn antenna illustrating plane wave behavior of wave front

(a.) Source frequency of 1 GHz
(b.) Source frequency of 4 GHz